MODELING AND DYNAMICS ANALYSIS OF EMPTS

ZHANG JIDONG

2014

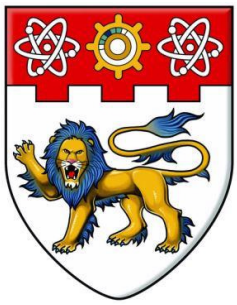

NANYANG TECHNOLOGICAL UNIVERSITY

MODELING AND DYNAMICS ANALYSIS OF ELECTRO-MECHANICAL POWER-TRAINS

ZHANG JIDONG

SCHOOL OF MECHANICAL AND AEROSPACE ENGINEERING

2014

MODELING AND DYNAMICS ANALYSIS OF ELECTRO-MECHANICAL POWER-TRAINS

ZHANG JIDONG

School of Mechanical and Aerospace Engineering

A thesis submitted to the Nanyang Technological University
in partial fulfillment of the requirement for the degree of
Doctor of Philosophy

2014

ABSTRACT

In the past few decades, the electro-mechanical power-trains (EMPTs) are being used to replace the conventional power-trains in a few transportations, such as “More Electric Aircraft” and “Hybrid Electric Vehicle”, to improve the energy efficiency and reduce greenhouse emissions. In the EMPTs, the electrical components such as electric machines, power electronics, controllers, and batteries are introduced. To accommodate these new components, the new power-train configurations are also involved.

Due to the new components and new configurations, the application of the EMPTs gets a few challenges, including: (1) the nonlinear dynamics in the power-trains have not been sufficiently investigated, resulting in a limitation of the design optimization formulations that can reduce the vibration and noise levels in the power-trains; (2) the electro-mechanical interactions in an EMPT are not fully understood, especially the reflection of the vibration signature onto the stator current of electric machines. Therefore, the stator current has so far not been effectively utilized to analyze the dynamics and monitor the health of the EMPTs; and (3) modeling of the EMPTs is challenging and time consuming due to a large variation in the modeling strategies with respect to an EMPT’s configuration and the intended research application. In other words, there is a lack of a modeling strategy that could be applicable to various types of the EMPTs and be implemented with relative ease.

To deal with the before mentioned challenges of the EMPTs, this doctoral research presents a study of the nonlinear dynamics involving gear rattle and electro-mechanical interactions in the power-trains, whose dynamic models were built based on a systematic co-simulation strategy developed for the EMPTs in the study. The key contributions of this doctoral research are as follows,

1. A systematic co-simulation modeling strategy, which utilizes the extensive model libraries of block diagrams (such as MATLAB/SIMULINK), multi-body system (such as SIMPACK), bond graph (such as 20-SIM), and finite element analysis (such as ANSYS and ANSOFT), is proposed to model the EMPTs of various configurations for different research applications. Compared with the existing modeling methods, the proposed co-simulation strategy is applicable to various types of EMPTs and at the same time allows for accurate models to be described with relative ease.

2. The nonlinear dynamics of the power-train having a gearbox during the occurrence of gear rattle was studied by developing a new analytical formulation. The formulation evaluated the level of vibrations and noise emitted during gear rattle by a gearbox with given parameters and therefore can serve as a guideline for gearbox design to reduce the rattle noise concern. This design guideline can help in reducing the time and capital in redesigning and remanufacturing a gearbox, which often result in selection of gearboxes for automotive transmissions due to the excessive vibration and gear rattle.

3. The electro-mechanical interactions were investigated by evaluating the transfer function from the gearbox vibration to the stator current of the electric machines. Using this investigation's result, a novel condition health monitoring method based on the resonance residual technique is proposed for the EMPTs through the measured stator current. Compared with the existing condition health monitoring methods, this new method is shown to be more sensitive to the incipient faults in the EMPTs.

Keywords: Electro-mechanical power-train; Co-simulation; Nonlinear dynamics analysis; Electro-mechanical interaction; Gear rattle; Condition health monitoring; Resonance residual method

ACKNOWLEDGEMENTS

Foremost I would like to express my warmest and sincerest thanks to my supervisor, Prof. Jaspreet Singh Dhupia, for his kind and patient guidance, keen insights, encouragements and friendship. He was always around whenever I needed him, and helped me focus in the right direction. His motivation and persistence helped me professionally.

I would like to express my gratitude to Nanyang Technological University for the opportunity to study here with a research scholarship.

Special gratitude goes to Rolls-Royce Singapore Pte. Ltd. for their provided research funding, and to Dr. Chandana J. Gajanayake and Mr. Nadarajan Sivakumar from Advanced Technology Center, Rolls-Royce Singapore Pte. Ltd. for their timely help and advice during my research.

I am also grateful to all the technicians in the Mechatronics Laboratory, and all the PhD students and staffs in our research group for their support over the past four year.

Most of all, I owe the greatest debt of gratitude to my family. I would like to thank my parents for a lifetime of support, encourage, and education. Lastly, I would like to thank my wife He Li whose love and support has helped to make everything I have accomplished possible

Table of Contents

List of Figures

List of Tables

List of Symbols

J inertia of the gear/carrier/rotor

θ angular displacement of the gear/carrier/rotor

r_b base radius of the gear/carrier

c gear damping coefficient

k gear meshing stiffness

N_a number of teeth on the annulus gear

ϕ_{ap1} relative phase for a gear pair consisting of the annulus gear and planet 1

Δk stiffness reduction due to the annulus gear tooth fault

v_q and v_d terminal voltages in q and d axes

i_q and i_d line currents in q and d axes

λ_q and λ_d magnetic flux linkages

ω_r electrical rotor speed

r_s resistance of stator winding

T_{em} electromagnetic torque developed by the PMSM

T_L load torque

p number of the poles

ω_m mechanical rotor speed

ω_r electrical rotor speed

D_ω viscous damping coefficient

T_{ch} churning torque function is given as

ρ_{lub} density of the lubricant oil

S_m immersion area of the gear in the lubricant

T_m dimensionless drag torque

h immersed depth of the gear in the lubricant

d_c pitch diameter

V_0 volume of the lubricant oil

f_N contact force acting on the gear teeth surface

ξ dynamic transmission error (DTE)

v_0 initial tangential speed of the pinion gear

b_{ls} half of backlash

Subscript:

pi represents the planet where *i*=1 to 4

s, *a*, and *c* represents the sun gear, annulus gear, and carrier

Chapter 1 Introduction

1.1 Motivation

The electro-mechanical power-trains (EMPTs), also referred to as hybrid power-trains, are now utilized to replace the conventional power-trains in many transportation applications such as more electric aircrafts, hybrid electric vehicles and hybrid electric ships [1-3], as shown in Figure 1.1 and Figure 1.2.

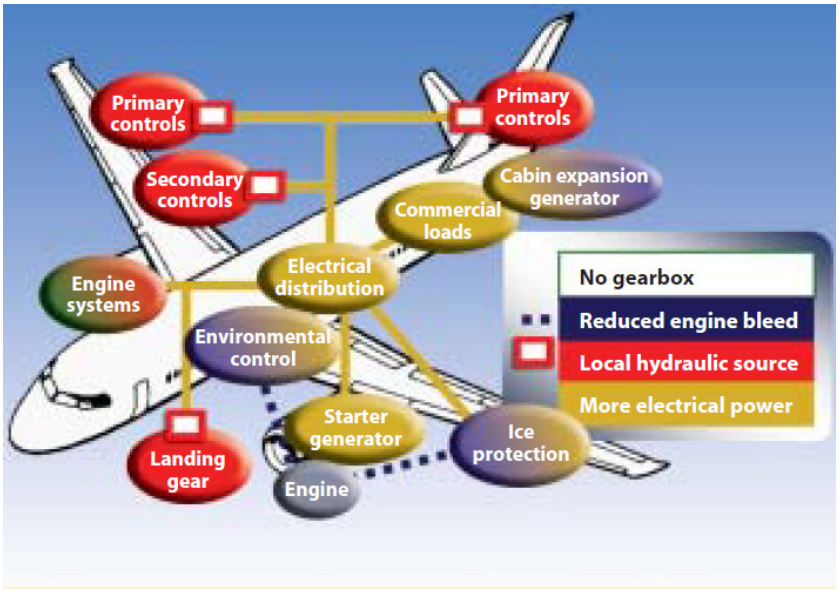

Figure 1.1 More electric aircraft [1]

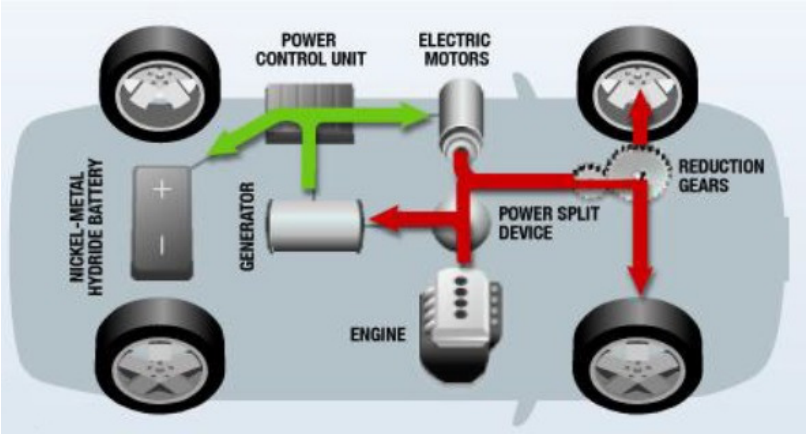

Figure 1.2 Hybrid electric vehicle (Toyota, Prius II) [2]

In the conventional power-trains, there are purely mechanical components. However, the EMPTs include additional electrical components such as electric machines, power electronics, controllers, and batteries [1, 4]. These electrical components can decouple the power generation stage from the power consuming stage in the power-trains, enabling the engine to always run at an optimized speed with high energy efficiency [5-7]. As a result, high fuel efficiency can be achieved in EMPTs during the whole operating period, reducing the air pollutant emissions.

The new components and new configurations in the power-trains will change the original dynamics and performance, raising a few concerns: (1) comfort should be delivered to the users, for example the vibration and noise level should be reduced as much as possible; (2) safety of the power-train should be guaranteed and always monitored properly; and (3) the power-train should be modeled properly to do dynamics investigation.

1.2 Problem Statement

To deal with the concerns on the application of the EMPTs, there still face a few challenges, i.e., (1) modeling of the EMPTs is time consuming and requires significant effort due to the variation in the modeling strategy with respect to the EMPTs' configuration and the intended investigation applications. There is a lack of model development methods which allows for overall electro-mechanical modeling capability and offer a high modeling efficiency in terms of required effort and accuracy; (2) the nonlinear dynamics in the power-trains have not been sufficiently investigated, resulting in a lack of the design

optimization knowledge, for example, sizing of gearboxes that may reduce the vibration and noise in the power-trains; and (3) the electro-mechanical interactions have not been fully investigated, especially the reflection of the torsional vibration signatures onto the stator current of electric machines. As a result, the stator current has not been effectively utilized to analyze the dynamics and carry out health monitoring of the EMPTs.

1.3 Research Objectives

The proposed doctoral research described in this document focuses on investigating the nonlinear dynamics of the EMPTs and the electro-mechanical interactions inside EMPTs, which can be used to optimize the system performance as well as to monitor their health conditions. A systematic co-simulation strategy will be proposed as well to help people to develop an EMPT model quickly with easy effort. To achieve these goals, the following specific tasks have been met:

1. Development of a systematic co-simulation strategy for the EMPTs, which allows for modeling overall EMPTs with high accuracy that can be applied to different types of configuration

To ease the efforts of modeling the EMPTs with various configurations and for different research purposes, a systematic co-simulation strategy is presented where a graphical user interface to develop block diagram models (such as MATLAB/ SIMULINK) is used as the platform along with other modeling techniques integrated to build highly accurate models for the EMPTs. The

integrated modeling techniques include multi-body system (such as SIMPACK), bond graph (such as 20-SIM), and finite element analysis (such as ANSOFT and ANSYS). This modeling strategy has high efficiency in terms of required effort and achieved accuracy that is applicable to any EMPTs.

2. Exploration of the nonlinear dynamics of the power-trains to optimize their dynamic performance

The nonlinear dynamics inside the power-trains can cause a few concerns, for example, excessive vibration and noise. A typical nonlinear phenomenon for the gearbox-based power-trains is the gear rattle occurrence. Therefore, the nonlinear dynamics during the gear rattle is explored. To reduce the gear rattle excited vibration and noise, the important gear parameters' effect on the gear rattle noise level is analytically evaluated, which can provide a guideline for the gearbox design optimization. This evaluation method has been verified by the simulation result from a dynamic model built in SIMPACK and by the previous published experimental results.

3. Investigation of the electro-mechanical interactions, based on which to propose a novel condition health monitoring technique for the EMPTs

The electro-mechanical interactions in the EMPTs enable to reveal the mechanical dynamics via electrical signature, and vice versa. An important application of this feature is to monitor the health condition of the power-trains based on motor current signature analysis (MCSA). Therefore, a transfer function between the vibration signature and the stator current of the electric

machine is built to investigate the interaction problem. With the analyzed result, a novel condition health monitoring (CHM) method is developed for the gearbox based on the resonance residual technique through MCSA. Compared with the conventional CHM methods, the proposed method is more sensitive to the incipient gearbox faults.

4. Design of an EMPT experimental testbed and verify the proposed novel CHM technique

To verify the developed model for the EMPTs as well as the proposed CHM method based on the resonance residual technique, a reconfigurable testbed has been designed and built at Mechatronics Laboratory in Nanyang Technological University. Four different power-train configurations can be achieved in this testbed. Several types of sensors are integrated into the testbed to acquire enough dynamics of the EMPTs, including current, voltage, speed, vibration, and torque. Finally, the developed model and the proposed CHM method are verified based on the experimental results under various operating conditions.

1.4 Key Contributions

Three key contributions have been made in this project, which are as follows:

1. A systematic co-simulation strategy, which utilizes the extensive model libraries available for block diagram development in MATLAB/SIMULINK, multi-body dynamics SIMPACK, bond graph development 20-SIM, and finite element analysis ANSYS and ANSOFT has been proposed to model the EMPTs of various configurations for different research applications. Compared with the

existing modeling methods, the proposed co-simulation strategy is applicable to different EMPTs configurations and at the same time provides high modeling accuracy.

2. The nonlinear dynamics of a gear-based power-train during the gear rattle occurrence was investigated by developing a new analytical formulation. This analytical formulation is based on simplifying the gearbox model to a single DOF model, solving its motion equations, and deriving the RMS of the unloaded gear acceleration, which is proportional to the gear rattle noise level. With this technique, the effect of the important gear parameters on the gear rattle vibration and noise level can be evaluated and a design guideline is provided to reduce the rattle noise in a gearbox. Compared with the conventional evaluation methods, the new method needs less time and less capital cost will be spent in manufacturing and installing the gearbox as well. A journal manuscript based on this work will soon be submitted to International Journal of Automotive Technology. A conference paper focusing on effect of different frictional factors on the gear rattle has been published in ISCIE/ASME 2014 International Symposium on Flexible Automation (ISFA 2014).

3. The electro-mechanical interactions were investigated through analytical evaluation of transfer function between the gearbox torsional vibration and the stator current of the electric machines. With this investigation, a novel condition health monitoring method based on the resonance residual technique is proposed for the EMPTs through the measured stator current. Compared with the existing condition health monitoring methods, this new method is more

sensitive to incipient faults in an EMPT. A preliminary investigation of electro-mechanical interactions through simulations were reported in 2012 ASME Dynamic Systems and Control Conference (DSCC 2012). The analytical basis of resonance residual technique for stator current analysis was presented in the 2014 IEEE/ASME International Conference on Advanced Intelligent Mechatronics (AIM 2014). Based on the simulation and experimental investigation, the novel resonance residual technique was developed and accepted for publication in IEEE Transactions on Industrial Electronics.

1.5 Organization of the Report

In this chapter, the motivation, problem statement, research objectives and key original contribution of the proposed research to develop models for the EMPTs, to explore their nonlinear dynamics, as well as to investigate the electro-mechanical interaction are described.

Chapter two provides the literature review in the area of the modeling, dynamics analysis, and CHM of the power-trains. The characteristics of the mechanical and electrical components as well as the overall configurations of the power transmissions are explored. Then, three typical modeling strategies for EMPTs are reviewed and compared. Finally, the typical faults of the EMPTs as well as the corresponding fault detection approaches are reviewed.

Chapter three proposes a systematic co-simulation strategy to model the EMPTs with various configurations and for varied investigation applications. A general description of this modeling strategy is provided to give the readers an overall

broad scope of investigation. Several different co-simulation case studies are presented to illustrate the implementation of this strategy clearly.

Chapter four develops an analytical evaluation method for the gear tooth rattle impact to investigate the contribution of the gear parameters on the impact. First, a dynamic model is developed for a typical transmission to describe the gear rattle dynamics. Then based on the built model, an analytical solution to obtain RMS of gear acceleration during the rattle impact is derived. Since, this RMS acceleration value is proportional to the rattling noise, the proposed analytical evaluation method is capable of investigating the gear parameters' effect on the rattle noise level, including backlash, meshing stiffness, inertia and meshing damping factor of the gearbox. To verify the proposed analytical evaluation method, a MBS dynamic model is developed for a typical transmission in SIMPACK. Comparing the analytical and dynamic simulation analysis, it can be found that the proposed analytical method can effectively predict the influence of gear parameters on the rattle noise. Moreover the predicted result is also in agreement with previously conducted experimental results from other researchers. Thus, the proposed evaluation method provides a simple guideline that can be used to optimize the gearbox parameters to reduce the gear rattle noise level. A journal manuscript based on this work is currently under review for publication in International Journal of Automotive Technology. A conference paper focusing on effect of different frictional factors on the gear rattle has been published in ISCIE/ASME 2014 International Symposium on Flexible Automation (ISFA 2014).

Chapter five first introduces the configurations and the components of a configurable EMPT experimental testbed. A dynamic model for a typical EMPT is built to explore the dynamic response under both the healthy and faulty gearbox conditions. Then, the transfer functions between the PMSM stator current response and planetary gearbox vibration are investigated, based on which a CHM method relied on the resonance residual technique is developed. Finally, the proposed CHM method is shown to be more sensitive and effective compared to the existing conventional methods through both simulation and experiments. A preliminary investigation of electro-mechanical interactions through simulations were reported in 2012 ASME Dynamic Systems and Control Conference (DSCC 2012) DSCC. The analytical basis of resonance residual technique for stator current analysis was presented in the 2014 IEEE/ASME International Conference on Advanced Intelligent Mechatronics (AIM 2014). Based on the simulation and experimental investigation, the novel resonance residual technique was written as a journal paper which has been accepted for publication in IEEE Transactions on Industrial Electronics.

Finally, chapter six provides the concluding remarks and future work of the research.

Chapter 2 Literature Review

A typical power-train comprises of the power generation, power transmission, and power consumption. According to the configuration, power-trains can be divided into conventional or electro-mechanical power-trains (EMPTs). Compared to the conventional power-trains, the EMPTs can offer significant benefits in terms of higher energy efficiency and easier control performance. However, the dynamic features of the electrical components are different from the mechanical components making it challenging to build a reliable accurate dynamic response model for the analysis of EMPT. A high fidelity model for the EMPT can assist in nonlinear dynamics analysis and exploration of electro-mechanical interactions. Therefore, the overall configurations and the individual components of the power transmissions are reviewed in Section 2.1. Three typical modeling strategies for the EMPTs are reviewed in Section 2.2. Finally, the typical fault types in the EMPTs and the existing condition health monitoring (CHM) approaches are reviewed in Section 2.3.

2.1 Power Transmission Systems

In this section, the configurations of the conventional power-trains and the EMPTs are presented and compared. The features of the typical mechanical and electrical components in the power-trains are reviewed as well.

2.1.1 Conventional power-trains

The conventional power-trains have been around for a while and used in several applications, where the mechanical power from the prime mover is transmitted to the load through an assembly of mechanical components. The typical mechanical components include internal combustion engine (ICE), transmission shaft, gearbox and bearing.

2.1.1.1 Overall configuration

The conventional power-train in a typical vehicle is used as an example to illustrate its configuration, where it is made up of the ICE, clutch, transmission, propeller shaft, final drive and wheels [5] (Figure 2.1). The ICE provides mechanical power to drive the overall power-train. Speed reduction and torque increase are implemented inside the transmission through different types of gears and gear-sets. However, the conventional power-trains can provide a low energy efficiency due to the facts [6] such as: 1) The ICE has an optimal speed where the highest efficiency can be achieved. However, the practical vehicle driving condition is time-varying, 2) To meet certain driving conditions such as acceleration and climbing, an ICE with a much larger size has to be used in the vehicle, which can reduce the power-trains' efficiency and vehicle's dynamics, 3) Due to frictional losses, significant energy is wasted as heat when the vehicle is under braking.

2.1.1.2 Internal combustion engine

The ICE converts the chemical energy into mechanical energy. According to the ICE configuration, it can be divided into the reciprocating engine, rotary engine,

and continuous engine [8, 9]. The reciprocating engine consists of two-stroke engine, four-stroke engine, six-stroke engine, and so forth. The continuous combustion engine comprises of the gas turbine.

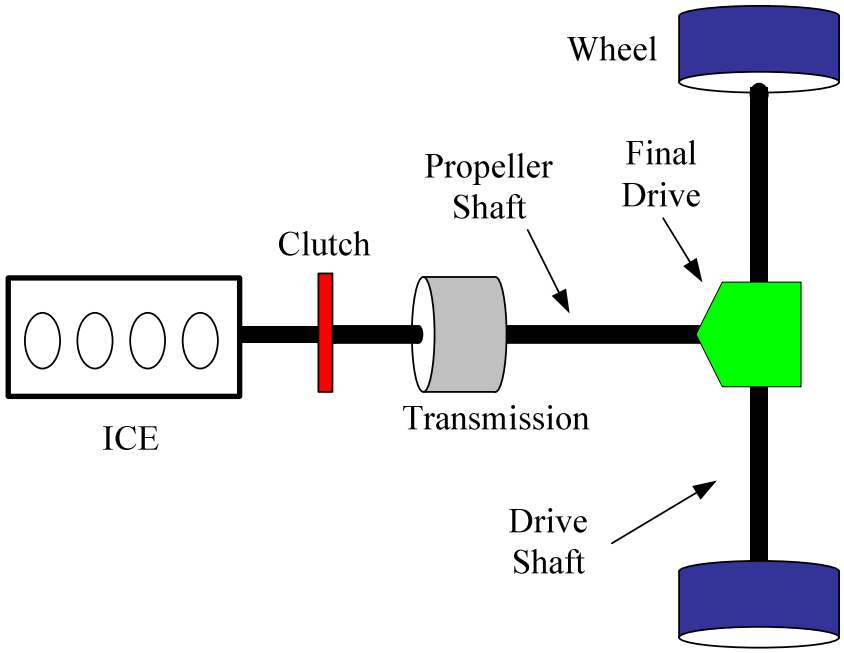

Figure 2.1 Schematic of the conventional power-train of a typical vehicle [5]

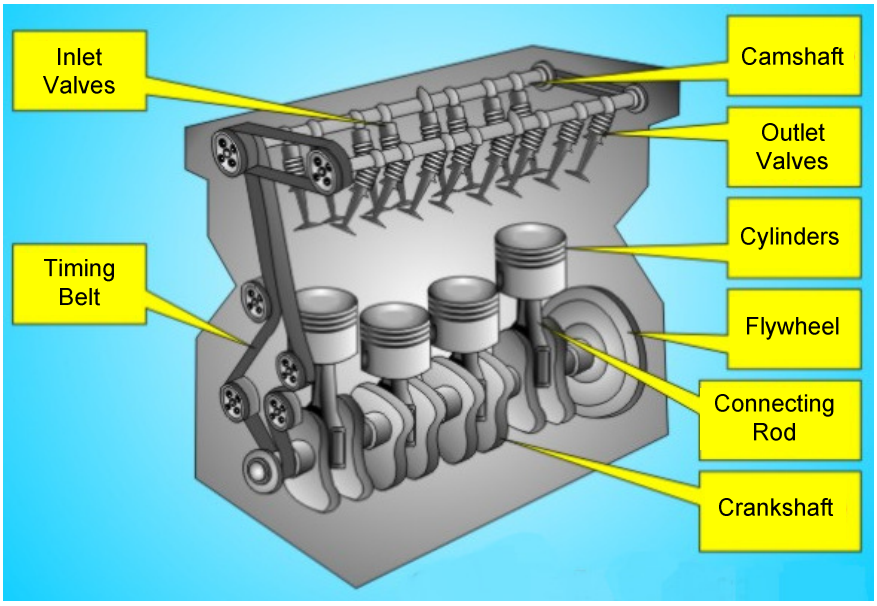

Figure 2.2 Diagram of a four-cylinder four-stroke engine

Reciprocating engines (e.g. Figure 2.2) have a high power-to-weight ratio with excellent fuel energy density and they are widely used in the vehicles and marine vessels. The gas turbines can provide a very large power as well and can be found in airplanes and huge marine vessels. Among reciprocating engines, the diesel engine has the highest thermal efficiency due to a high compression ratio. Some diesel engines can have a thermal efficiency over 50 percent.

Dynamics of an internal combustion engine

In a diesel engine, the generated torque can be controlled through calibration with fuel index to drive the shaft. A dynamic model for the diesel engine is introduced in [10], where its dynamic is divided into two parts: energy conversion and crankshaft dynamics. The dynamics of energy conversion relates the generated torque and the fuel index by the transfer function

$$T_{eng}(s) = \frac{k_Y(1+\Delta k_Y)e^{-\tau \cdot s}}{1+\tau_e \cdot s} Y(s) \tag{2.1}$$

where T_{eng} is the generated torque, τ is the manifold to power time delay, Y is the fuel index, k_Y is the gain constant, and τ_e is the time constant. Afterwards, the crankshaft dynamics is obtained from Newton's second law as

$$J_{cs}\frac{d\omega_{cs}}{dt} = T_{eng} - T_L - T_f \tag{2.2}$$

where J_{cs} is inertia of crankshaft, T_L is load torque, and T_f is friction torque. To achieve the expected output rotational speed, a speed control technique of the diesel engine is introduced in [11], where the fuel injection index is controlled by a speed controller using the crankshaft speed feedback and reference speed.

Torsional vibration of the ICE

Due to the firing sequence of the ICE, the pulsating components can be introduced into the driving torque, which can excite torsional vibration in the power-trains. This torsional vibration can be boosted by some potential factors such as 1) downsizing of the engine and flywheel to increase the dynamic response and fuel efficiency, 2) application of the direct-ignition, 3) removal of the clutch, and 4) unbalance of the engine mass. For example, in a *N*-cylinder four-stroke ICE, its speed fluctuates at three times of the mean speed ω_m [12], where *N* should be an even.

$$\omega_{cs}(t) = \omega_m + \Delta\omega\cos\left(\frac{N}{2}\cdot\omega_m t\right) \tag{2.3}$$

This torsional vibration may excite the gear rattle phenomenon inside the backlash that is a significant source of resulting noise and primary cause of passengers discomfort from power-train dynamics.

2.1.1.3 Transmission shaft

The transmission shafts or propeller shafts can transmit torque and rotational motion among different rotational components. However, large torsional and shear stress, for example, under resonance conditions can reduce their expected life span. The dynamics of a flexible shaft consist of lateral and torsional vibrations. The shaft bending increases with bearing-to-rotor stiffness ratio and rotor spin speed [13]. In a power-train with proper bearing support, low misalignment, low rotor eccentricity, and low rotational speed, the shaft dynamics is mainly dominated by the torsional vibrations. A flexible shaft can

be described by either a lumped parameter or a distributed parameter model. A brief description about the two modeling approaches is as follows:

Lumped model

If a shaft's inertia is much smaller than other rotational components such as the gearboxes and motor rotor, the shaft can be represented by an equivalent torsional spring damper system, where the torsional stiffness and damping coefficient can be obtained as [14, 15]

$$k = \pi G D^4 / 32L \tag{2.4}$$

$$c = 2\xi \sqrt{\frac{kJ_1 J_2}{J_1 + J_2}} \tag{2.5}$$

where G is the shear modulus of shaft, L is the length of shaft, D is the shaft diameter, J_1 and J_2 are the inertia of the two rotors connected to the shaft terminals, ξ is the shaft damping ratio shown to be within 0.005 and 0.075 by experiments [14, 15]. Dynamic response at low frequency can be provided by a single degree of freedom (DOF) model which is suitable for preliminary study of power-trains [16]. Better accuracy can be achieved for higher frequencies by introducing a multi-DOF lumped model, where the shaft can be divided into multiple elements along the axial direction with each element being described as a mass-spring-damper system [13]. Generally, five to ten elements are sufficient as only the first five to ten natural frequencies have dominant influence on the shaft dynamics.

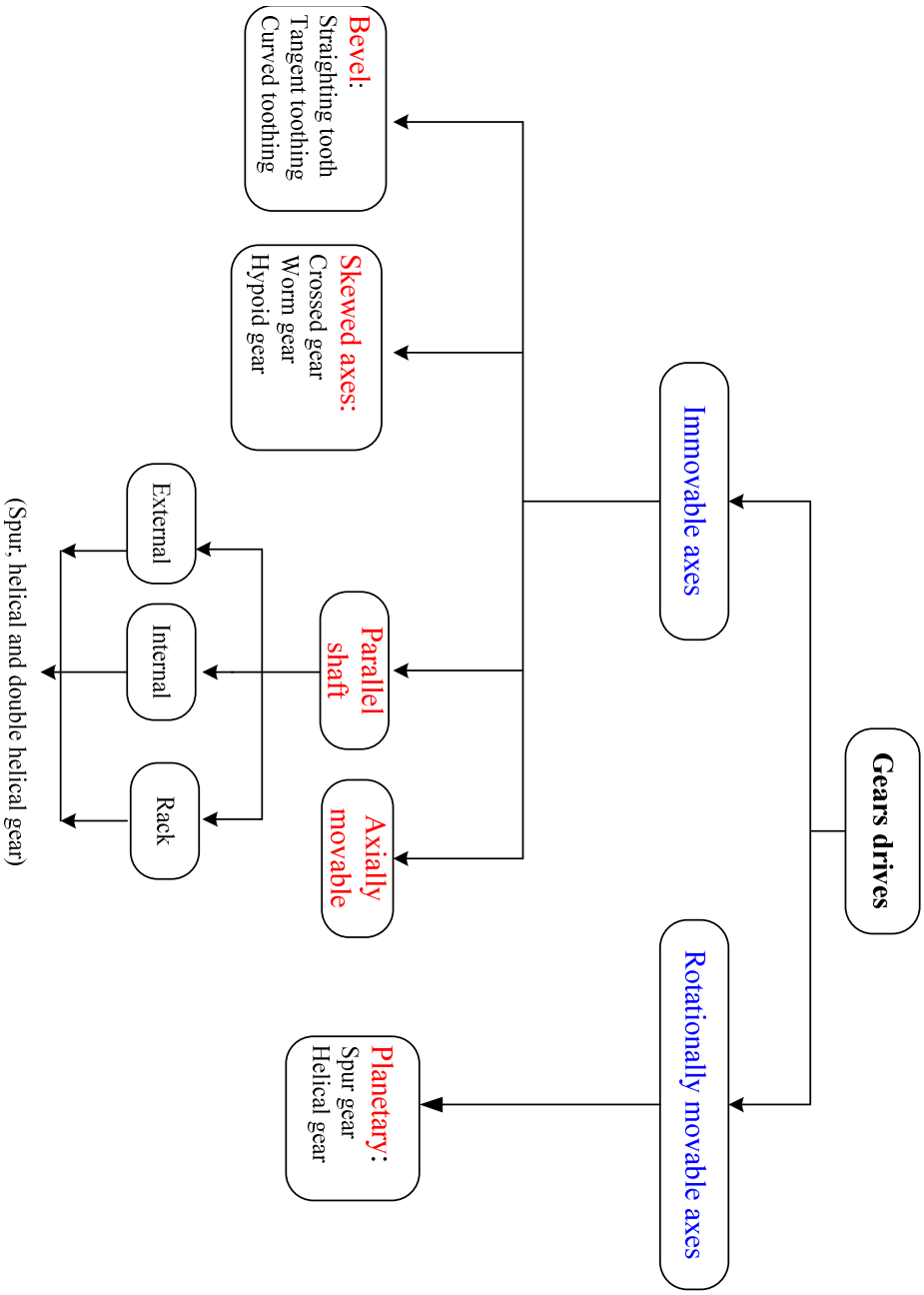

Figure 2.3 Classification of the gear drives [17]

Distributed model

Distributed modeling approaches can provide more accurate dynamic response as they treat the shaft as a continuous system with infinite DOFs. Although the theoretical knowledge to develop a continuous model for the shaft is available in the textbooks (e.g. [18]), a significant effort is required to integrate such

models with other power-train components to obtain the mode shapes and natural frequencies of the overall power-train configurations.

2.1.1.4 Gear drive

A gearbox provides speed, torque and direction conversions from a rotating component to another one, whose classification [17] is shown in Figure 2.3. In the practical applications, different types of gear can be combined together to build a gearbox with a particular configuration. To fit various research purposes, the static and dynamic models for the gearbox have been developed [5, 19, 20].

Static gearbox model

By ignoring the power loss and inertia of the gears and assuming the gears to be rigid, the output speed and torque of a spur gear pair can be described as

$$T_L = -(r_{bw}/r_{bp})T_p \tag{2.6}$$

$$\omega_w = (r_{bp}/r_{bw})\omega_p \tag{2.7}$$

where the input gear is referred to as the pinion, the output gear is referred to the wheel, and r_{bp} and r_{bw} are the base radii of the pinion and wheel. More accurate results can be achieved by taking the inertia and viscous damping into consideration [5].

Gearbox dynamic model

To better understand the gearbox transient dynamics, the dynamic models have been developed by including the gear meshing stiffness, damping coefficient, and gear profile imperfections in [19, 20]. The number of the gear tooth in

contact is a function of the rotational angle (Figure 2.4), which is usually designed to be 1 or 2 in a typical spur gear pair. If there are less teeth in contact, the gear meshing stiffness $k_g(t)$ equals to its minimum value k_{min}. Otherwise, it equals to its maximum value k_{max}. Thus, the gear meshing teeth $k_g(t)$, varying with the rotational angle, can be represented as a rectangular waveform as in Figure 2.5, where T_{GM} is the gear meshing period and ε is the gear contact ratio. Due to the manufacturing imperfections, such as gear eccentricities, non-uniform tooth spacing and tooth profile error, transmission error $e(t)$ exists even in a healthy gearbox. Therefore, it was taken into consideration in the model developed by [19]. If the variation of the gear meshing stiffness is not a concern, it can be assumed to be an equivalent constant [21]. The vibration signal measured on the gearbox housing requires the investigation of the dynamic response including the translational DOFs, wherein the flexibility of the supporting bearing should be taken in consideration as well [22-24].

Backlash and gear rattle

The backlash is the amount of clearance between the mated gear teeth, which is necessary to prevent jamming of the teeth due to manufacturing errors and thermal expansion [17]. Torsional vibration is inevitable in the power-trains due to a few potential factors, such as (1) pulsating torque from the ICE, (2) unbalanced mass of the power-train, and (3) occurrence of the mechanical resonance and variation of the operation speed. Excited by the torsional vibration, the gear teeth may vibrate inside the backlash producing the gear rattle noise. The rattle noise is an important cause of passenger discomfort in automotive applications.

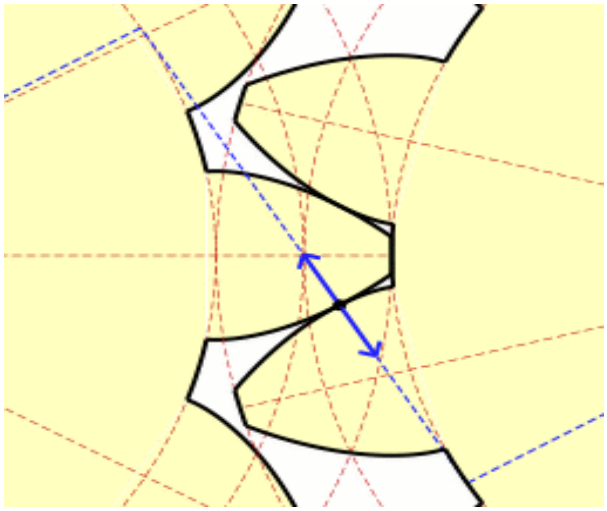

Figure 2.4 A pair of meshing gear

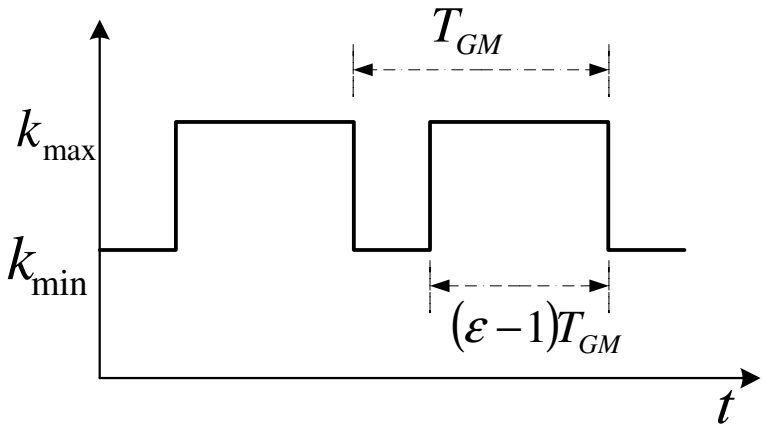

Figure 2.5 Time-varying gear meshing stiffness of a gear pair

2.1.1.5 Rolling element bearing

Rolling element bearings (REBs) can support a shaft or housing while permitting their free motion about a rotation axis [25]. The REBs are usually composed of four components: outer race, inner race, cage, and rolling elements (Figure 2.6), where the rolling elements could be balls, straight and tapered cylinders, as well as spherical rollers. There are many types of REBs available for various applications, such as deep-groove ball bearing, angular contact ball

bearing, cylindrical bearing, needle bearing, tapered bearings, and spherical bearing.

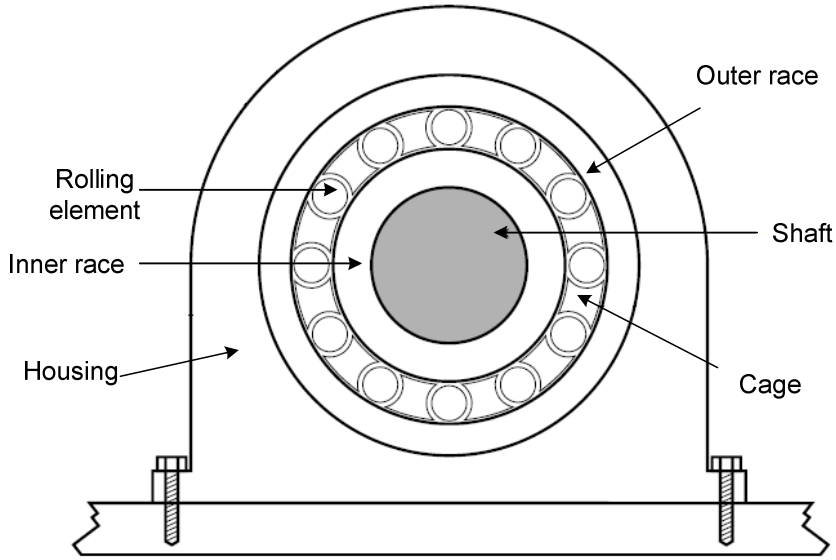

Figure 2.6 Schematic for a rolling element bearing

Dynamic model for bearings

A lumped model for the rolling ball bearing was introduced in [25], where it is modeled as a linear spring and damper connected to ground. A more accurate dynamic model for the rolling ball bearing was introduced in [26, 27]. In this model, the ball bearing is assumed as a solid multi-body system. Each component is connected with others via spring-damper elements (Figure 2.7). When the load applied to the bearing is moderate, the bearing vibrates linearly. The bearing motion can be described by a linear second order differential equation

$$\mathbf{M}\ddot{\mathbf{u}} + \mathbf{C}\dot{\mathbf{u}} + \mathbf{K}\mathbf{u} = \mathbf{F} \tag{2.8}$$

where **M**, **C**, and **K** are mass, damping and stiffness matrices respectively. The force vector **F** consists of forces in translational directions and momentum around the rotational axis for each element. Although this model is quite accurate, it is very difficult to acquire the model parameters in practice.

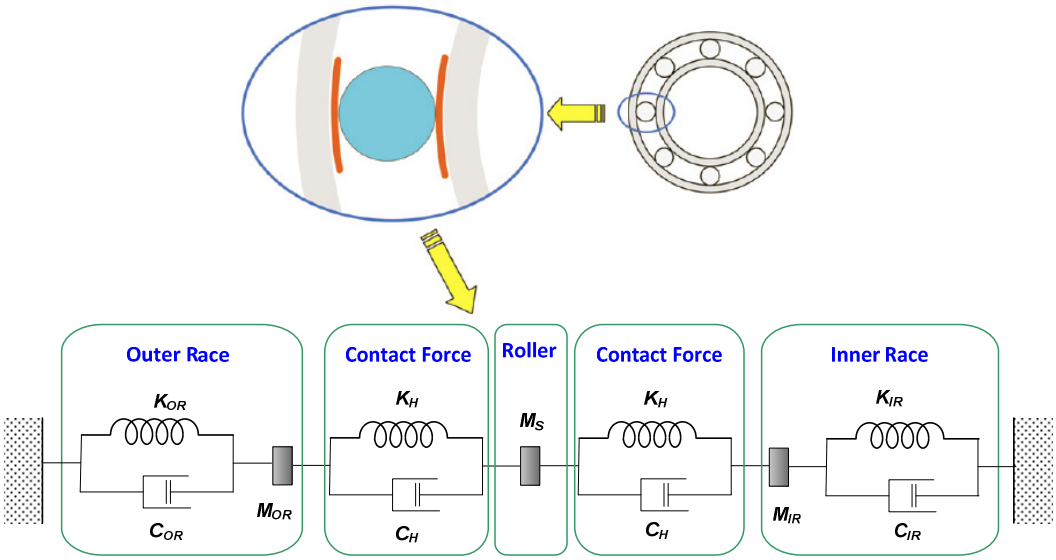

Figure 2.7 Three DOF bearing model [26]

2.1.2 Electro-mechanical power-trains

The electro-mechanical power-trains (EMPTs) provide a dramatic improvement in terms of higher energy efficiency and reliability. In an EMPT, in addition to the mechanical components, the electrical components can also be found such as electric machine, power electronics, controller and battery.

2.1.2.1 Overall configuration

The configurations of the EMPTs can be divided into the series, parallel, and series-parallel types [28, 29]. A few manufacturers have launched the products driven by the EMPTs, such as the vehicles and marine vessels. For example,

Toyota had launched its first hybrid electric vehicle (HEV) "Toyota Prius (XW10)" in 1997. Currently, its models Prius and Lexus RX400h are driven by the series-parallel hybrid power-trains. A typical series-parallel EMPT can be found in [30] (Figure 2.8), where there are two permanent magnet synchronous machines (PMSMs) MG1 and MG2. These two PMSMs are connected to the battery through the inverter. Both PMSMs can be controlled to work either as a motor or as a generator.

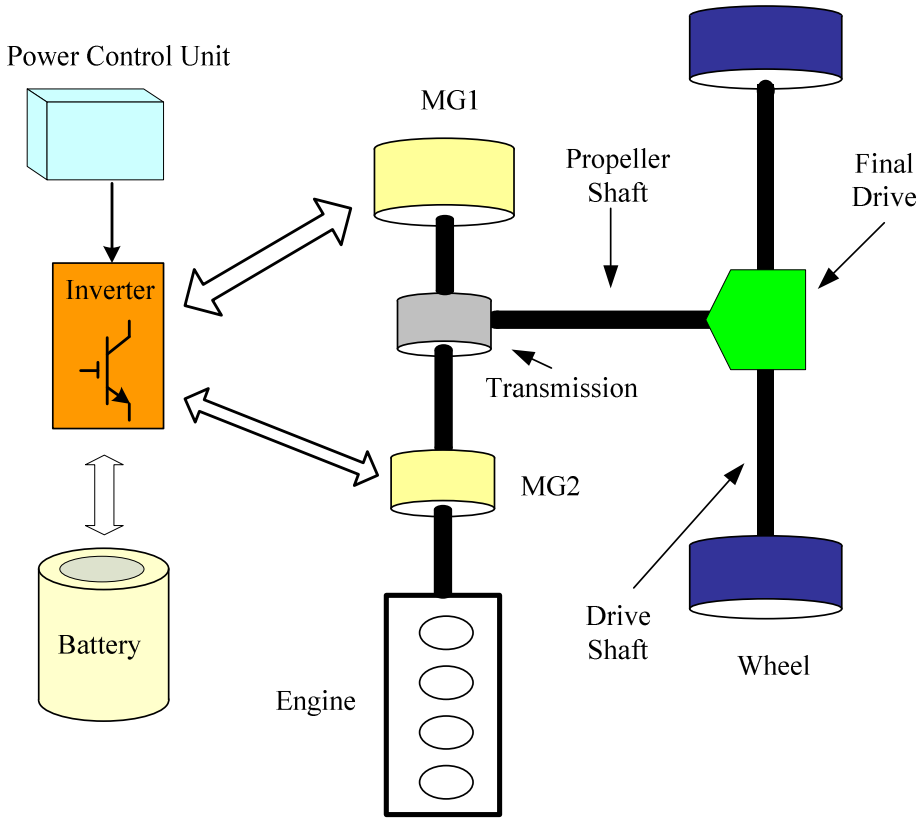

Figure 2.8 Schematic diagram of a series-parallel type of HEV [30]

At low driving speed, the vehicle can be driven by MG1 alone without switching on the ICE. At high speed, the ICE is switched on to drive the vehicle itself while maintaining high fuel efficiency. During the acceleration or climbing, MG1 can be used to boost the torque to help the ICE to drive the

HEV. Therefore, the power redundancy required from ICE in conventional power trains can be removed, which means that the size of the ICE only needs to meet the normal driving condition. As the speed of MG1 and MG2 is controlled and the ICE only runs at its optimal speed, the size of the transmission can be reduced as well. Regeneration is also implemented during braking, where the PMSMs operates as a generator to provide a braking torque and the battery is charged by the generated electricity [7]. This feature can significantly increase the energy efficiency especially under run-stop-run conditions encountered in city driving.

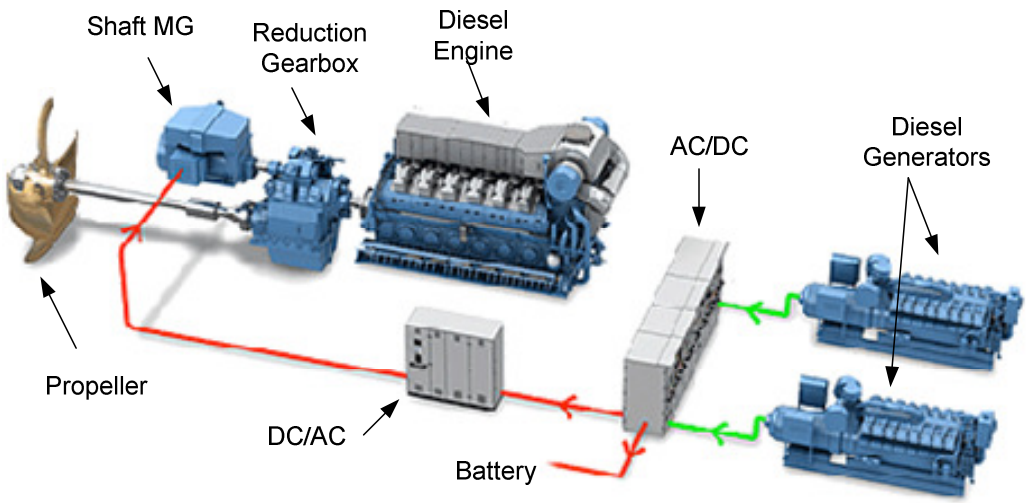

Figure 2.9 Hybrid shaft generator propulsion system (Rolls-Royce) [31]

Figure 2.9 presents a hybrid shaft generator propulsion system built by Rolls-Royce for the marine vessels [31, 32]. The shaft motor/generator (MG) can work as either a motor or generator. Power electronics and controllers regulate the power flow among the shaft MG, the two diesel generators, and the battery. There are five working modes for the EMPTs in the marine vessels, i.e., Boost, Diesel electric, Combinatory, Transit, and Shore connection. According to the

cruise speed and load of the marine vessels, the EMPTs can be automatically or manually controlled to operate under one mode which can provide the highest fuel efficiency. With this hybrid configuration, the fuel consumption of the marine vessels can be reduced by 5-30% [32]. Therefore, an EMPT can provide better fuel efficiency and reduced emission in this application area as well.

2.1.2.2 Electric machines

An electric machine is an electro-mechanical device used for conversion between the electrical and mechanical energy. In an EMPT, it can work as a generator by converting the mechanical energy to electricity using the power generation from the ICE or during regenerative braking. Also, EPMTs employ electric machines to work as a motor to drive the power-trains. According to their configuration, they can be divided into AC and DC types [33] as in Figure 2.10.

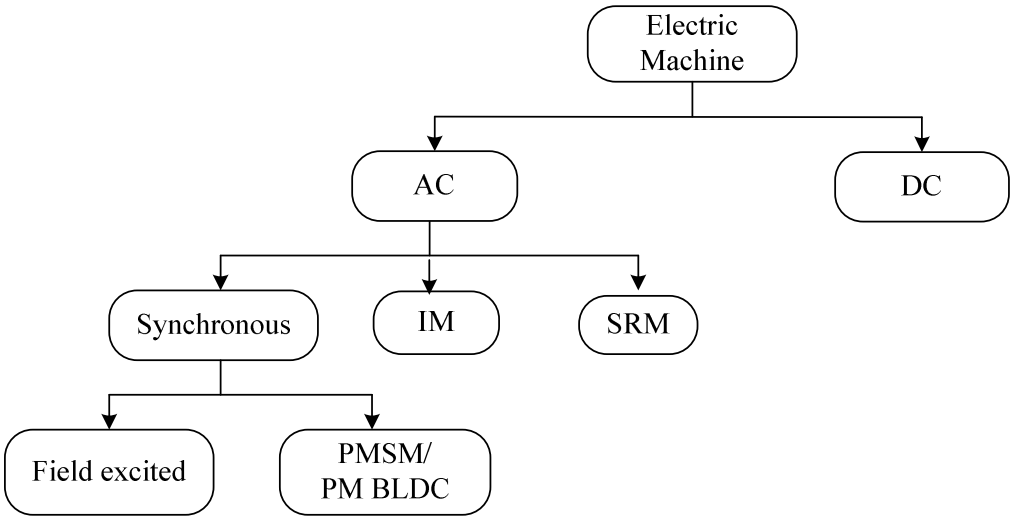

Figure 2.10 Classification of electric machines [33]

Due to the size and maintenance limitations, the DC machines are rarely used in EMPTs. Currently most of EMPTs are employing AC machines such as the induction machine (IM), switched reluctance machine (SRM), field-excited synchronous machine (FESM), and the permanent magnet (PM) machine. The IM, FESM and SRM are more robust and less expensive than the PM machines, however they do have some limitations [33]: (1) the IM and the FESM have lower efficiency as some of the energy is required to create the rotor magnetic field, (2) the SRM has a higher torque ripple and acoustic noise as it is driven only by the reluctance torque. The PM machines have a higher energy efficiency and power density as the rare-earth magnets on the rotor can produce a strong magnetic field without any need for electric power. According to the power source (sinusoidal type or trapezoidal type), the PM machines can be divided into PMSM and PM Brushless DC machine (PM BLDC) [34]. The selection of the electric machine types depends on the capital cost, space limitation, and performance requirement. The AC machine dynamics have been studied by using both the linear and nonlinear models.

Linear model

As a classical linear model for the AC machines, Park's model [33] has been proven to be effective enough in designing the control strategies for the AC machines. In this model, the variables (voltage, current, and magnetic flux linkage) associated with the stator winding are referred to a new reference frame. By this transformation, the time-varying inductances become constant in the new reference frame, reducing the complexity of the analysis.

The PMSMs can be described by Park's model [35] as Eqn. (2.9-2.12). Inside a PMSM, there are three-phase stator windings on the stator and PM poles on the rotor as in Figure 2.11.

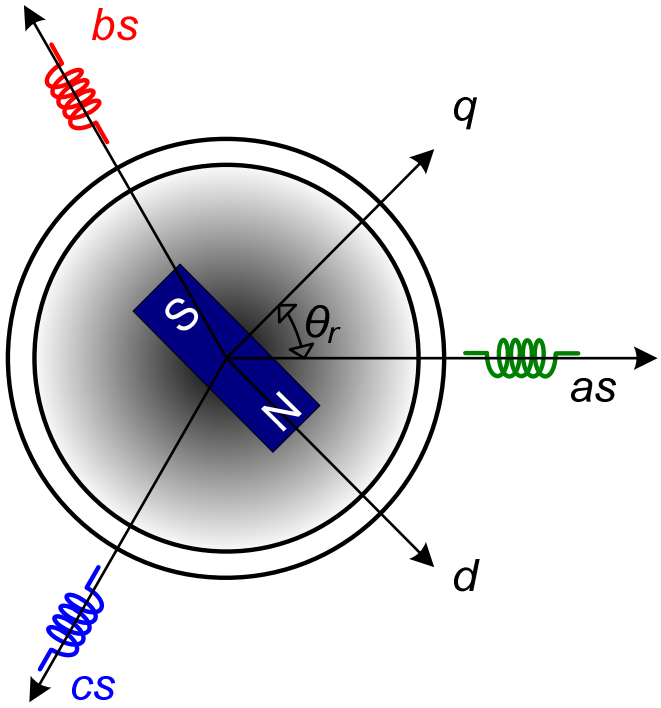

Figure 2.11 Magnetic axes of a PMSM

$$v_q = r_s i_q + \omega_r \lambda_d + d\lambda_q / dt \tag{2.9a}$$

$$v_d = r_s i_d - \omega_r \lambda_q + d\lambda_d / dt \tag{2.9b}$$

$$\lambda_q = L_q i_q \tag{2.9c}$$

$$\lambda_d = L_d i_d + \lambda'_f \tag{2.9d}$$

where v_q and v_d are the terminal voltages in q and d axes, i_q and i_d are the line currents in q and d axes, ω_r is the electrical rotor speed, r_s is the resistance of stator winding, λ_q and λ_d are the magnetic flux linkages. The electromagnetic torque developed by the PMSM is

$$T_e = \frac{3}{2}\frac{p}{2}\left[\lambda_f' i_q + \left(L_d - L_q\right) i_q i_d\right] \tag{2.10}$$

where p is the number of the poles. The motion equation of the PMSM is

$$J\frac{d\omega_m}{dt} = T_e - D_\omega \omega_m - T_L \tag{2.11}$$

where ω_m is the mechanical rotor speed, J is the rotor inertia, D_ω is the viscous damping coefficient, and T_L is the load torque. The relationship between ω_r and ω_m is

$$\omega_m = \frac{2}{p} \cdot \omega_r \tag{2.12}$$

To linearize the machine parameters, Park's model makes a few assumptions [33, 36-39], such as (1) no magnetic saturation and core losses, (2) the number of the stator winding coils is distributed sinusoidally around the stator, (3) the influence of the stator slot on the magnetic permeance is negligible, and (4) the ideally balanced three-phase winding. Therefore, Park's model cannot be used to analyze the higher order dynamics of the electric machines.

Nonlinear models

Design optimization of the electric machines requires consideration of factors such as the winding configuration, magnetic saturation, vibration, temperature, and torque ripple, which can introduce nonlinear dynamics into the models. The electro-mechanical interactions are affected by the higher order harmonics in the stator current as well, which requires developing a nonlinear analytical model such as those built through Finite Element Analysis (FEA). A general purpose FEA software ANSYS has been proposed to build nonlinear models of

the electric machines to optimize the performance in [40, 41]. There are several FEA modeling tools available which are specially designed for the nonlinear modeling of the electric machines, such as ANSOFT, Flux 2D/3D, and Opera-2D [42-45], where special modules of the electric machine components have been prepared to reduce the modeling effort.

2.1.2.3 Power electronics converter

The power electronics converter converts the power input at certain alternative voltage level and frequency to the other voltage level and frequency. A converter mainly relies on an electronic switch to manage the power conversion where the switches are controlled by the gating signal from the control circuit. According to the input and load type, the converter can be divided into four basic types [46]: AC to DC rectifier, AC to AC cycloconverter, DC to AC inverter, and DC to DC converter. A typical commercial variable frequency inverter that is connected to a power grid to drive an electric machine consists of a DC/AC converter, an AC/DC inverter, a low pass filter circuit, and a gating signal control unit as shown in Figure 2.12.

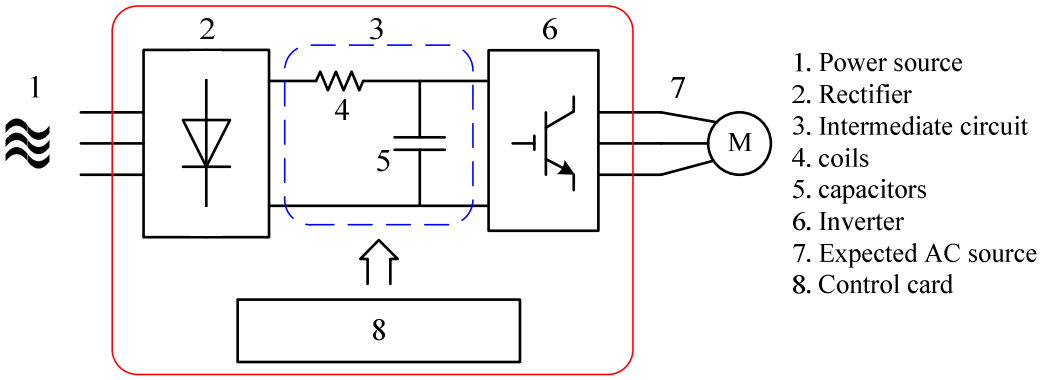

Figure 2.12 Diagram of a typical electrical drive [46]

2.1.2.4 Control strategy of electric machines

The control of a DC machine is simple and straightforward as there is no coupling between the armature current i_a and the field flux ϕ excited by either the field winding current or the permanent magnet in the electromagnetic torque T_e as

$$T_e = k\phi i_a \tag{2.13}$$

where k is a constant determined by the configuration of the DC machine. However, the electromagnetic torque of an AC machines is determined by the amplitude, phase, and frequency of the stator current [34, 47], which are coupled together. Therefore, the AC machine control is much more complex than that of the DC machine. The control methods of the AC machines can be mainly divided into scalar control and vector control.

Scalar control

The speed of AC machines is (roughly) proportional to the power supply frequency f, while the induced voltage V in the AC machines is proportional to the rotational speed. With scalar control, the voltage of the power supply is set to be proportional to its frequency such that V/f = constant [47]. Therefore, the speed of the synchronous machine can be controlled by the variation of the voltage and frequency. Scalar control is easy to implement and it provides good steady-state performance. However, its response time to speed/torque variation is much larger than the vector control.

Vector control

The vector control provides a better dynamic response by controlling not only the amplitude and frequency of the stator current but also the phase. As in the phasor diagram of the PMSM in Figure 2.13, the stator current phasor $\mathbf{i}_s$ can be decoupled into i_q and i_d on the rotor reference frame. A few control strategies have been proposed through controlling i_q and i_d separately [34], such as the constant torque-angle control, unity power-factor control, optimum-torque-per-ampere control, and flux-weakening control.

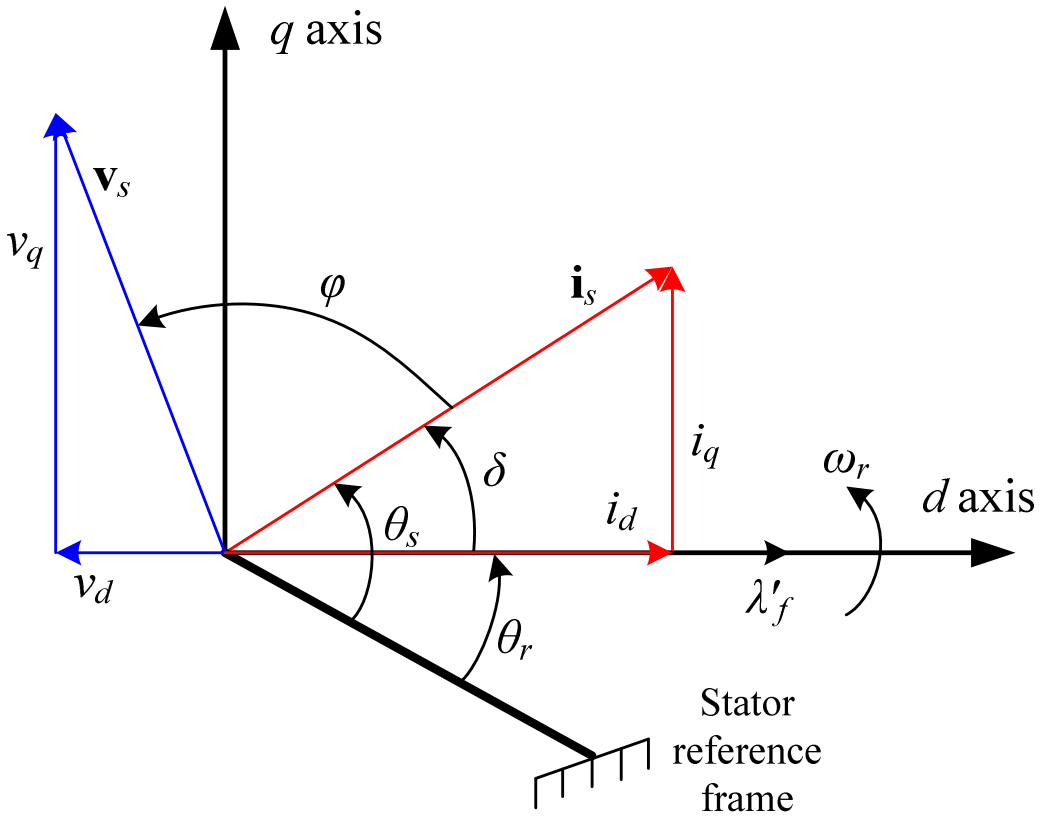

Figure 2.13 Phasor diagram of the PMSM

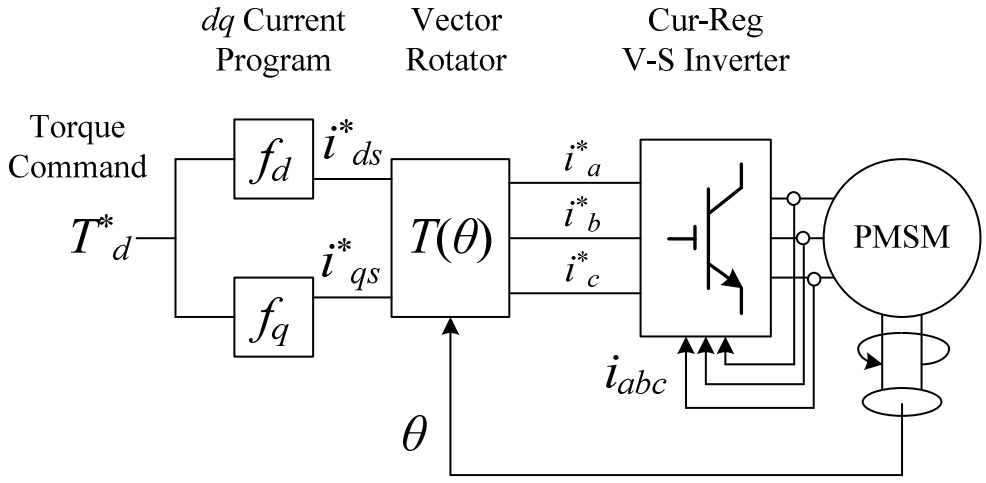

Figure 2.14 Block diagram of torque control scheme for PMSM using vector control [48]

In the constant torque-angle control, by setting i_d to be always zero ($\delta = \pi/2$) in Eqn. 2.10, the electromagnetic torque T_e will be directly proportional to i_q as

$$T_e = \frac{3}{2}\frac{p}{2}\lambda'_f i_q \tag{2.14}$$

Therefore, the desired torque can be achieved by controlling the stator current i_q alone. A block diagram of the torque control of the PMSM based on the vector control was presented in Figure 2.14 [48], where the stator current is measured by Hall Effect sensors and the rotational speed is measured by a resolver / encoder. The measured variables are used as the feedback signals to the PI controllers to drive the inverter to output the expected current. The detailed tuning methods of the PI controllers can be found in several literatures, e.g. [49].

2.1.2.5 Energy storage system

The most challenging part of the commercialization of the EMPTs is the portability of the energy storage devices that allow high power output, high

power density, and low cost [7]. The energy storage devices include rechargeable batteries, supercapacitors, flywheels, fuel cell, and so forth.

Rechargeable battery

Among the energy store systems, the rechargeable batteries play the most important role. The lead-acid type battery has been used for several decades with low cost, low power output and low power density. The Lithium-ion (Li-ion) provides higher power output and power density. However, its application is limited by the factors: (1) initial cost is much higher than the lead-acid, and (2) more safety attention is needed.

In an empirical model proposed in [50], the battery was modeled as an ideal voltage source E_0 connected in series with an internal resistance R_b as shown in Figure 2.15. This model gives a simple relationship between the output current and voltage. However, it does not consider the time varying internal resistance of the battery, allowing the drawn energy to be unlimited. Therefore, it is only suitable for the static evaluation of the capacity and energy density of the battery.

An electric circuit model for the battery that considers internal chemical phenomena such as SoC and the diffusion process was introduced in [7] (Figure 2.16), where both the diffusion process and effect of SoC are represented as a resistance-capacitor parallel circuit. Therefore, this model can provide more detailed information of the battery dynamics. However, the model parameters are not always available to the end users, challenging its practical application [7].

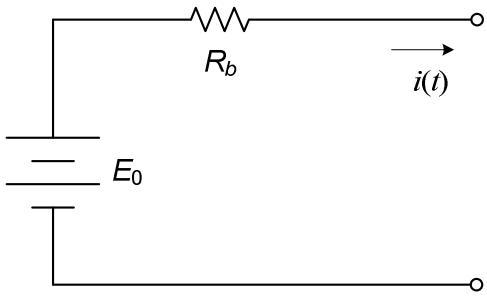

Figure 2.15 Empirical model of battery

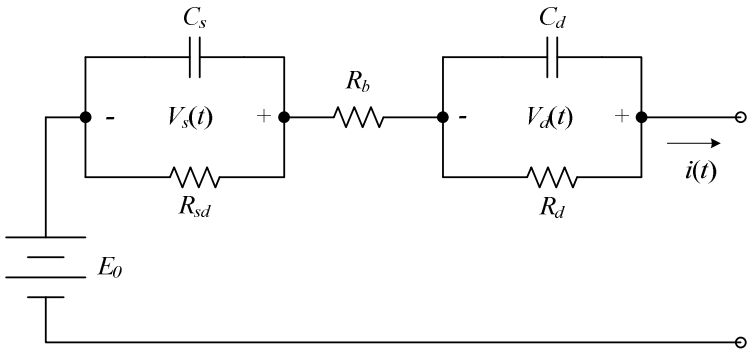

Figure 2.16 Electric equivalent circuit model of battery [7]

Supercapacitor

The power density of the supercapacitors is lower compared to the batteries, however they have a much higher energy efficiency, a higher power output capability, and a much longer life cycle than the batteries [30]. Therefore, a hybrid energy storage device consisting of the supercapacitors and batteries is recommended for the EMPTs to provide a better and more robust dynamic performance. A simple equivalent electric circuit model for the supercapacitor was proposed in [7] (Figure 2.17), where C is the capacitance in farads, R_p is the parallel resistance which accounts for the self-discharging losses, and ESR is the internal resistance during charging and discharging.

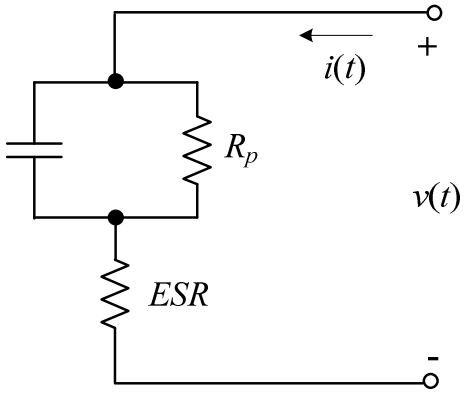

Figure 2.17 Electric equivalent circuit model of supercapacitor [7]

2.2 Dynamic Modeling of Electro-Mechanical Power-Trains

A reliable dynamic model for the EMPT can assist in the nonlinear dynamics analysis and the electro-mechanical interaction investigation. Therefore, significant efforts have been put in the development of EMPT models.

2.2.1 Existing models of electro-mechanical power-trains

Compared to the static models of the EMPTs, the dynamic models can provide transient information through modal analysis, vibration evaluation, dynamics analysis, and so forth [15, 19, 51].

To evaluate the dynamic performance of the hybrid electric vehicles, the dynamic models for the hybrid power-trains were built in [52-54], where each rotor was modeled as inertia and the stiffness was neglected as shown in Figure 2.18. In [53, 54], the Bond Graph method was utilized to model the power-trains. With this model, the vehicle's acceleration/braking response to different driving torque and load conditions can be obtained and optimized. In [55, 56], dynamic models were built for the wind turbine and vehicles, where the torsional stiffness of both the transmission shafts and the rotor inertia were

taken into consideration. In [55], a model library was built by the author to build the overall power-trains. With these models, the modal analysis can be implemented. Based on this information, the resonance frequency can be removed from the operating range.

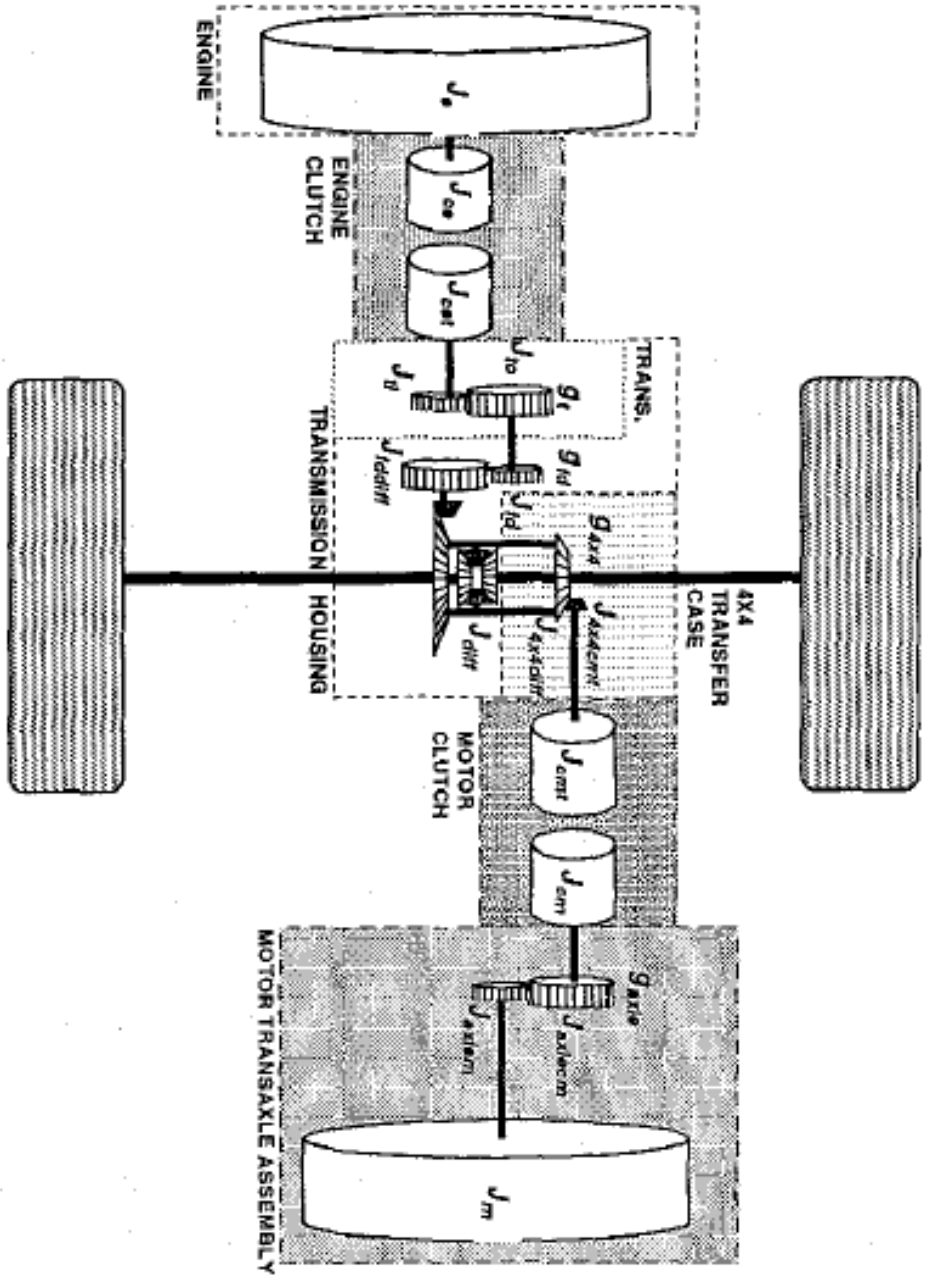

Figure 2.18 A parallel hybrid power-train [52]

The angle-varying gear meshing stiffness accompanied with the rotation of the gear-based EMPTs results in a lot of vibration and noise [22]. To reduce the vibration excited by gear meshing stiffness, the stiffness variation was taken into consideration in the dynamic models developed for the wind turbines [15, 57]. The gearbox models with four different levels of complexity had been built to compare their dynamic response considering the gear inertia, damping and stiffness, and shaft stiffness [58]. Not only the gear meshing stiffness but also the bearings supporting the gears can affect the dynamic transmission error of the power-trains. Therefore, to obtain a more accurate dynamic transmission error, the bearing stiffness was included in the models built for the power transmissions in [59, 60]. Furthermore, the bearing stiffness can affect the vibration transmission path in the vehicles, and thus it was included in a model built for the gear rotor bearing system in [24].

The gearbox backlash can cause excessive noise and vibration under rattling condition, to study the nonlinear dynamics of the gearbox-based power-trains, the backlash was incorporated in the models for the automotive transmissions in [61-63] as shown in Figure 2.19. This model can be used to study the nonlinear vibration and noise excited during the gear rattle occurrence, whose amplitude is determined by several important gearbox parameters, such as backlash, stiffness, damping, as well as inertia. However, the effect of these parameters on the rattle vibration and noise has not been effectively evaluated. The static transmission error, resulting from the gear profile error and installation error, was included in a power-train model to explore its effect on nonlinear dynamics [64]. To explore the dynamics of the power-trains containing the faulty gear

tooth and detect the failure, the effect of the faulty tooth was modeled as a reduction of the gear meshing stiffness function where the reduction occurs whenever other gears pass through the faulty teeth [65, 66].

From the reviewed models, it can be concluded that, (1) several models have been built for different configurations of EMPTs; (2) the focuses of these models vary according to needs of investigation as well; (3) for higher accuracy, the model requires more complex modeling approaches.

2.2.2 Model development methodologies

The modeling approaches of these reviewed models of the EMPTs in Section 2.2.1 can be divided into three types: model library [55], bond graph [53, 54, 58], and general mathematical description [65-67].

2.2.2.1 Model library method

With the model libraries consisting of the models for the basic EMPT components, models for an overall EMPT can be built by searching the suitable basic models from the model libraries and combining them together. The modeling tools, such as graphical programming (available in MATLAB\SIMULINK), multi-body system (SIMPACK), and finite element analysis (ANSOFT), provide several basic models required in the modeling of an EMPT where each modeling tool has its own benefits and limitations.

SIMULINK

Integrated with MATLAB, SIMULINK provides a graphical user interface to model the EMPTs [68]. On one hand, SIMSCAPE, which is incorporated into

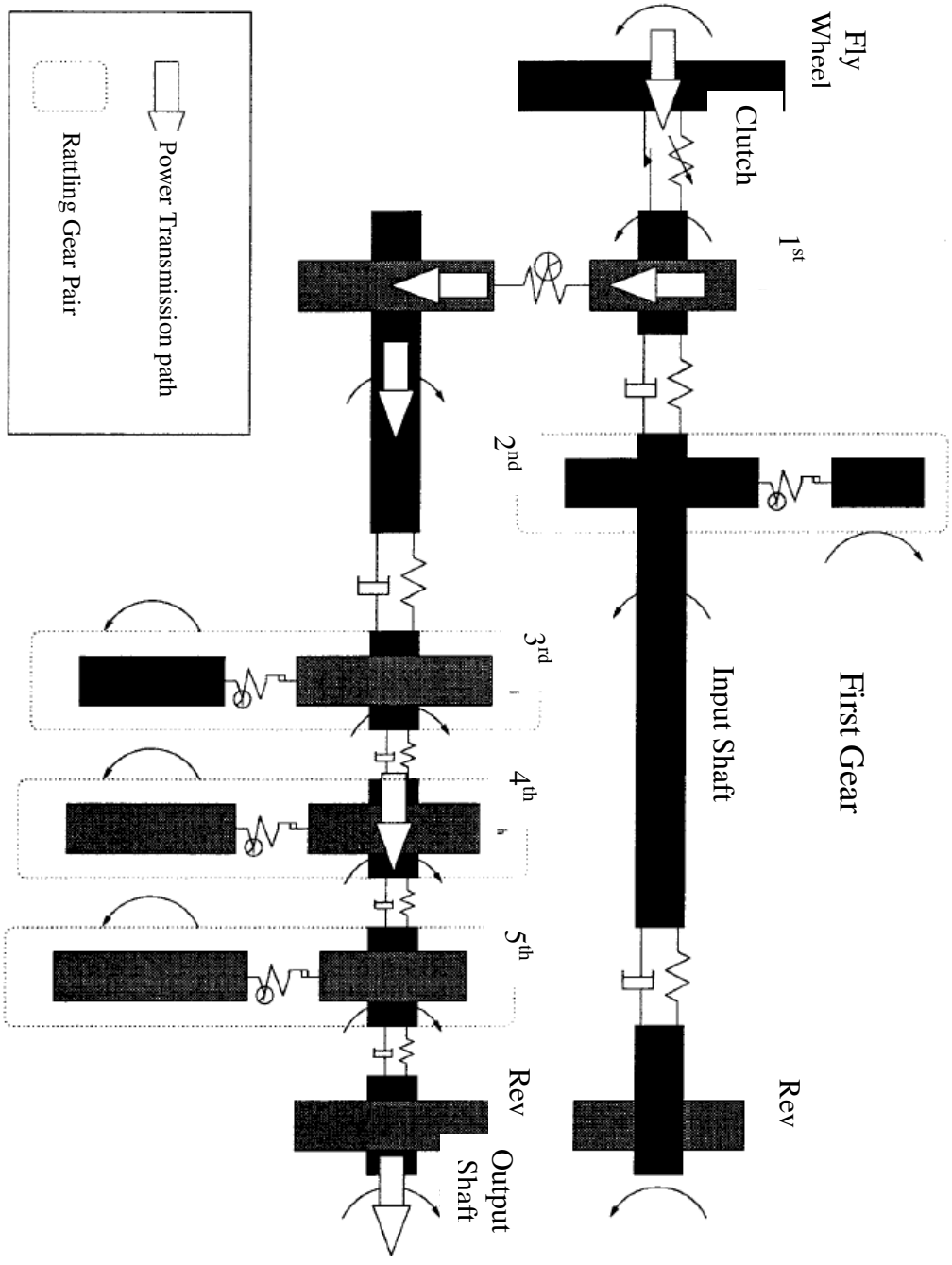

Figure 2.19 The power-train model for the first gear [62]

SIMULINK, includes a few models for the EMPT components, such as the electric machines, power electronics, mechanical shafts and gears. On the other hand, SIMULINK provides several basic mathematical operation blocks

(addition / subtraction, multiplication / division, integrator / derivation, and so forth) and the user-defined functions to help the users to build their own models. For example, a dynamic model of the vehicle power-train was built using SIMULINK mathematical blocks and its control strategy was implemented through these blocks [52]. Although the models in SIMSCAPE provide useful dynamic information, some nonlinearity is still missed or difficult to be incorporated, such as the nonlinearity of the electric machines and the gear meshing stiffness. Therefore to build reliable models for the EMPTs, the professional electromagnetic and mechanical modeling tools such as ANSOFT and SIMPACK are utilized.

SIMPACK

The multi-body system (MBS) software SIMPACK provides a model library for the mechanical components of the power-trains [69]. Compared to SIMULINK /SIMSCAPE, the models in SIMPACK include more detailed nonlinear dynamics. For instance, an existing force element representing the angle-varying gear meshing stiffness can be found in SIMPACK, while a similar element is not available in SIMULINK. Besides of the provided lumped models, the distributed models can be integrated into SIMPACK as well through the model reduction technique (FE-MBS coupling) where the finite element models of the flexible bodies created in ANSYS can be simplified and incorporated into SIMPACK.

ANSOFT

ANSOFT consists of several different modeling modules such as MAXWELL and SIMPLORER which can be used to study the electromagnetics problems [70]. For example, MAXWELL is capable of modeling the electric machines with finite element method, enabling to investigate their nonlinear dynamics. SIMPLORER on the other hand provides basic models of the electrical and electronics components which can be used to simulate the power electronic driving circuits of the electric machines at the physical level.

Co-simulation

To take advantage of the various model libraries at the same time, SIMULINK provides interfaces to integrate SIMPACK, and ANSOFT with SIMULINK. For example, a co-simulation is implemented between SIMULINK and SIMPACK to study the driving performance of a semi-active suspension vehicle, where a detailed multi-body model was established for the vehicle in SIMPACK while the corresponding hybrid control strategy was implemented in SIMULINK [71]. A wind turbine with doubly fed induction generator was modeled through a co-simulation between SIMPLORER and SIMULINK, where the generator was described with a finite element model in SIMPLORER while the drive circuit, controller implementation, and the power-train are modeled in SIMULINK [72], as shown in Figure 2.20. A synchronous servo drive under speed control mode, comprised of a PMSM and a sinusoidal type voltage source inverter, was investigated by a co-simulation as well where the PMSM and the inverter were modeled in SIMPLORERE while the control strategy was implemented in SIMULINK [73]. Compared with the models based on a single model library,

the co-simulation provides more flexibility and reliability in modeling the EMPTs.

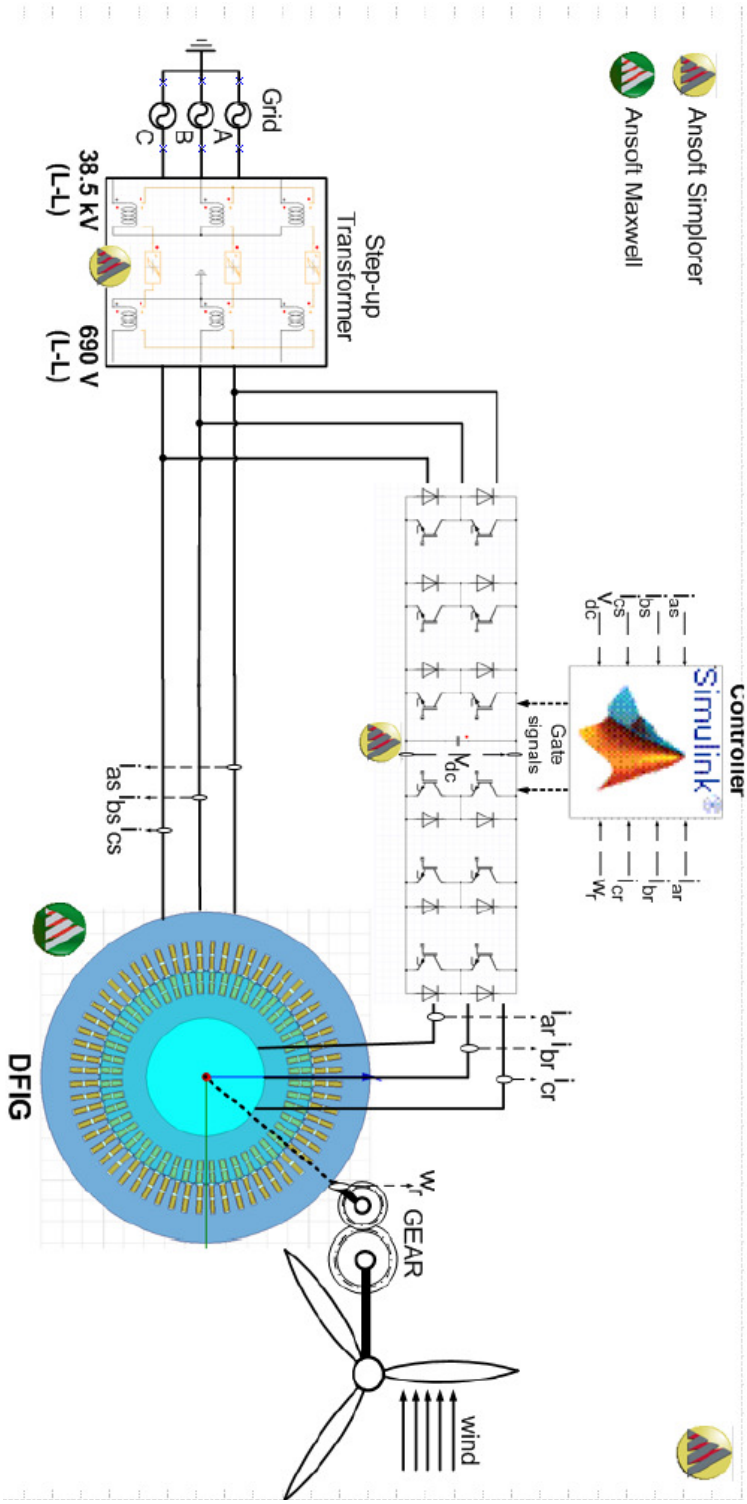

Figure 2.20 Schematic diagram of co-simulation in wind turbine [72]

2.2.2.2 Bond graphs

Bond graphs are domain-independent graphical tools to capture the dynamic behaviors of physical systems from different domains including the electrical, mechanical, hydraulic, thermal, fluid, and so forth. The concept of bond graphs was introduced by H.M.Paynter in 1959 and published in 1961 [74]. The idea was further developed by Karnopp and Rosenberg [75-77], which enabled the technique to be put into practice [78].

Modeling principles

In a bond graph, there are four groups of basic standard elements, i.e., three basic one port passive elements (R, C, I), two basic active elements (SE, SF), two basic two port elements (TF, GY) and two basic junctions (0, 1). In the elements or subsystems, places where they can be interconnected are called (energy) ports. According to the system topology, a model can be built by connecting the energy ports of the elements to the junction structures through the bonds, where the junction is the manifestations of the constraints. The energy exchange among different elements is achieved through the energy ports which involve two power factors i.e., Effort *e* and Flow *f*.

To model a system involving different physical domains, bond graphs propose the concept of the "analogies", which means that the components in different domains that are analogical to each other can be described by the same elements. For example, in the R-element, the Effort *e* and the Flow *f* variables at the single port are related by a static function $e = R \times f$ as in Figure 2.21. Usually, resistors dissipate energy. This must be true for simple resistors and mechanical

dampers. Similar R-element, C-element and I-element in different physical domains are shown in Table 2.1. Accordingly, Effort and Flow have different interpretations in different physical domains as shown in Table 2.2. The product of the Effort and Flow is the instantaneous power transmitted via the power port. For example, the energy transmitted to the R-element is $P = e \times f = R \times f^2$.

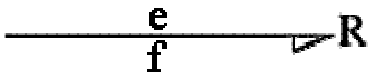

Figure 2.21 R-element representation

Table 2.1 R, C, and I variables in different physical domains

One port element	Translation	Rotation	Electrical
R	Damper	Rotational damper	Resistor
C	Spring	Torsional spring	Capacitor
I	Mass	Inertia	Inductor

Table 2.2 Effort and Flow variables in different physical domains

Bond Graph	Translation	Rotation	Electrical
Effort e	Force F N	Torque τ N.m	Voltage V V
Flow f	Velocity v m/s	Angular velocity ω rad/s	Current I A

Examples of bond graph models

As the bond graph method can effectively gain valuable insights about the system dynamic structure and behavior, models for the power-trains based on bond graphs can be found in several literatures. For example, bond graph modeling approach was used for wind turbines to build models of two different complexity to compare their performance in [79], where the simplified model is

shown in Figure 2.22. The physical meaning of each element is shown in Table 2.3. The models for several electric machines have been developed [80-82]. For example, a model for a BLDC PM motor was built using the MODELICA bond graph library in [80] as in Figure 2.23.

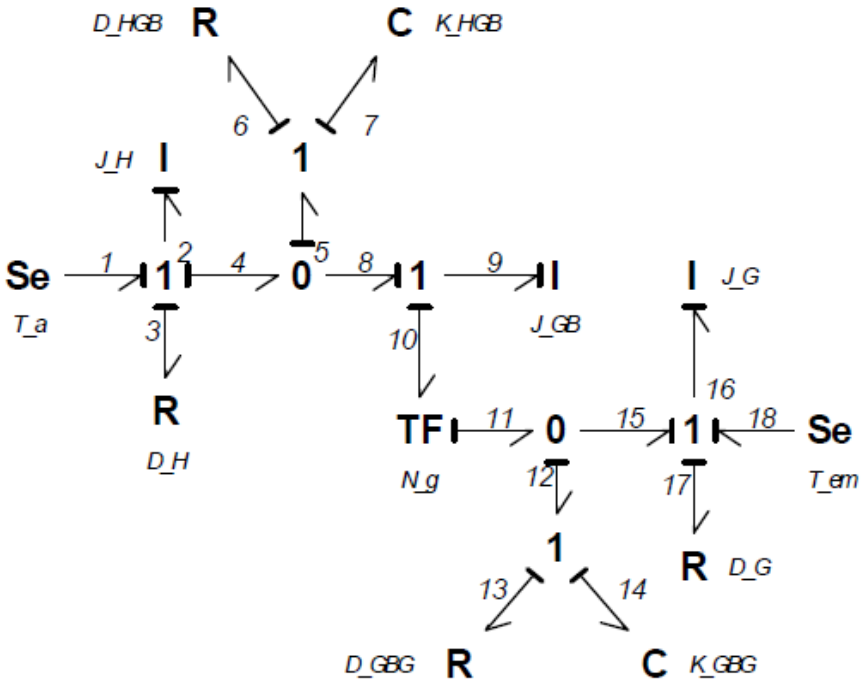

Figure 2.22 Simplified model for the wind turbine using the bond graph [79]

Table 2.3 Physical meaning of the variables in the simplified WT model [79]

Term	Meaning
T_a	Aerodynamic torque
J_H	Hub inertia
D_H	Hub damping
D_HGB	Damping between hub and gearbox
K_HGB	Stiffness between hub and gearbox
J_GB	Gear wheel inertia
N_g	Gearbox ratio
D_GBG	Damping between gearbox and generator
K_GBG	Stiffness between gearbox and generator
J_G	Generator inertia
D_G	Generator damping
T_em	Electromagnetic torque

Bond graphs provide a straightforward interpretation of physical systems, giving a clear picture of the configurations. It has a high portability because the submodels can be re-used elegantly. With the help of the existing software such as 20-SIM, ENPORT, MODELICA, and COSMO, the co-simulation can be achieved among models built with bond graphs and the ones based on block diagram. For example, the bond graph models in 20-SIM can be converted into S-functions, enabling them to be incorporated into SIMULINK. However, limitations for bond graphs include: (1) bond graphs do not resemble to the actual systems, which can be problematic for representation of complex mechanical structures, and (2) the extension from one-dimensional models to 3D multi-body systems is complex and tedious, requiring the development of vectorial bond graphs.

2.2.2.3 General mathematical descriptions

Most of the models reviewed in Section 2.2.1 are based on the mathematical equations describing the dynamics of the power-trains, as the users often have particular research purposes which cannot be met easily by the commercial software. These equations can then be solved by numerical integration methods, such as Euler's method, Newmark's method and Runge-Kutta method [24, 56, 83]. This modeling method is applicable to various types of EMPTs as far as they can be described by the mathematical equations. It is especially useful in modeling of unconventional systems which, for example, include a new machine or faulty machine [65, 66].

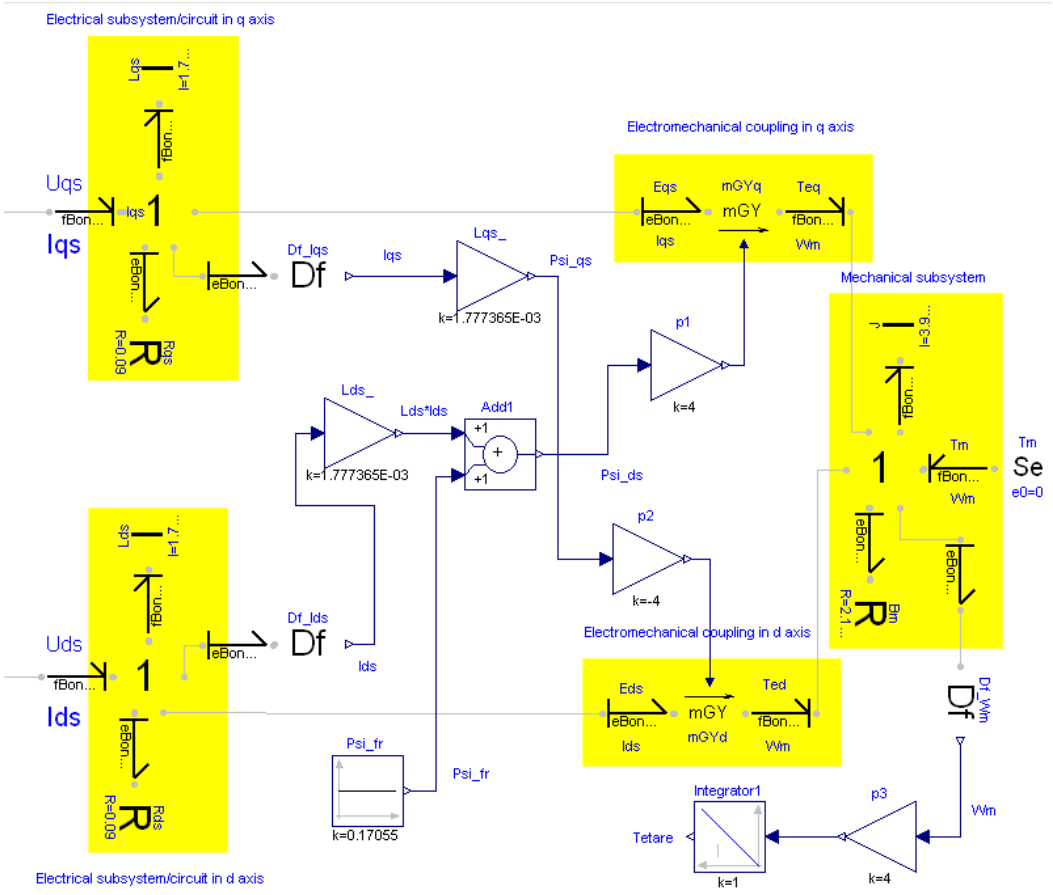

Figure 2.23 Two-axes model of a PM BLDC motor in terms of bond graphs [80]

The limitations of this general modeling approach are: (1) the derivation and programming of the equations are energy and time consuming, especially for an EMPT with complex configuration, (2) this method has a low efficiency as the model equations built for an existing power-train cannot be directly used in a power-train with new configurations, resulting in repeated effort, and (3) even for the power-trains with similar configurations, their model equations vary according to different research purposes. For instance, the backlash was included in a power-train model to explore the backlash induced dynamics in [84]. While the bearing stiffness effect was included in a model for another power-train to investigate the bearing stiffness induced dynamics in [85]. Although these two models in [84, 85] were built for the power-trains sharing

similar configurations, their equations look quite different from each other. Therefore, this modeling approach can be considered inefficient.

Thus, in summary the noteworthy arguments for the three modeling techniques are:

(1) The model library method is more efficient than other approaches as a few models for the EMPT components have already been built in the libraries. However, this method is not applicable to certain EMPTs such as the one with faulty components;

(2) Bond graph provides a straightforward insight into the power-train structures, while it will take significant effort to model a complex configuration using this technique, especially a 3D model;

(3) The general mathematical description is applicable to different kinds of power-trains for various research purposes. However, such models need to be built from scratch for each configuration or investigation area which results in repeated effort rendering this modeling method inefficient.

Therefore, there is a lack of an efficient modeling strategy that can provide an overall electro-mechanical modeling capability for EMPTs.

2.3 Condition Health Monitoring of Electro-Mechanical Power-Trains

The faults can occur in EMPTs due to many factors including fatigue, excessive temperature, over speed and over load, high corrosion, strong vibration,

improper manufacturing and maintenance, debris or dirt, and so on [86]. Based on the fault location, they can be divided into three types: mechanical, electrical, and magnetic faults as in Figure 2.24. These faults can result in potential catastrophic accidents, long down-time. And they might require expensive maintenance. Therefore, detecting such failures at an early stage can significantly reduce the associated capital losses and down-time.

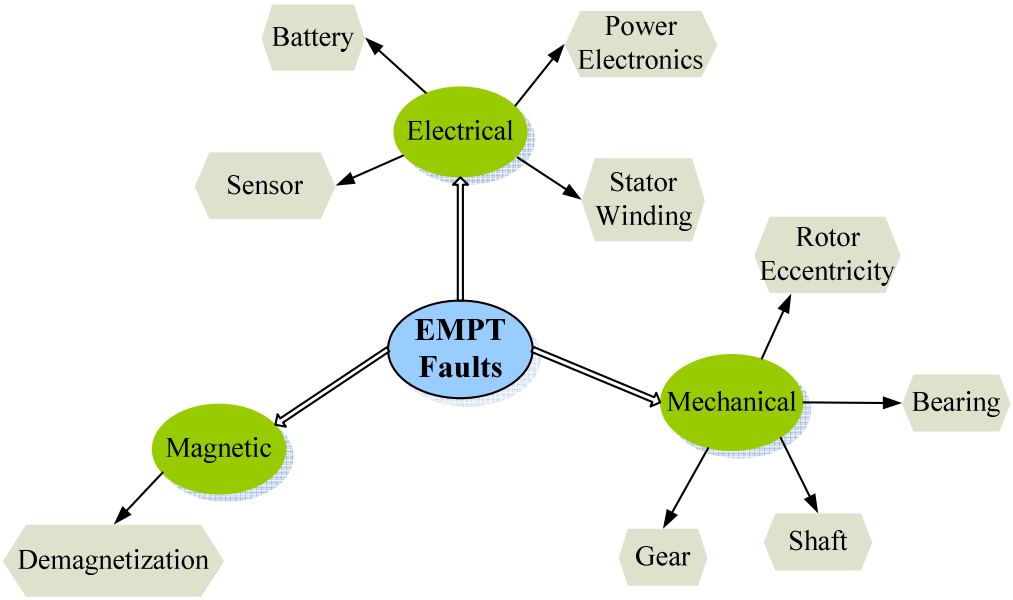

Figure 2.24 Fault types in the EMPTs

The most common mechanical faults in the power-trains include the gear tooth fault [87-93], bearing fault [94, 95], rotor eccentricity [96, 97], and shaft fault [98, 99]. For each type of these faults, examples are given in Figure 2.25. There have been several approaches to detect the mechanical faults, such as vibration analysis, acoustic analysis, oil debris analysis, thermal analysis, and motor current signature analysis (MCSA). Since the mechanical faults might produce higher temperature and larger vibration levels, the temperature and vibration

information were utilized to detect the bearing faults in [100-102]. The material loss due to the mechanical fault could result in a reduction of the contact

(a)

(b)

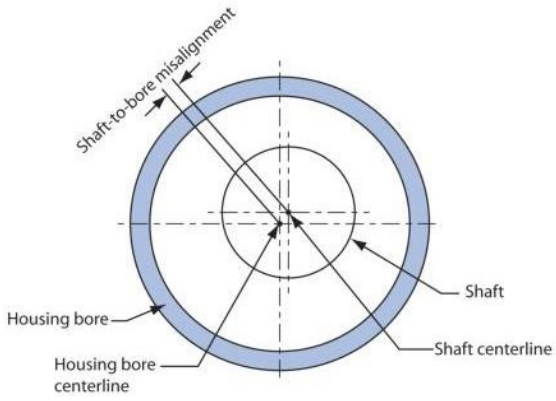

(c)

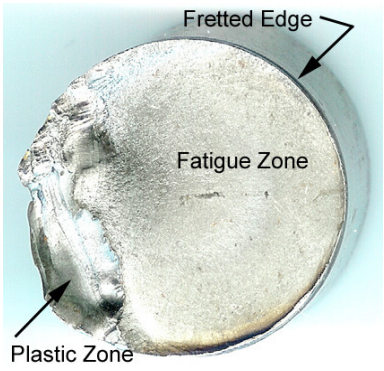

(d)

Figure 2.25 Mechanical faults (a) gear tooth crack, (b) bearing inner race defect, (c) static rotor eccentricity, and (d) shaft crack

2.3.1 Mechanical faults

stiffness, which can excite a periodical vibration signature. For example, in rolling element bearings, single point fault in the inner race usually manifests itself as a characteristic frequency in the machine vibration [94, 95] as

$$F_{IRF} = \frac{N_B}{2} F_R \left(1 + D_B \cos\theta / D_p\right) \tag{2.15}$$

where N_B is number of rolling elements, F_R is rotor frequency, D_B is ball diameter, θ is ball contact angle, and D_P is pitch diameter. Therefore, the sidebands in the vibration spectrum due to the characteristic frequencies were used as an indicator to monitor the health condition of the power-trains [87-92]. Due to the electro-mechanical interactions, the vibration signature can be reflected on the stator current of the electric machines. Therefore, the MCSA was proposed as an alternative nonintrusive method to detect the rotor eccentricity, shaft misalignment, and bearing fault [103-105]. However, the practical application of MCSA still faces some challenges, such as (1) high background noise exists in the stator current; (2) a few harmonics can be excited by the electric machines and the mechanical dynamic characteristics; and (3) the electro-mechanical interaction function has not been fully revealed.

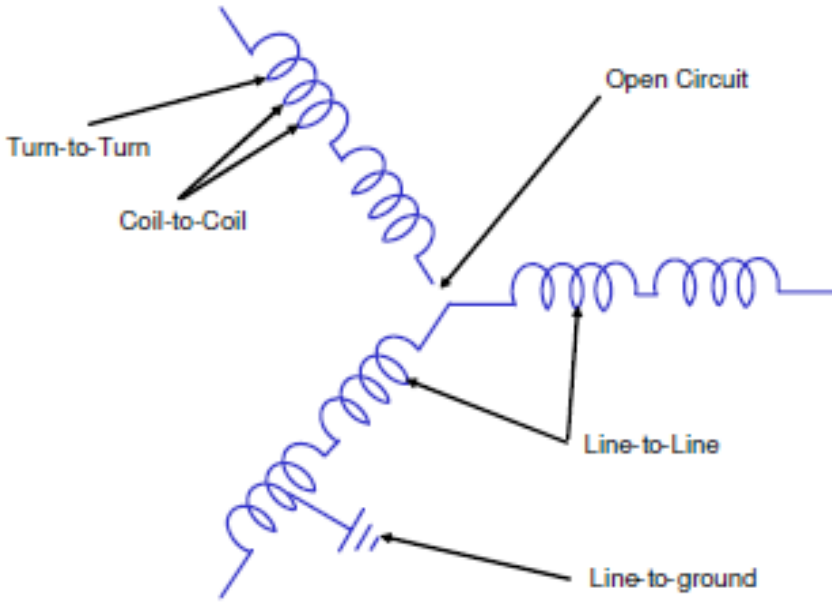

Figure 2.26 Stator winding fault types [106]

2.3.2 Electrical faults

The electrical faults in the EMPTs might occur in the stator winding, power electronics, sensors, battery, and so on. The potential stator winding faults are shown in Figure 2.26 ([106]). A few different approaches have been proposed to monitor the health of the electrical components, such as MCSA, vibration analysis, thermal analysis, electromagnetic torque analysis, and magnetic flux analysis. In [107, 108], the motor current signature was processed using the discrete wavelet transform to extract the energy distribution over different levels, which can be used as an indicator of the turn-to-turn short circuit fault in the stator winding. In [109, 110], the sidebands at the first and the second harmonics of the fundamental frequency in the stator current spectra were proposed to be a fault indicator of the current sensor measurement error. The temperature was used to monitor the health condition of the PMSM as well in [111].

2.3.3 Magnetic faults

Demagnetization can be caused by strong vibrations, overcurrent and high temperature [97]. For example, when overcurrent is fed into the stator windings, the PM might not be able to recover its initial residual flux density after cancelling the armature magnetic reaction, resulting in a demagnetization fault. A local demagnetization fault is simulated by removing a fraction of the PM materials on the rotor as shown in Figure 2.27.

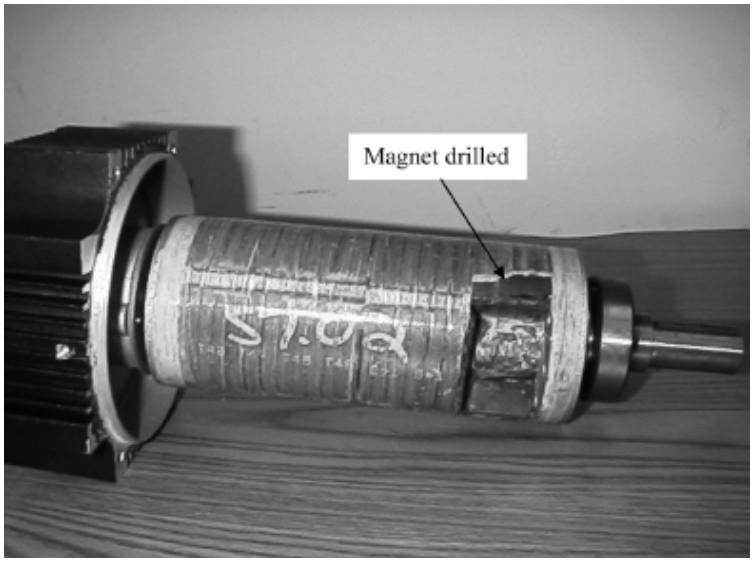

Figure 2.27 Localized demagnetization [97]

The demagnetization can be manifested itself by the instantaneous or RMS back-EMF excited by the PMSM rotor. So the estimation of the *d*-axis magnet flux in the synchronous reference frame was proposed to monitor the rotor demagnetization in [112]. A gradient-based iterative algorithm based on permeance network method was also developed to calculate the remnant induction values in the magnet regions and detect demagnetization [113].

Chapter 3 Modeling of Electro-Mechanical Power-Trains

In this chapter, a systematic co-simulation strategy is presented for the electro-mechanical power-trains (EMPTs) by integrating several modeling techniques including block diagram, multi-body system, bond graph, and finite element analysis. In Section 3.1, an overall description of the modeling strategy is provided, with details illustrated through case studies from Section 3.2 to 3.4. In Section 3.2, a gearbox-based power-train model is built through co-simulation of block diagram and multi-body system modeling approaches, which can be used to explore the nonlinear dynamics in the power-trains. In Section 3.3, a model of an electric machine connected to the load bank is demonstrated through co-simulation of finite element analysis and block diagram approach, where the built model can be used to explore the electro-mechanical interactions. In Section 3.4 a faulty EMPT is modeled using the block diagram approach, where the healthy components are directly chosen from the model library. A faulty planetary gearbox is modeled using the basic blocks and the gear meshing stiffness is estimated by finite element analysis.

3.1 Co-Simulation Strategy for Power-Trains

There are a few existing techniques to develop dynamic models for the EMPTs. However, as discussed in Section 2.2, each method has its own advantages and limitations. To achieve both a full modeling capacity and high efficiency for the EMPTs, a systematic co-simulation strategy is proposed by effectively integrating different modeling techniques as shown in Figure 3.1.

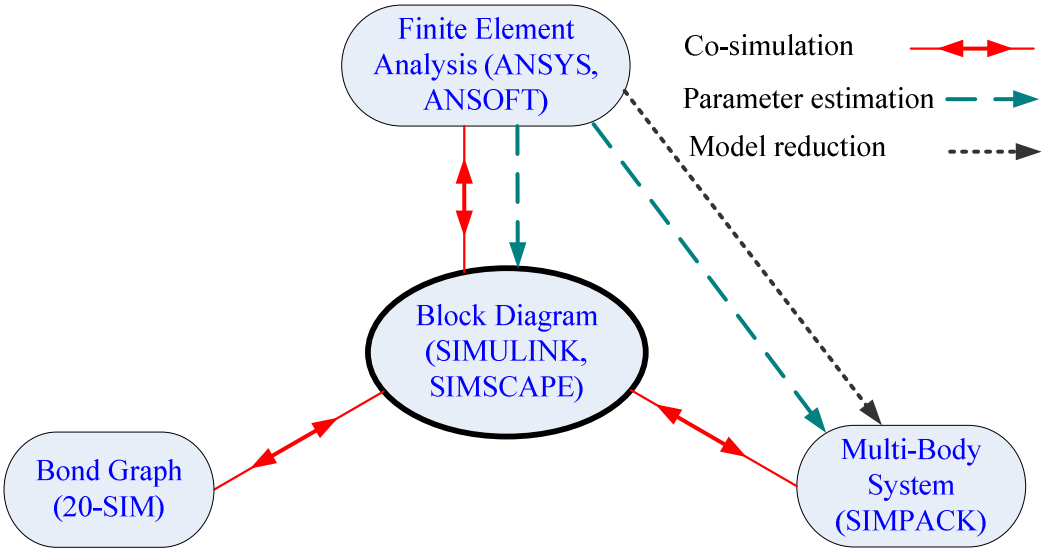

Figure 3.1 A co-simulation strategy for EMPTs

In the co-simulation strategy as in Figure 3.1, the block diagram (available in MATLAB/ SIMULINK) is utilized as a model development platform which is due to: (1) the basic mathematical blocks and the user-defined functions in SIMULINK can be used to implement different control strategies and model the unconventional machines such as a faulty component; and (2) it can provide a few graphical user interfaces [68], which can integrate SIMULINK with several other modeling techniques including bond graph (such as 20-SIM), multi-body system (such as SIMPACK), and finite element analysis (such as ANSYS and ANSOFT). Co-simulation between block diagram in SIMULINK and other modeling tools enables people to incorporate detailed nonlinear dynamics into the power-train models, where the nonlinearity is missing in SIMULINK.

Multi-body system (SIMPACK) provide basic lumped models for the mechanical components such as gears, shafts, and bearings [69]. Compared to block diagram (SIMULINK), the basic elements in SIMPACK can provide

more detailed dynamics. For example, the element incorporating the angle-varying gear meshing stiffness and backlash can be found in SIMPACK.

With the finite element analysis specialized in electromagnetics (ANSOFT), the finite element model of the electric machines can be easily built [70]. Compared to the classical Park's model built in SIMULINK, this finite element model can provide more accurate information on the electro-mechanical interactions in the EMPTs. Furthermore, it enables the users to model the complex power electronics architectures in ANSOFT/SIMPLORER.

Bond graph (20-SIM) can represent the EMPT systems using physical modeling concept. Co-simulation between SIMULINK and 20-SIM is able to model part of the system using 20-SIM. For example, a dynamic model for the heating, ventilation, and air-conditioning systems was built based on the co-simulation [114], where the control strategy was implemented in SIMULINK and the physical model in 20-SIM was translated into an S-Function of SIMULINK.

Finally, a few model parameters can be estimated based on general finite element analysis (ANSYS). For example, the gear teeth meshing stiffness in the gearbox was estimated using ANSYS [115].

3.2 Model 1: Co-Simulation of Multi-Body System and Block Diagram

3.2.1 Multi-body system modeling approach

As a typical multi-body system simulation software, SIMPACK can be used for dynamics analysis of mechanical or mechatronic systems [69]. It is used

primarily within automotive, engine, power transmission, railway, and wind energy industrial sectors. It is operated via a graphical user interface, enabling the users to generate and solve virtual 3D models in order to predict and visualize the motion, coupling forces and stresses. The user inputs parameters describing the system to be simulated, such as mass and inertias of each body, and then the kinematic loops can be created by applying the pertinent joints, constraints, and forces. SIMPACK also provides a force element library containing specific force elements tailored for power-train simulation. Finally, based on the model topology SIMPACK creates the motion equations internally and allows the users to choose different options for the time integration.

3.2.2 A nonlinear model for a gearbox-based power-train

A typical nonlinear gearbox-based power-train is used as an example to illustrate the co-simulation between SIMULINK and SIMPACK as shown in Figure 3.2. The nonlinear dynamics inside the gearbox can be affected by several important gear parameters, such as backlash, meshing stiffness, damping, and geometry [12, 116]. All these mechanical parameters can be easily setup in SIMPACK. The speed control strategy can be implemented through the existing control toolbox in SIMULINK. Furthermore, the co-simulation interface “SIMAT” can integrate SIMPACK and SIMULINK together. SIMAT is designed to using the TCP/IP protocol to exchange the results with a given time step between SIMPACK and SIMULINK, enabling to run the simultaneous co-simulation model.

In Figure 3.2(a), a spur gearbox driven by pulsating torque is modeled by the co-simulation between SIMULINK and SIMPACK. The pinion gear is connected to a speed source through a flexible shaft, where the speed source can be modeled in SIMULINK. And the applied load torque on the wheel gear depends on its angular speed. The 3D visual spur gearbox model is shown in Figure 3.2(b). In Figure 3.2(c), the 2D topology diagram of the model is shown where the applied torque/force element and the gear interaction can be observed. The elements from SIMPACK model library to model the system are shown in Table 3.1. The Primitive "25: Gear Wheel" can be used to define the gear geometry by setting up parameters such as module, pressure angle, helix angle, backlash, flank width, addendum and dedendum coefficients, and the modification factor. The Force Element "225: Gear Pair" can be used to model the gear meshing stiffness as well as to detect the gear contact condition.

Table 3.1 SIMPACK library elements used to model components

Component	SIMPACK element
Gears	Primitive 25: Gear wheel
Gear meshing stiffness and damping	Force element 225: Gear pair
Driving torque	Force element 93: Force/Torque by u(t) Cmp
DOF constraint	Joints

3.3 Model 2: Co-Simulation between Finite Element Method and Block Diagram

3.3.1 Introduction of ANSOFT

ANSOFT consists of modules such as MAXWELL and SIMPLORER which can be used to study the electromagnetics related problems [70]. In electric

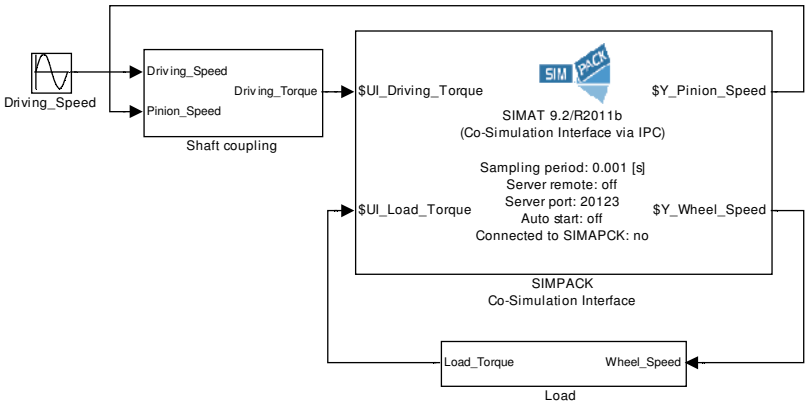

(a)

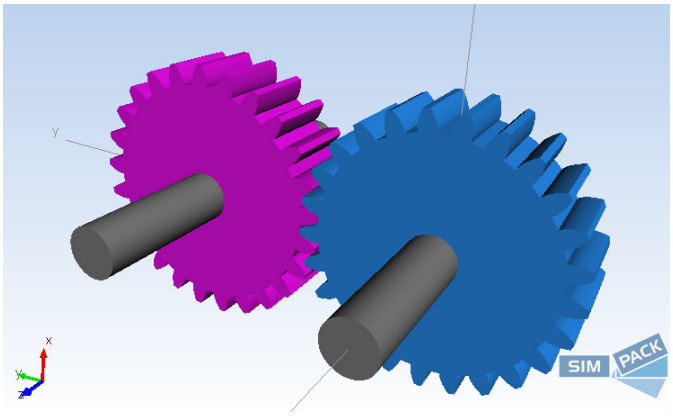

(b)

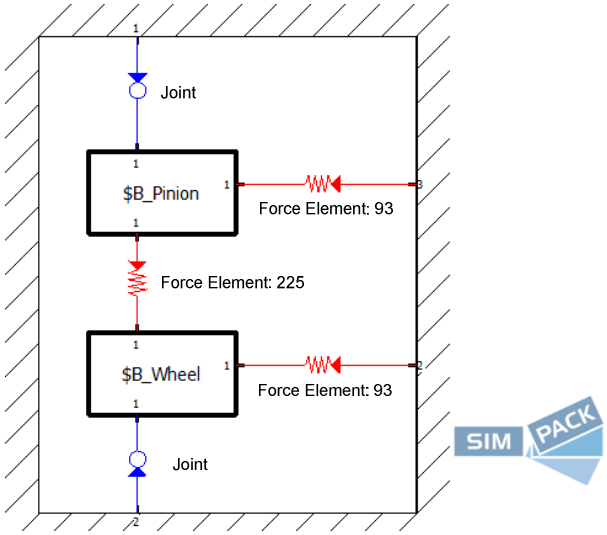

(c)

Figure 3.2 Model of a spur gearbox model (a) Co-simulation diagram in SIMULINK, (b) 3D visual in SIMPACK, and (c) 2D topology diagram in SIMPACK

machines, the higher order harmonics can be excited in the stator current and electromagnetic torque by factors such as slot effect, winding configuration and magnetic saturation, [36-39]. These harmonics can excite significant amount of vibration and noise in the power-trains. Furthermore, the harmonics in the stator current can deteriorate the fault detection performance based on motor current signature analysis. Compared to Park's model which can only be used to investigate the linear dynamics in the electric machines, MAXWELL together with RMxprt (Rotational Machine Expert) is capable of building a nonlinear dynamic model for the electric machine with finite element method. SIMPLORER is an intuitive, multi-domain and multi-technology simulation module which can be used to model the power electronic circuits with complex architectures. Furthermore, co-simulation between SIMULINK and SIMPLORER enables the detailed simulation of the electrical drive systems comprised of electric machines, the power electronics, and the controller.

3.3.2 Modeling of electric machines connected to resistive load

The permanent magnet synchronous machines (PMSMs) have high energy efficiency and can be found in lots of applications, such as hybrid electric vehicles (HEVs), wind turbines and aircrafts [117, 118]. By inputting the design parameters of the PMSM into RMxprt such as the geometry and materials, the stator winding diagram and cross-section can be obtained as shown in Figure 3.3(a) and (b). With the provided geometry and material information, a 2D/ 3D

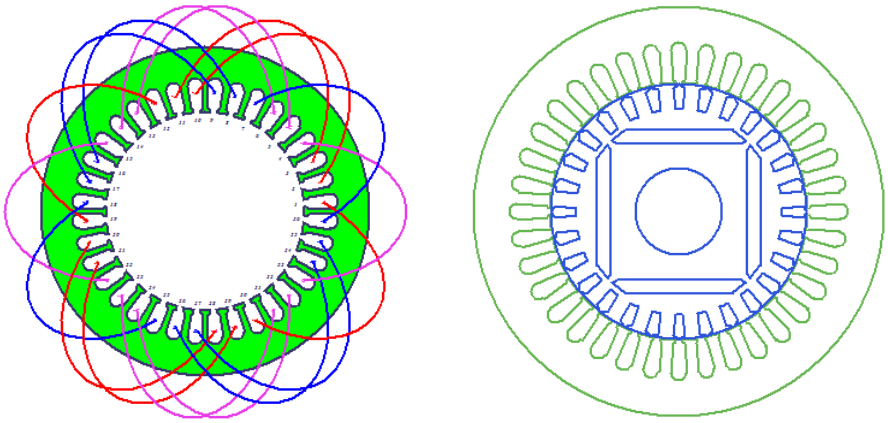

(a) (b)

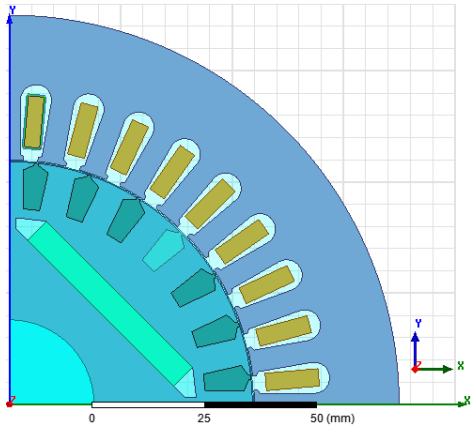

(c)

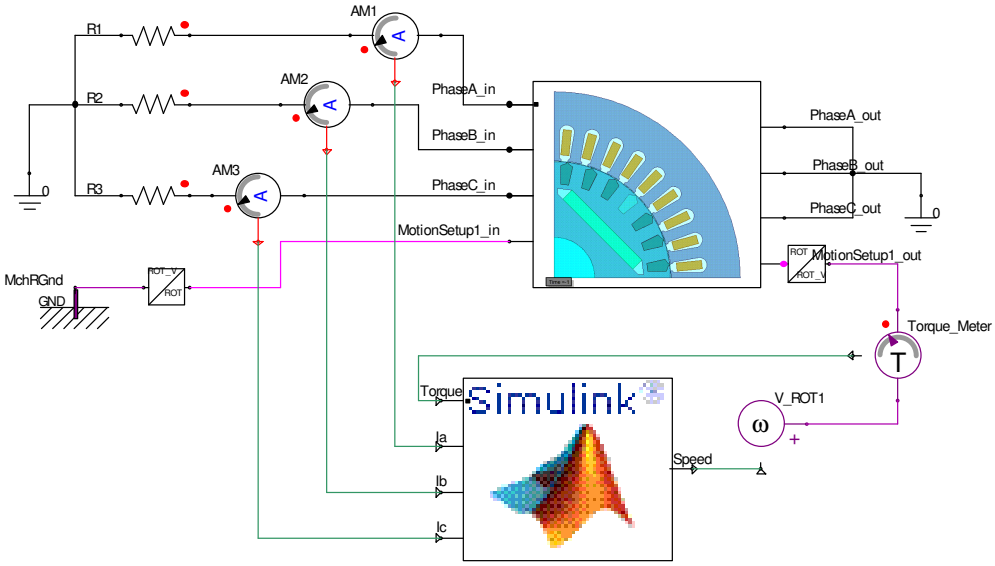

(d)

Figure 3.3 PMSM drives model (a) Stator winding diagram, (b) Cross section, (c) 2D MAXWELL model, and (d) Model in SIMPLORER coupled with SIMULINK

finite element model can be further obtained using MAXWELL as shown in Figure 3.3(c). The boundary conditions of the finite element model can be automatically defined by MAXWELL, saving a lot of efforts. Then, this finite element model can be coupled with the electrical circuits or power electronics built in SIMPLORER. A co-simulation between SIMPLORER and SIMULINK enables people to control the electrical drive system in SIMPLORER by the controller designed in SIMULINK. A detailed nonlinear dynamic model for a PMSM connected to the power load can be built as in Figure 3.3(d), where the PMSM works as a generator with its running speed controlled by SIMULINK. The driving torque applied on the PMSM and the stator current are measured in SIMPLORER and then transmitted to SIMULINK.

3.4 Model 3: Model Development using Block Diagram

3.4.1 Existing blocks in SIMULINK

In SIMULINK, a few basic blocks are provided for the users to build their own models [52] as shown in Figure 3.4, such as Sum block, Product block, Gain block, Integrator block, Function block (to describe the mathematical function), Signal Generator block (to generate the desired signal), Workspace block (to output the simulation results to MATLAB workspace), and Subsystem block (to represent the sub-models).

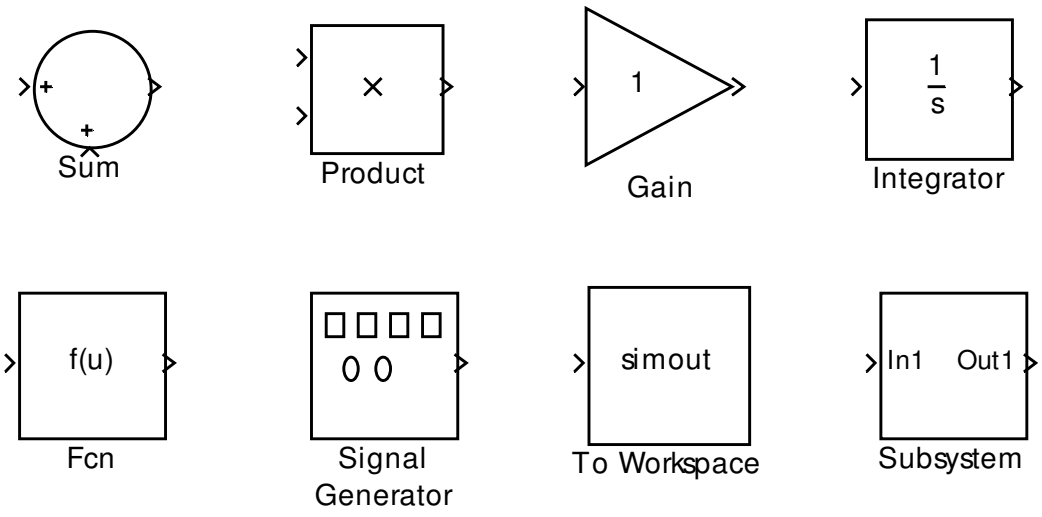

Figure 3.4 Basic blocks in SIMULINK

3.4.2 Modeling of faulty planetary gearbox in SIMULINK

Planetary gearboxes are preferred in many power-trains applications, such as wind turbines, maritime and automobiles. In a planetary gearbox, there is a sun gear, an annulus gear, and a carrier with several planet gears mounted as shown in Figure 3.5. In the shown configuration, the annulus gear is fixed and there are four planets. The gear tooth fault frequently occurs due to factors such as heavy load duty and bad lubricant conditions [87-89, 92]. If the tooth fault occurs, whenever other gears pass through the faulty location, a local reduction in the gear meshing stiffness will happen corresponds to the missing materials as illustrated later in Figure 3.11 (in Section 3.4.2.3). Since the meshing stiffness of the faulty tooth cannot be modeled in SIMPACK, the basic blocks in SIMULINK are utilized to model the faulty planetary gearbox.

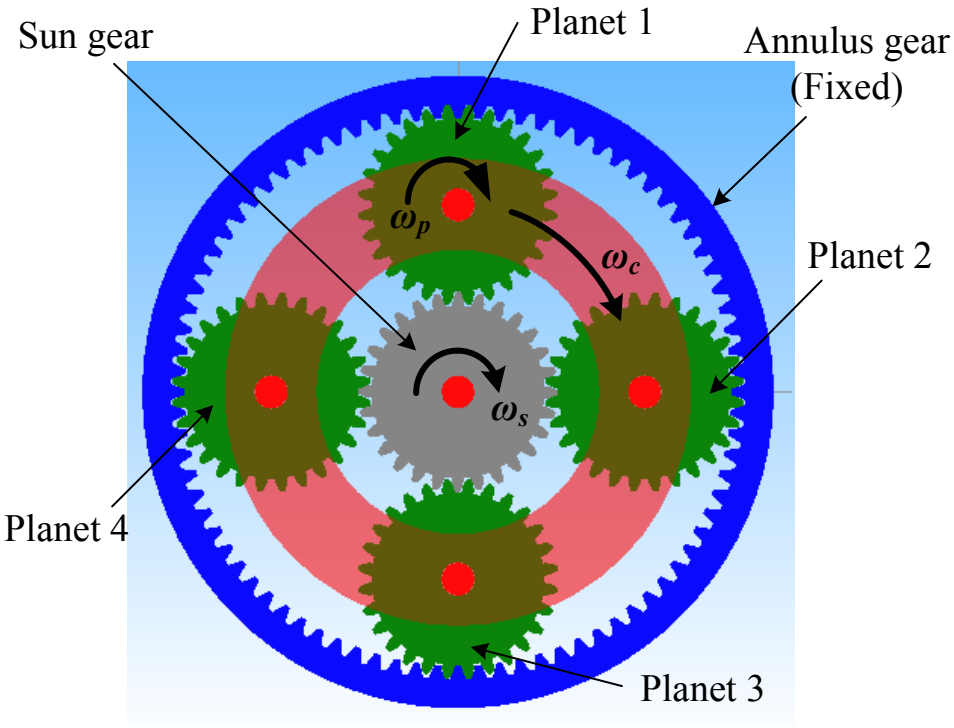

Figure 3.5 A planetary gear set with four planets and fixed annulus gear

3.4.2.1 Motion equations of planetary gearbox

A lumped model can be built for the planetary gearbox shown in Figure 3.5, and further represented as a matrix form (Eqn. 3.1 [57, 66])

$$\mathbf{M}\ddot{\mathbf{Q}}+\mathbf{C}\dot{\mathbf{Q}}+\mathbf{K}\mathbf{Q}=\mathbf{T} \tag{3.1}$$

As the rotational DOFs have significant effect on the torsional dynamics of the gearbox coupled with an electric machine, the vector **Q** only contains all the rotational DOFs as

$$\mathbf{Q}=\begin{bmatrix}\theta_s & \theta_{p1} & \theta_{p2} & \theta_{p3} & \theta_{p4} & \theta_c\end{bmatrix}^T \tag{3.2}$$

M is the mass matrix, **C** is the damping matrix, **K** is the stiffness matrix, the subscript *pi* represents the planet where *i*=1 to 4, the subscripts *s* and *c* represent the sun gear and carrier, and **T** is the external applied torque vector as

$$\mathbf{M}=\begin{bmatrix} J_s & & & & & \\ & J_p & & & & \\ & & J_p & & & \\ & & & J_p & & \\ & & & & J_p & \\ & & & & & J_c+4M_p r_{bc}^2 \end{bmatrix} \tag{3.3a}$$

$$\mathbf{C}=\begin{bmatrix} r_{bs}^2\sum_{i=1}^{4}c_{spi} & r_{bp}r_{bs}c_{sp1} & r_{bp}r_{bs}c_{sp2} & r_{bp}r_{bs}c_{sp3} & r_{bp}r_{bs}c_{sp4} & -r_{bc}r_{bs}\sum_{i=1}^{4}c_{spi} \\ r_{bs}r_{bp}c_{sp1} & r_{bp}^2\left(c_{ap1}+c_{sp1}\right) & 0 & 0 & 0 & r_{bc}r_{bp}\left(c_{ap1}-c_{sp1}\right) \\ r_{bs}r_{bp}c_{sp2} & 0 & r_{bp}^2\left(c_{ap2}+c_{sp2}\right) & 0 & 0 & r_{bc}r_{bp}\left(c_{ap2}-c_{sp2}\right) \\ r_{bs}r_{bp}c_{sp3} & 0 & 0 & r_{bp}^2\left(c_{ap3}+c_{sp3}\right) & 0 & r_{bc}r_{bp}\left(c_{ap3}-c_{sp3}\right) \\ r_{bs}r_{bp}c_{sp4} & 0 & 0 & 0 & r_{bp}^2\left(c_{ap4}+c_{sp4}\right) & r_{bc}r_{bp}\left(c_{ap4}-c_{sp4}\right) \\ -r_{bs}r_{bc}\sum_{i=1}^{4}c_{spi} & r_{bp}r_{bc}\left(c_{ap1}-c_{sp1}\right) & r_{bp}r_{bc}\left(c_{ap2}-c_{sp2}\right) & r_{bp}r_{bc}\left(c_{ap3}-c_{sp3}\right) & r_{bp}r_{bc}\left(c_{ap4}-c_{sp4}\right) & r_{bc}^2\sum_{i=1}^{4}\left(c_{spi}+c_{api}\right) \end{bmatrix} \tag{3.3b}$$

$$\mathbf{K}=\begin{bmatrix} r_{bs}^2\sum_{i=1}^{4}k_{spi} & r_{bp}r_{bs}k_{sp1} & r_{bp}r_{bs}k_{sp2} & r_{bp}r_{bs}k_{sp3} & r_{bp}r_{bs}k_{sp4} & -r_{bc}r_{bs}\sum_{i=1}^{4}k_{spi} \\ r_{bs}r_{bp}k_{sp1} & r_{bp}^2\left(k_{ap1}+k_{sp1}\right) & 0 & 0 & 0 & r_{bc}r_{bp}\left(k_{ap1}-k_{sp1}\right) \\ r_{bs}r_{bp}k_{sp2} & 0 & r_{bp}^2\left(k_{ap2}+k_{sp2}\right) & 0 & 0 & r_{bc}r_{bp}\left(k_{ap2}-k_{sp2}\right) \\ r_{bs}r_{bp}k_{sp3} & 0 & 0 & r_{bp}^2\left(k_{ap3}+k_{sp3}\right) & 0 & r_{bc}r_{bp}\left(k_{ap3}-k_{sp3}\right) \\ r_{bs}r_{bp}k_{sp4} & 0 & 0 & 0 & r_{bp}^2\left(k_{ap4}+k_{sp4}\right) & r_{bc}r_{bp}\left(k_{ap4}-k_{sp4}\right) \\ -r_{bs}r_{bc}\sum_{i=1}^{4}k_{spi} & r_{bp}r_{bc}\left(k_{ap1}-k_{sp1}\right) & r_{bp}r_{bc}\left(k_{ap2}-k_{sp2}\right) & r_{bp}r_{bc}\left(k_{ap3}-k_{sp3}\right) & r_{bp}r_{bc}\left(k_{ap4}-k_{sp4}\right) & r_{bc}^2\sum_{i=1}^{4}\left(k_{spi}+k_{api}\right) \end{bmatrix} \tag{3.3c}$$

$$\mathbf{T}=\begin{bmatrix} T_s & 0 & 0 & 0 & 0 & T_c \end{bmatrix}^T \tag{3.4}$$

where J is the inertia of the gear/carrier, θ is the angular displacement of the gear/carrier, T is the applied torque, and r_b is the base radius of the gear. c is the gear damping coefficient, and k is the gear meshing stiffness. The subscript a, represents the sun gear. For example, the stiffness between the annulus gear and the planet 1 is

$$k_{ap1}=k_{\min}+\left(k_{\max}-k_{\min}\right)\cdot\text{square}\left[N_a\left(\theta_c+\phi_{ap1}\right)\right]-\Delta k\cdot\text{square}\left(\theta_c+\phi_{ap1}\right) \tag{3.5}$$

where k_{min} is the low stiffness when less teeth pair are engaged, k_{max} is the high stiffness with more teeth pair are engaged, N_a is the number of teeth on the

annulus gear, ϕ_{ap1} is the relative phase for the gear pair comprised of the annulus gear and planet 1, Δk is the stiffness reduction due to the annulus gear tooth fault, and the function "square" represents the square function with a period 2π and amplitude 1.

3.4.2.2 Block diagram of planetary gearbox

In SIMULINK, the integration operator can provide better numerical convergence performance in solving the differential equations than the differential operator in the presence of the numerical error. To numerically solve Eqn. 3.1 in SIMULINK, it can be rewritten as

$$\mathbf{Q} = \mathbf{M}^{-1} \int \left[\iint (\mathbf{T} - \mathbf{K}\mathbf{Q}) dt - \mathbf{C}\mathbf{Q} \right] dt \tag{3.6}$$

Eqn. 3.6 is implemented in SIMULINK as in illustrated Figure 3.6 to 3.8. The overall block diagram is shown in Figure 3.6(a), where the torque vector **T** is represented by a subsystem block as in Figure 3.6(b). The stiffness matrix **K** and the damping matrix **C** share similar forms as in Eqn. 3.3, therefore only **K** is presented. According to Eqn. 3.5, if a gear tooth fault occurs, the corresponding gear meshing stiffness will be composed of two parts: (1) the one for a healthy gearbox, and (2) the stiffness reduction due to the gear tooth fault. For example, k_{ap1} between the annulus gear and planet 1 is shown in Figure 3.6(c). Furthermore, the gear meshing stiffness functions between the annulus gear and all the planets are shown as in Figure 3.7 (a). According to Eqn. 3.3(c), the stiffness matrix **K** can be obtained as in Figure 3.7(b), where $k1$ to $k6$ represent each row vector of **K**. The first row vector $k1$ is shown as an example in Figure 3.7(c). The multiplication of **K** and **Q** is decomposed into the

multiplication of each row vector (*k*1 to *k*6) with **Q** as in Figure 3.8(a) with the expression *k*1***Q** shown in Figure 3.8(b). Then, the integration operation is shown in Figure 3.8(c). Finally, the multiplication with inversed mass matrix is shown in Figure 3.8(d). The built model for the faulty planetary gearbox can be included in an overall model just like other general blocks in SIMULINK. With this approach, the gearboxes with different types of fault can be developed. By incorporating these gearbox models one by one into an overall power-train model, all the concerned faulty cases can be studied with easy effort. Therefore, this approach brings with a high efficiency.

3.4.2.3 Gear meshing stiffness estimation

The gear meshing stiffness are determined by the bending and fillet-foundation stiffness of each meshing tooth, and Hertzian contact stiffness between the meshing teeth as in [119]. The irregular shape of the faulty gear tooth makes the estimation of stiffness become even more complicated, so ANSYS is used to estimate this value. The meshing pair between the annulus gear and the planet in a planetary gearbox (with parameters in Table 3.2) are used as an example to show the influence of the missing material on the meshing stiffness, where one tooth on the annulus gear loses 1/3rd tooth width and the annulus gear is fixed on the housing as in Figure 3.9(a). In the simulation, a driving torque 110.4N.m is applied on the planet through the nodes on its inner race, where the coordinate system of these nodes needs to be rotated onto the cylindrical coordinate before applying the torque. The gear tooth contact is setup through contact elements 170 and 174.

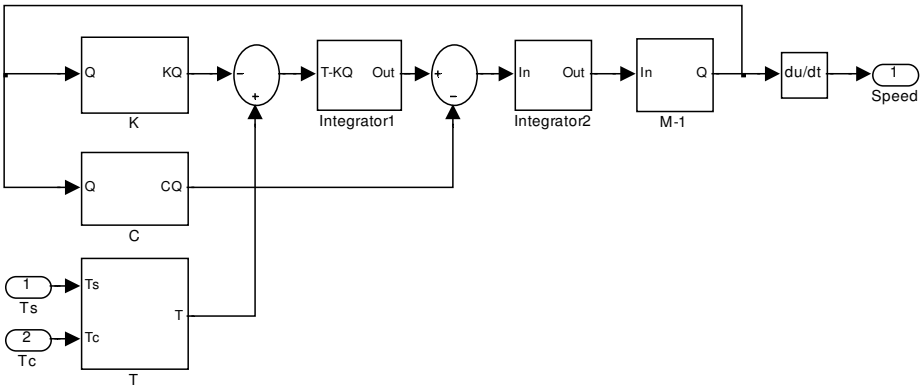

(a)

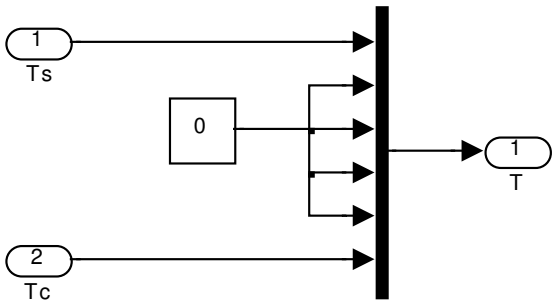

(b)

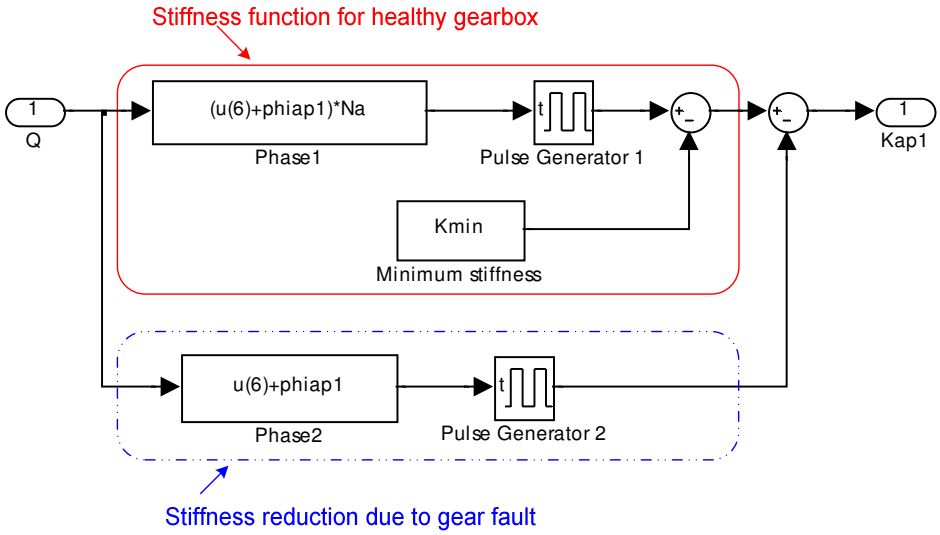

(c)

Figure 3.6 Block diagram of planetary gearbox in SIMULINK-Section 1 (a) overall picture, (b) torque vector **T**, (c) stiffness k_{ap1} between the annulus and planet 1

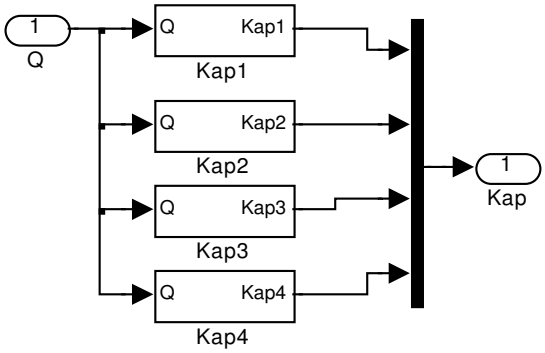

(a)

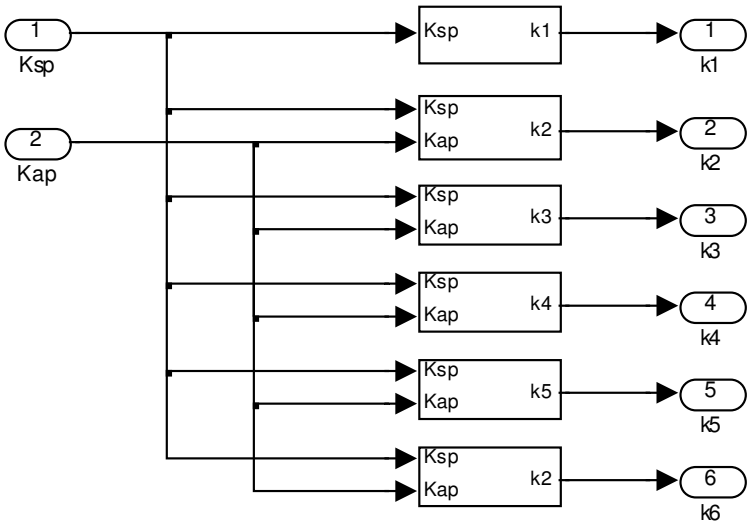

(b)

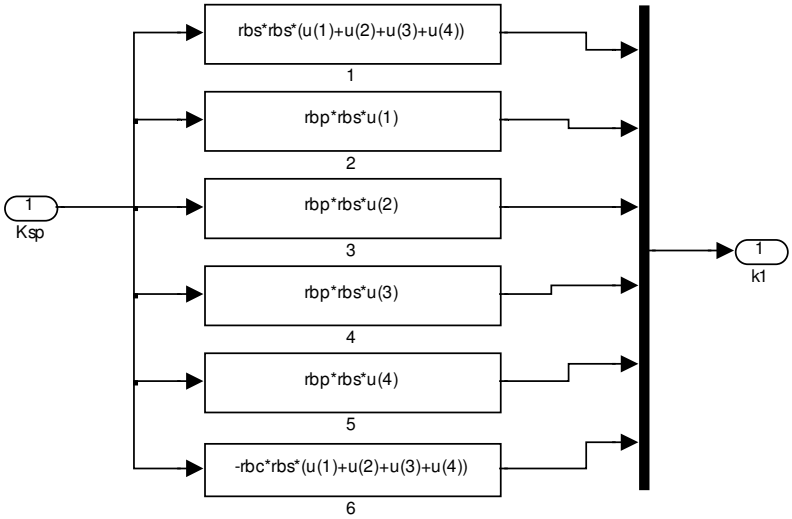

(c)

Figure 3.7 Block diagram of planetary gearbox in SIMULINK – Section 2 (a) stiffness vector between the annulus and planets K_{ap}, (b) stiffness matrix **K**, (c) row vector $k1$

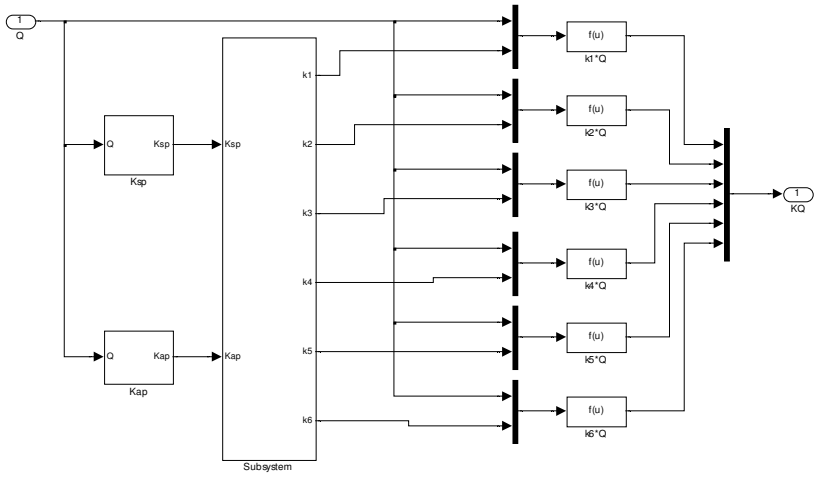

(a)

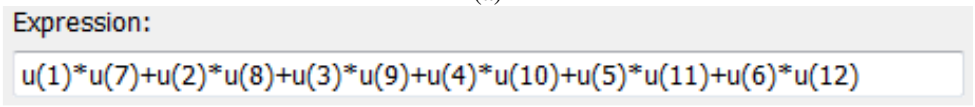

(b)

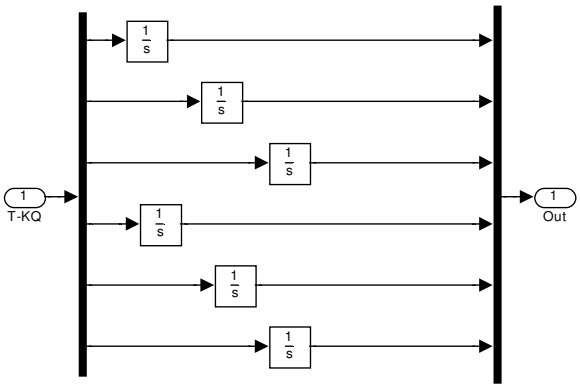

(c)

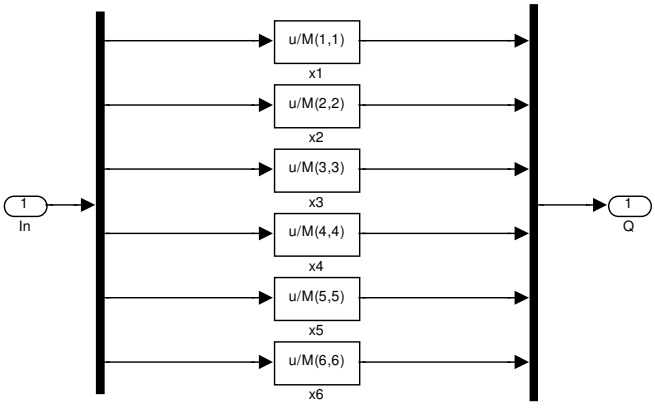

(d)

Figure 3.8 Block diagram of planetary gearbox in SIMULINK – Section 3 (a) multiplication of **K** and **Q**, (b) multiplication between $k1$***Q**, (c) integrator operation, and (d) multiplication with $\mathbf{M}^{-1}$

Table 3.2 Parameters of the annulus and planet gear

Parameter	Annulus	Planet
Material/Density ρ (Kg/m^3)	Steel / 7.87×10^3	
Young modulus E (Pa)	190×10^9	
Poisson coefficient v_{pc}	0.27	
Number of tooth N_a, N_p	84	28
Module m(mm)	2	
Pressure angle α(°)	20	
Tooth face width L (mm)	30	

With the applied torque, the Von Mises stress obtained in ANSYS is shown in Figure 3.9, where Figure 3.9(a) shows the fault tooth location while Figure 3.9(b) shows the healthy tooth location. The corresponding displacement contour of the gear pair is shown in Figure 3.10. With the applied torque and the obtained displacement, the corresponding gear tooth meshing stiffness can be calculated easily. By rotating the gear pair with a small fractional angle each time, the gear meshing stiffness for an overall meshing period can be achieved as shown in Figure 3.11. Looking at the faulty location, when one teeth pair are engaged, the local stiffness loss is 0.3×10^8 N/(m.rad). When two teeth pairs are engaged, the local stiffness loss is only 0.2×10^8 N/(m.rad) as the load is distributed on two teeth pairs. Furthermore, from the Von Mises stress contours obtained under both the faulty and healthy conditions in Figure 3.9, it can be found that the faulty tooth introduce a higher contact stress due to the missing material. Therefore, the breaking process could be accelerated by the unevenly distributed stress along the axial direction.

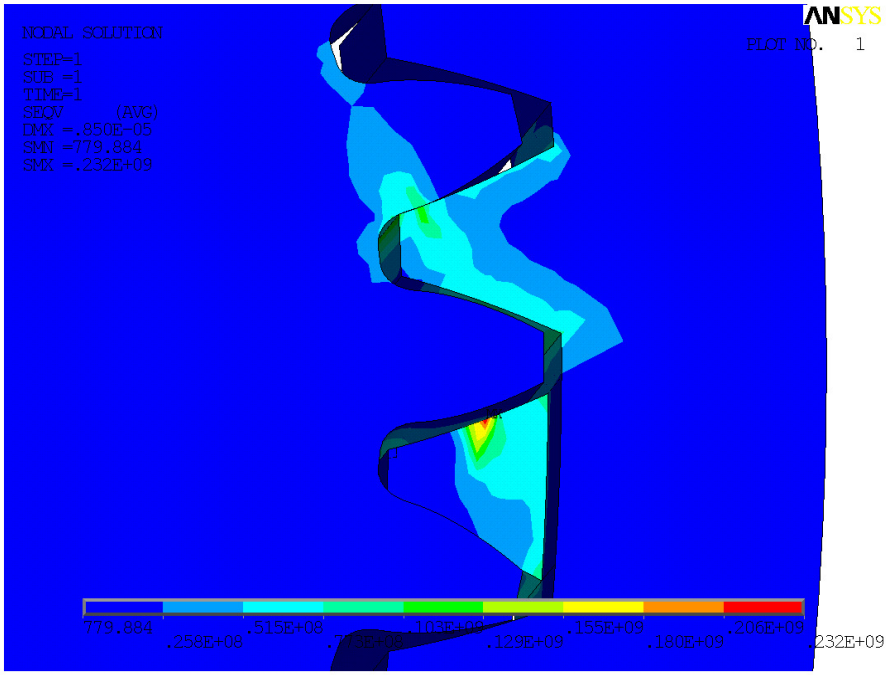

(a)

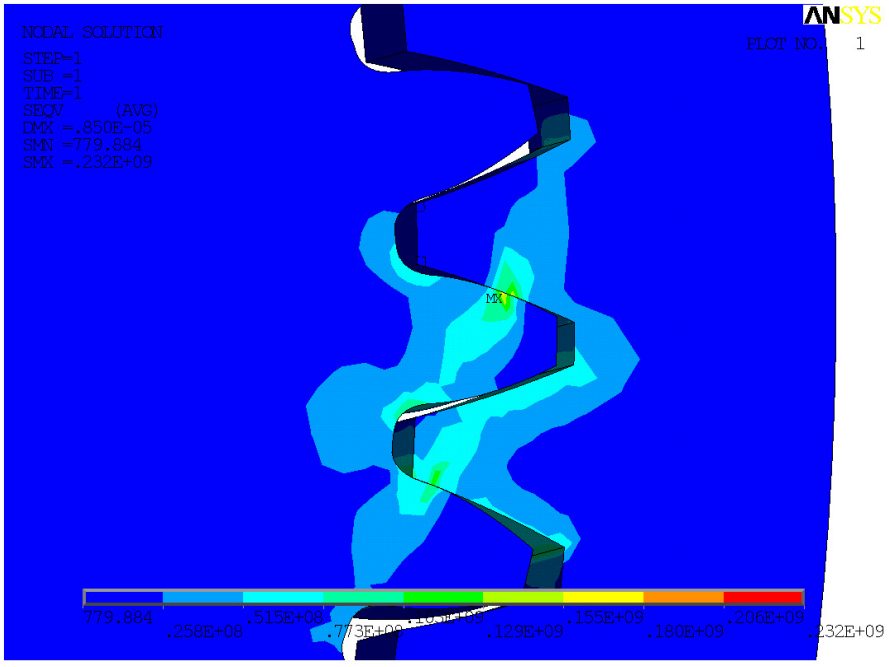

(b)

Figure 3.9 Von Mises stress of the gear pair (a) faulty location, and (b) healthy location

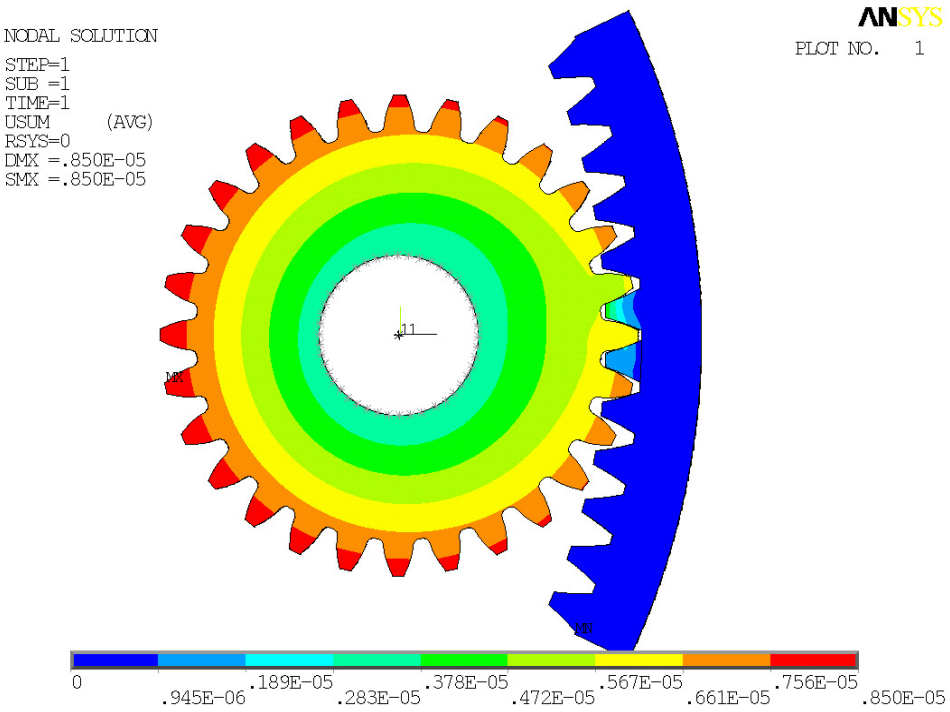

Figure 3.10 Displacement of the gear pair

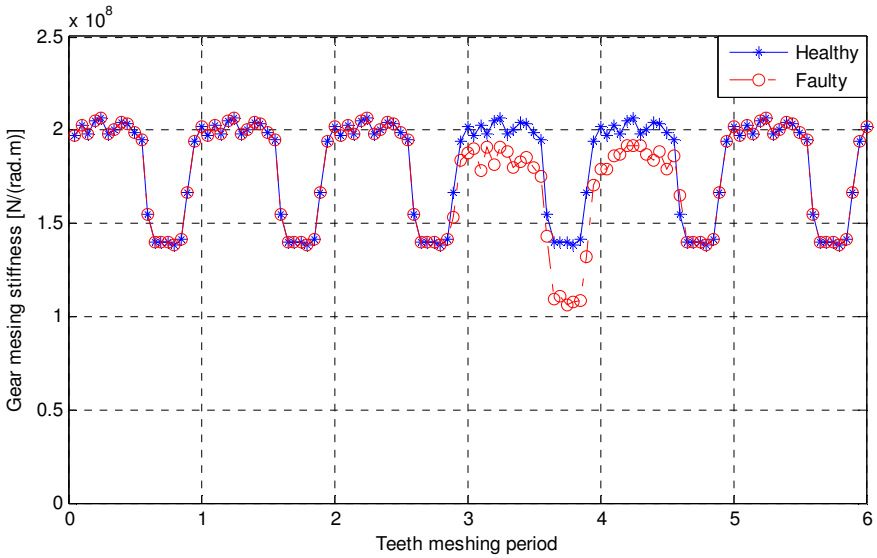

Figure 3.11 Gear meshing stiffness of the annulus-planet gear pair

Chapter 4 An Analytical Method to Evaluate Gear Parameters Effect on Rattling Noise

4.1 Introduction

Gear rattle is a common occurrence in transmission systems, such as those in vehicles and marine vessels, under lightly loaded conditions [23, 24, 120]. When gear rattle occurs, the gear teeth oscillate within the backlash while undergoing several consecutive tooth impacts that produce a high level of vibration and noise. This noise resulting from gear rattle is an important source of passenger discomfort in automotive applications [61, 62, 121, 122]. The occurrence and severity of gear rattle induced impacts and emitted noise is influenced by different components of power-trains such as the diesel engine, the flywheel, the clutch, and the gearbox. Recent technological improvements have significantly reduced the size of engines and flywheel, as well as mitigated the frictional torques through improvements in bearings and lubricants technology, which can increase the occurrence of gear rattle thus bringing it in focus [120, 123, 124]. Therefore, to avoid expensive modifications later, it is crucial to consider the gear rattle during the design stage of the gearbox itself.

Previous research has investigated the influence of the various transmission components on the gear rattle. The effect of the inertia of the flywheel, as well as the stiffness and hysteresis of the clutch on the gear impact has been investigated through stiffness varying multi-DOF lumped parameter models of the transmission [61, 62, 125]. It was shown that by increasing the flywheel inertia, reducing the clutch rigidity and selecting adequate clutch hysteresis

torque, the speed fluctuation transmitted from the diesel engine to the gearbox can be reduced, thereby reducing gear rattle severity. Gearbox parameters can also affect the rattle noise level [12, 116], e.g., an increase of backlash and gear meshing stiffness can produce more rattling noise, while an increase of damping factor and the wheel gear inertia can reduce the noise level. To quantify the effect of different gear parameters on the rattling noise level, both numerical modeling and experimental based approaches have been developed. For example, a two-DOF lumped parameter model was developed for a spur gear pair to explore the effect of gear backlash and inertia in [116, 126]. However, it is time-consuming to assess gear parameters' effect on the rattle noise by individual numerical simulation that evaluates each parameter one by one. Furthermore, investigations on power-trains with various configurations and parameters do not provide an insight regarding the final expected rattle noise as a combination of all these input variables. Experiment based approaches have been carried out to investigate the effect of the variation of gear parameters on rattle noise as well [12, 116]. However, an experimental investigation of gear parameters on rattle noise requires manufacturing, installation and commissioning of gears with different dimensions, which is both time-consuming and expensive. Further, the experimental results are influenced by errors in manufacturing and installation, such as gear profile error, shaft misalignment and eccentricity [124, 127]. Therefore, an analytical approach to evaluate the importance of gear parameters' effect on the gear rattle noise is required. According to [116, 128, 129], the root mean square (RMS) value of the wheel gear acceleration is proportional to the noise level during the gear

rattle and has been used as an indicator of the sound perception. Since the pure rotational motion of the gear bodies produce negligible noise, the rattle noise can be attributed to the period when gear impact occurs. Furthermore, even though several consecutive impacts can occur gear teeth face at one side before the gear teeth mesh together again, the first impact has the most dominant energy as the subsequent impacts can get dampened quickly [130, 131]. It can be deduced that the rattling noise level is mainly determined by the RMS value of the wheel gear acceleration during the first impact period, which is used in this work to estimate its value analytically.

Therefore, in this chapter the acceleration magnitude due to gear rattle is analytically evaluated to investigate the contribution of different gear parameters on the gear rattle. A two-DOF model developed for a typical power-train configuration is simplified to a single-DOF equation of motion to describe the teeth impact. This simplified model sufficiently describes the wheel gear vibration within the backlash. The analytical solution obtained from this model is used to evaluate the RMS value of the acceleration of the wheel gear due to teeth impacts during gear rattle. This proposed formulation to access the gear rattle noise is verified using a dynamic model of a typical transmission system built in SIMPACK software environment. Previously reported experimental results in [12, 116] are also shown to agree with the proposed method. Thus, the proposed evaluation method for estimating the acceleration RMS value during gear impacts can quantify the influence of gear parameters on the rattle noise, and can thus provide an easy design guideline to determine the expected severity of gear rattle at the gearbox design stage.

4.2 Modeling of a Simplified Transmission

4.2.1 Gearbox parameters

Gear meshing stiffness and backlash

During operation, the gear teeth can bend along the line of action that is due to material elasticity. The gear teeth meshing stiffness k_g can be determined by using the standards mentioned in [132, 133]. The backlash $2b_{ls}$ is the amount of clearance between two mating pair of gear teeth that is usually kept for allowing an unobstructed operation, as shown in Figure 4.1. However, torque and speed fluctuations from a prime-mover can result in the teeth to vibrate within the backlash, which results in the rattling noise.

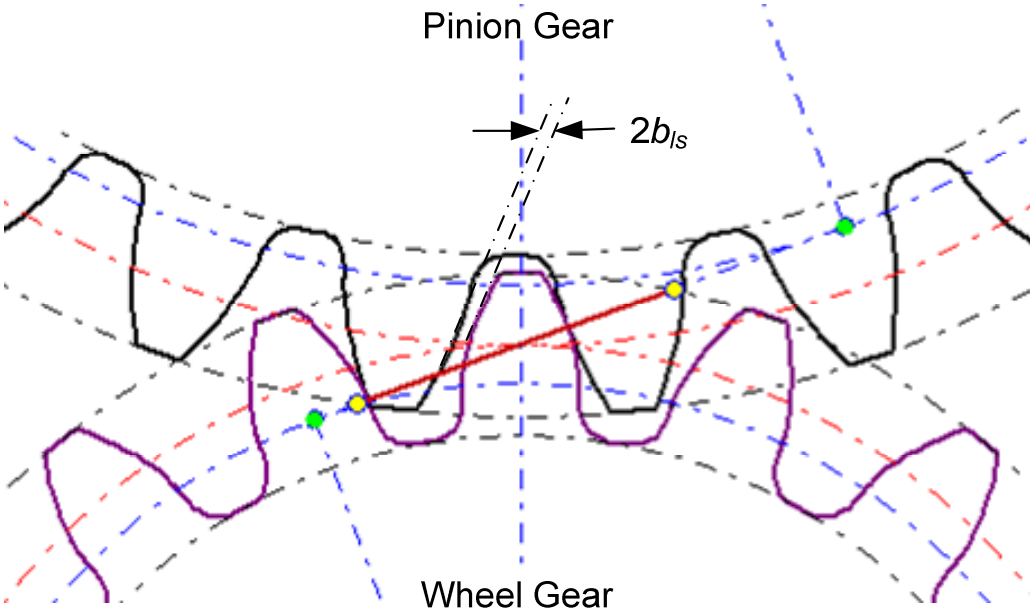

Figure 4.1 Gear teeth meshing for a gear pair

Bearing frictional torque

Palmgren model was developed based on a laboratory testing of different types and sizes of bearings to describe the bearing frictional torque with respect to rolling, sliding and lubricant loss effects as [134]

$$T_{bf} = T_0 + T_1 \tag{4.1}$$

where, T_0 is a load independent component determined by the lubricant properties and a function of angular velocity, while T_1 is a load dependent component determined by the radial and axial load which can be assumed to be a constant for a given load. The dependence of these frictional components on bearing type, dimensions, load, rotational speed, and lubricant properties is described in [134-136].

Lubricant churning losses

Grease lubrication is commonly used in medium-sized gearboxes, wherein all the gears are either partially or completely submerged in the lubricant. This results in a power loss component due to lubricant churning. The churning loss is a complex process for which a dynamic model was developed in [137, 138], where the churning torque can be expressed as a function of the grease viscosity and immersion of the gears in the lubricant, which is dependent on dimensions of gears and the gearbox housing. The churning torque function is given as

$$T_{ch} = 0.5\rho_{\text{lub}}\omega^2 r_c^3 S_m T_m \tag{4.2}$$

where ρ_{lub} is the density of the lubricant oil, S_m is the immersion area of the gear in the lubricant, and T_m is the dimensionless drag torque. At low speeds, T_m can be obtained as

$$T_m = 1.36\left(h/d_c\right)^{0.45}\left(V_0/d_c^{\,3}\right)^{0.1}\mathrm{Re}^{-0.21}\,\mathrm{Fr}^{-0.6} \tag{4.3}$$

where h is the immersed depth of the gear in the lubricant, d_c is the pitch diameter, V_0 is the volume of the lubricant oil, the Reynolds number $\mathrm{Re} = \omega r_p^2 / v_{\mathrm{lub}}$, Froude number $\mathrm{Fr} = \omega^2 r_p / v_{\mathrm{lub}}$ and v_{lub} is the dynamic viscosity of the lubricant oil.

4.2.2 Transmission model under idling conditions

A typical five-speed manual transmission [139] is shown in Figure 4.2. In this configuration, the output gears are usually rotating freely. To obtain a given gear shift configuration which corresponds to a given speed ratio, one of the three synchronizers (shown in blue color) is used to lock different gears with the output shaft. However, the 4^{th} gear speed is obtained by directly coupling the input shaft with the output shaft using the first synchronizer from the left. Under idling condition, all gears on the output shaft are in a free flight condition wherein the only resistance to their motion is provided by a low drag torque that is due to the bearing friction and lubricant churning.

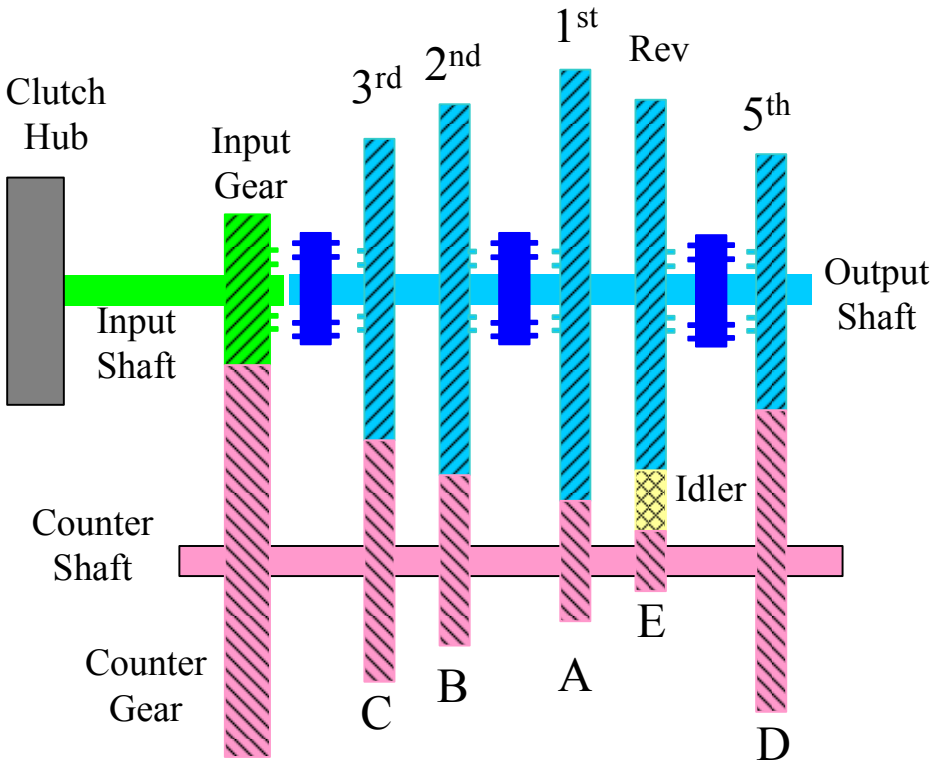

Figure 4.2 A typical five-speed manual transmission

To set up the dynamic model of the meshing gears, a two-DOF model consisting of the equivalent pinion gear and the corresponding wheel gear as shown in Figure 4.3 is formulated. Taking the example of the 3rd gear pair, the inertias on the input and counter shafts, including gears A, B, D, E, counter gear, input gears and clutch hub, are reflected onto the pinion gear C to obtain the equivalent pinion gear inertia I_p. The governing equations of the two-DOF model are obtained and can be written as

$$I_p\ddot{\theta}_p = T_p - r_{bp}f_N - r_{bp}c_g\dot{\xi} - T_{bfp} - T_{chp} \tag{4.4a}$$

$$I_w\ddot{\theta}_w = r_{bw}f_N + r_{bw}c_g\dot{\xi} - T_{bfw} - T_{chw} \tag{4.4b}$$

where T_p is the driving torque applied on pinion gear, I_w is the wheel gear inertia, r_{bp} and r_{bw} are the base radii of pinion and wheel gears, T_{bfp} and T_{bfw} are

the bearing frictional torque of pinion and wheel gears, T_{chp} and T_{chw} are the churning torque of pinion and wheel gears, θ_p and θ_w are the angular displacement of the pinion and wheel gears, k_g is the gear meshing stiffness, c_g is the damping coefficient of the gear pair, and f_N is the contact force acting on the gear teeth surface. f_N can be expressed as

$$f_N = k_g \begin{cases} \xi - b_{ls} & \xi > b_{ls} \\ 0 & |\xi| \le b_{ls} \\ \xi + b_{ls} & \xi < -b_{ls} \end{cases} \tag{4.5}$$

where $\xi = r_{bp}\theta_p - r_{bw}\theta_w$ is the dynamic transmission error.

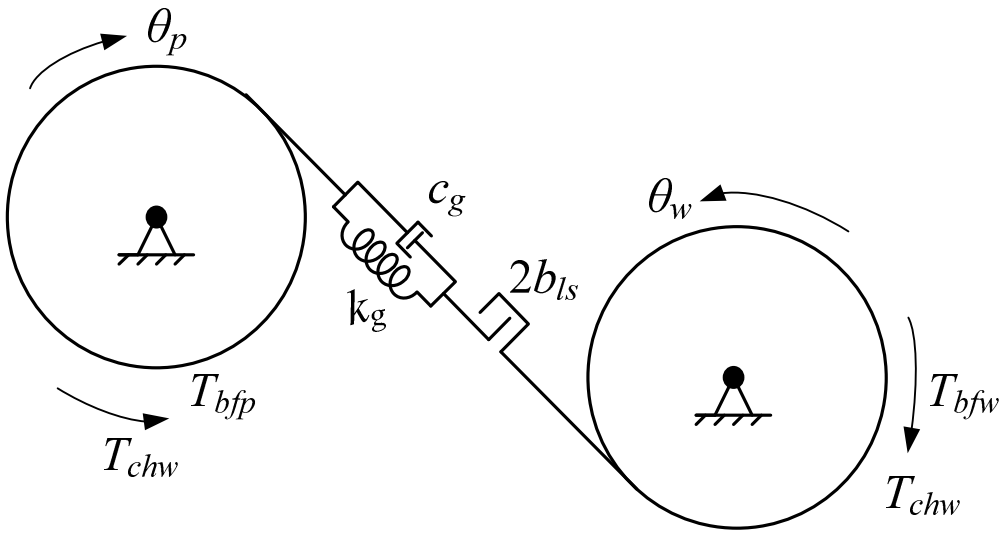

Figure 4.3 A two-DOF model for the transmission

4.3 Analytical Evaluation of the Gear Tooth Impact

4.3.1 Modeling of the gear tooth impact

The unique working principle in an internal combustion engine (ICE) and the unbalance from the internal rotational component can excite speed fluctuations in a transmission system. For example, in a four stroke ICE, each cylinder needs to rotate two revolutions to finish one stroke. And the frequency of speed

fluctuations is proportional to the number of the cylinder. Therefore, in a *N*-cylinder four-stroke ICE, the input angular speed at the pinion gear as applied by the ICE can be described as [12]

$$\omega = \omega_m + \Delta\omega \cos\left(\frac{N}{2}\omega_m t\right) \tag{4.6}$$

where the pinion gear speed ω fluctuates at $N/2$ times of the input rotational frequency ω_m. As the gear impact is determined only by the speed fluctuation component, the mean gear speed can be ignored in the subsequent analysis and thus the input velocity at pinion gear is taken as:

$$\omega = \Delta\omega \cos\left(\frac{N}{2}\omega_m t\right) \tag{4.7}$$

This speed fluctuation can result in alternating teeth separation and impacts within the gearbox under idling conditions, as illustrated through the speed profiles of the pinion and wheel gears in Figure 4.4. The loss of gear contact occurs from point B to C and then from point E to F in Figure 4.4, during which the pinion gear's speed profile follows the solid line, while the wheel gear follows the dashed line. In other regions, the gears remain in contact. The area between the speed profiles of the two gears from point B to C or from point E to F is the distance travelled by gear teeth between the impacts and equals the backlash $2b_{ls}$.

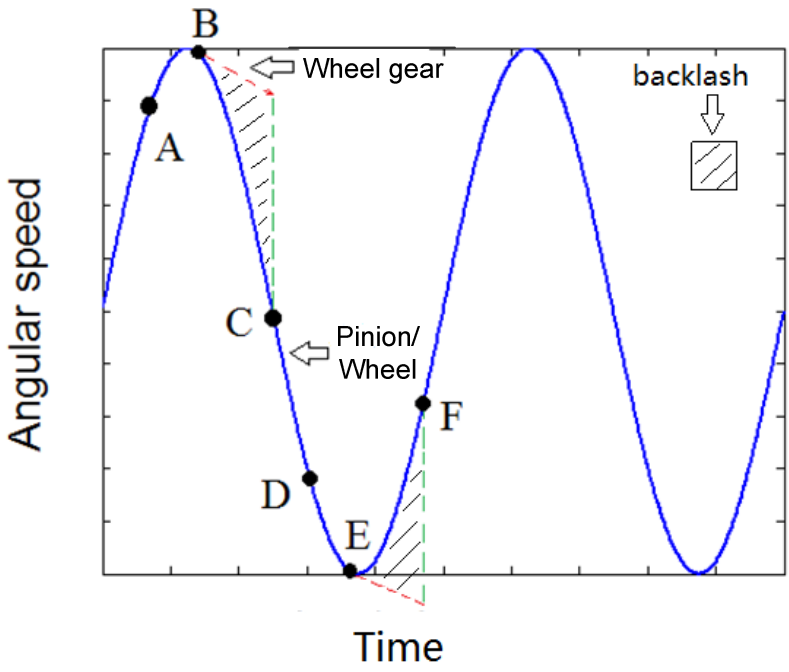

(a)

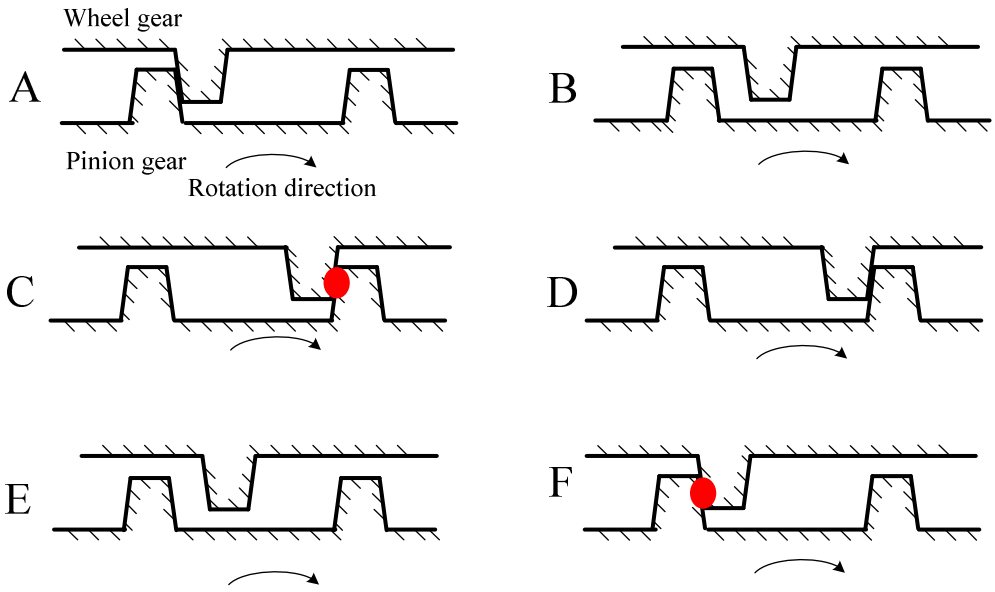

(b)

Figure 4.4 Gears crossing across backlash (a) gears' speed profiles, and (b) key configurations [116]

Gear rattle occurs if the tangential deceleration at the contact point for the pinion gear is greater than that for the wheel gear. Under idling condition, only

the drag torque due to bearing and lubricant acts on the wheel gear. Therefore, the deceleration threshold for the pinion above which gear rattle occurs is

$$\ddot{\theta}_{critical} = r_{bw} T_{drag} / \left(r_{bp} I_w \right) \tag{4.8}$$

where the drag torque $T_{drag} = T_{chw} + T_{bfw}$ consists of the bearing friction and the lubricant churning components. Thus, a decrease of the drag torque or an increase of the wheel gear inertia decreases the deceleration threshold limit, thereby increasing the likelihood of gear rattle.

Gear rattle noise, which is directly perceived by the end user, is correlated to the acceleration of the gear teeth. According to [116, 128, 129], the RMS value of the wheel gear acceleration is linearly correlated with the noise level when the gear rattle occurs. And this RMS value has been used to indicate the sound perception. The noise produced by the pure rotation of the gear bodies is negligible. Therefore, the rattle noise level is mainly determined by the period when gear impact occurs. Furthermore, although several consecutive impacts might occur before the gear teeth mesh together again, the first impact has the dominant energy as the rest ones can be dampened quickly [130, 131]. As a result, the rattling noise level is mainly determined by the RMS value of the wheel gear acceleration during the first impact period. This reasonable simplification enables the RMS value to be estimated analytically. Therefore, the influence of gearbox parameters' such as the meshing stiffness, damping factor, gear inertia and backlash, on the rattling noise level can be accessed by evaluating their effect on the RMS value of the wheel gear acceleration through investigation of the dynamic model of gearbox presented in Eqn. 4.4. Taking

example of a typical transmission presented in [139], the ratio of equivalent inertia of the pinion gear with respect to the largest gear on the output shaft is greater than six. Therefore, the output gear has little effect on the dynamic response of input shaft. Furthermore, the wheel gear dynamics under idling conditions can be represented by a single DOF model (similar to Ref. [12]) as shown in Figure 4.5, where the wheel gear can be modeled as a rigid body vibrating along the tangential direction insides the backlash. The boundary conditions for the motion equation for the wheel teeth vibration are time-varying due to the speed fluctuations from input at the pinion gear. Compared with the 2-DOF model, the motion equation of the 1-DOF model can be solved easily by analytical approach.

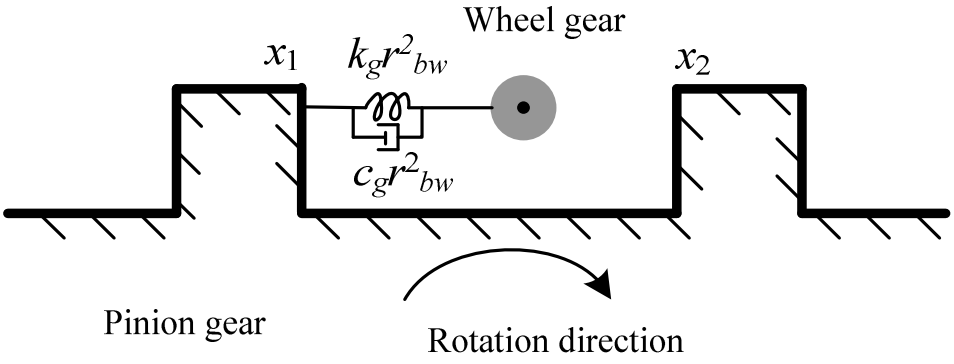

Figure 4.5 Single-DOF model for the gear impact

Considering with a six-cylinder four stroke ICE an impact on the front flank side of the teeth, the equation of motion for the wheel gear from the time instant at start of collision t_0 till the time instant for separation t_1 can be obtained by substituting Eqns. 4.5 and 4.7 into the Eqn. 4.4b as

$$I_w\ddot{x} + c_g r_{bw}^2 \dot{x} + k_g r_{bw}^2 x = -\left(T_{drag} r_{bw} + k_g r_{bw}^2 b_{ls}\right) + c_g r_{bp} r_{bw}^2 \Delta\omega \cos 3\omega_m t + \frac{k_g r_{bp} r_{bw}^2 \Delta\omega}{3\omega_m} \sin 3\omega_m t \quad (4.9)$$

where $x = r_{bw}\theta_w$ is the tangential displacement of the wheel gear. The initial conditions at $t = t_0^-$, when the gear pair are about to collide on the front flank (side x_1 in Figure 4.5) are

$$x_w\left(t_0^-\right) = -b_{ls} + \frac{r_{bw}\Delta\omega}{3\omega_m} \sin\left(3\omega_m t_0\right) \quad (4.10a)$$

$$\dot{x}_w\left(t_0^-\right) = v_0 = \Delta\omega \cos\left(3\omega_m t_0\right) \quad (4.10b)$$

where v_0 is the initial tangential speed of the pinion gear.

4.3.2 Analytical solution

In this section, the motion equation of the wheel gear is simplified and analytically solved. For a typical gear pair, the ratio k_g/c_g is greater than 1×10^4 while the idling speed of a medium sized engine ω_m is less than 200 rad/s. Compared to the third term on the right side of Eqn. 4.9, the second term has much lower amplitude and therefore can be neglected. Furthermore, the drag torque T_{drag} induced acceleration component is much lower than the tooth impact force induced acceleration during the impact period and can also be neglected. Therefore,

$$I_w\ddot{x} + c_g r_{bw}^2 \dot{x} + k_g r_{bw}^2 x \approx -k_g r_{bw}^2 b_{ls} + \frac{k_g r_{bp} r_{bw}^2 \Delta\omega}{3\omega_m} \sin 3\omega_m t \quad (4.11)$$

The solution of Eqn. 4.11 can be expressed as a sum of three terms

$$x = x_h + x_{p1} + x_{p2} \quad (4.12)$$

where x_h is the homogeneous solution, x_{p1} is the particular solution corresponding to the constant term $-k_g r_{bw}^2 b_{ls}$, and x_{p2} is the particular solution

corresponding to the sinusoidal term $\frac{k_g r_{bp} r_{bw}^2 \Delta\omega}{3\omega_m} \sin 3\omega_m t$. These three solutions can be individually found as

$$x_h = e^{-\zeta\omega_n t}\left(A_1 \cos\omega_d t + B_1 \sin\omega_d t\right) \tag{4.13a}$$

$$x_{p1} = -r_{bw} b_{ls} \tag{4.13b}$$

$$x_{p2} = \frac{r_{bp}\Delta\omega}{3\omega_m} \cdot \frac{k_g r_{bw}^2}{\sqrt{\left(k_g r_{bw}^2 - 9I_w\omega_m^2\right)^2 + \left(4c_g r_{bw}^2 \omega_m\right)^2}} \sin 3\omega_m t \tag{4.13c}$$

where the natural frequency $\omega_n = \sqrt{\frac{k_g r_{bw}^2}{I_w}}$, the damped natural frequency $\omega_d = \sqrt{1-\zeta^2}\,\omega_n$, and damping factor $\zeta = \frac{c_g r_{bw}}{2\sqrt{k_g I_w}}$. For a typical gear pair, $\omega_n >> 3\omega_m$ and $k_g >> 4\omega_m c_g$. Therefore, Eqn. 4.13c can be rewritten as

$$x_{p2} \approx \frac{r_{bp}\Delta\omega}{3\omega_m} \sin\left(3\omega_m t\right) \tag{4.14}$$

Using the initial condition shown in Eqn. 4.10, the coefficients A_1 and B_1 in x_h can be evaluated as

$$A_1 = -\frac{r_{bw} v_d \sin\omega_d t_0}{\omega_d} e^{\zeta\omega_n t_0} \tag{4.15a}$$

$$B_1 = \frac{r_{bw} v_d \cos\omega_d t_0}{\omega_d} e^{\zeta\omega_n t_0} \tag{4.15b}$$

where $v_d = v_0 - r_{bp}\Delta\omega\cos\left(3\omega_m t_0\right)$ is the tangential speed difference between the gears at time $t = t_0^-$ when the impact is about to occur. Thus, tangential displacement of the wheel gear (Eqn. 4.12) can be evaluated as

$$x = e^{-\zeta\omega_n\left(t-t_0\right)} \frac{v_d r_{bw} \sin\omega_d\left(t-t_0\right)}{\omega_d} - r_{bw} b_{ls} + \frac{r_{bp}\Delta\omega}{3\omega_m} \sin\left(3\omega_m t\right) \tag{4.16}$$

The wheel gear tangential acceleration can be obtained by twice differentiating the Eqn. 4.16 with respect to time

$$\ddot{x} \approx \frac{e^{-\zeta\omega_h(t-t_0)}}{I_w} v_d \sqrt{k_g I_w r_{bw}} \cdot \left[\left(1-2\zeta^2\right)\sin\omega_d\left(t-t_0\right)+2\zeta\cos\omega_d\left(t-t_0\right)\right] \quad (4.17)$$

It can be observed that the acceleration $\ddot{x}$ of gear teeth excited due to their impacts is determined mainly by the homogeneous solution. The particular solution x_{p1} is constant, and it disappears in Eqn. 4.17 during differentiation. Also, $\left|\ddot{x}_{p2}\right|$ is much lower than the homogeneous solution $\left|\ddot{x}_h\right|$. However, it must be noted that the pinion speed fluctuation $\Delta\omega$ also affects the homogenous component of wheel gear acceleration. A larger $\Delta\omega$ produce a higher speed difference v_d, which will increase the RMS value of acceleration as given by Eqn. 4.17. As is shown in previous literatures [116, 129], the rattling noise level is linearly correlated with the RMS value of the impact-induced wheel gear acceleration. Further, the first impact is the most dominant among the consecutive impacts that may occur on a gear tooth face. Taking the duration of the gear tooth first impact to be half of the damped oscillation period for the gear teeth $t_1 - t_0 = \pi/\omega_d$, the RMS value can be obtained as

$$\mathrm{RMS}\left(\ddot{x}\right) = \sqrt{\frac{1}{t_1 - t_0}\int_{t_0}^{t_1} \ddot{x}^2 dt} \quad (4.18)$$

$$\approx v_d \sqrt{\frac{k_g\left(1-e^{-2\pi\zeta}\right)r_{bw}}{4\pi I_w \zeta}\left(1+4\zeta^4\right)}$$

Furthermore, the shaded region in Figure 4.4(a) between the wheel gear speed profile and the pinion gear speed profile can be treated as a triangle whose area equals to the backlash amount $2b_{ls}$. Therefore, the speed difference v_d and

backlash $2b_{ls}$ can be related as $v_d \approx k_d\sqrt{2b_{ls}}$ where k_d is a constant coefficient for a given speed fluctuation amplitude. Thus,

$$\mathrm{RMS}(\ddot{x}) = k_d\sqrt{\frac{2k_g\left(1-e^{-2\pi\zeta}\right)r_{bw}}{4\pi I_w\zeta}\left(1+4\zeta^4\right)b_{ls}} \tag{4.19}$$

Based on Eqn. 4.19, it can be seen that RMS($\ddot{x}$) increases if the meshing stiffness k_g or the backlash $2b_{ls}$ increases. However, it will decrease if the inertia of the wheel gear I_w increases. If the damping factor ζ increases, the damping related term $\sqrt{\left(1-e^{-2\pi\zeta}\right)\left(1+4\zeta^4\right)/\zeta}$ decreases in the typical range of damping factor [140], $0.01 \le \zeta \le 0.10$, which results in a decrease of RMS($\ddot{x}$) value.

4.4 Results and Discussion

The gear rattle occurring in a typical transmission is investigated in this section through a transmission models as shown in Figure 4.6. A flywheel is connected to the pinion gear through a clutch. The pinion gear meshes with the wheel gear as a meshing pair. The equivalent inertia of the pinion gear is much larger than that of the wheel gear because the equivalent pinion gear inertia should considers the gears and rotor inertias at the input side as well as the counter shafts' inertia. In this study, this equivalent inertia is set to be six times of the wheel gear, which is typical in automobile transmission design [61, 62, 139]. The corresponding model parameters are given in Table 4.1. The frictional characteristics associated with lubricant churning are evaluated assuming that 3/10th of the gears are immersed in the lubricant (70°C).

Table 4.1 Parameters of the transmission

Parameters	Value
Number of teeth (pinion/wheel gears)	25/25
Module m (mm)	4
Pressure angle α (°)	20
Equivalent inertia of the pinion gear I_p (kg.m^2)	7.0×10^{-3}
Inertia of the wheel gear I_w (kg.m^2)	1.16×10^{-3}
Gear meshing stiffness k_g (N/(m.rad))	2.4×10^{8}
Damping factor ζ of gear meshing	0.06
Half of backlash b_{ls} (μm)	50
Inertia of flywheel (kg.m^2)	3×10^{-2}
Stiffness of clutch (N.m/rad)	1×10^{-3}

4.4.1 Modeling in SIMPACK

A typical transmission is modeled in SIMPACK (shown in Figure 4.6) where a spur gear pair is connected to a large inertia to simulate the flywheel through an equivalent torsional spring-damper system to simulate the clutch. The elements from SIMPACK library used to model the system are shown in Table 4.2.

Table 4.2 Model components represented in SIMPACK

Component	SIMPACK element
Gears	Primitive 25: Gear wheel
Flywheel	Primitive 2: Cylinder
Driving speed of the flywheel	Joint: Single axis 40 $u(t)$
Gear meshing stiffness and damping	Force element 225: Gear pair
Stiffness and damping of clutch	Force element 52: Cardan joint

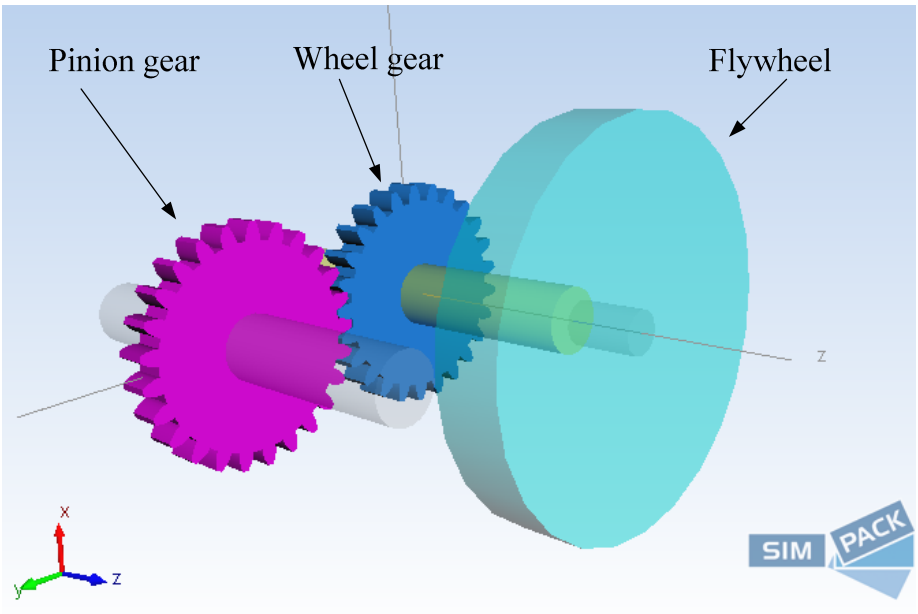

Figure 4.6 Dynamic model of the transmission

4.4.2 Result analysis

If the gear rattle occurs, it can manifest itself as either a single-sided or double-sided impact, which depends on the magnitude of the pinion gear deceleration. With the model described in Section 4.4.1, letting ω_m=83.78 rad/s (800RPM) and $\Delta\omega$ = 12.57 rad/s (120RPM) the double-sided impact occurs (as seen in the dynamic transmission error fluctuations shown in Figure 4.7) which is a typical gear rattle phenomenon [12]. Therefore, this case is analyzed to investigate the gear parameters effect on the rattle impact. From Figure 4.8(a), it can be seen that the bearing frictional torque and the lubricant churning torque components are comparable under idling conditions. Both of them have a low value and have similar contributions in determining the threshold of the rattle occurrence. The tooth impacts periodically excite impulse like peaks in the gear teeth contact force profile (Figure 4.8(b)), which is the root cause of the rattling noise.

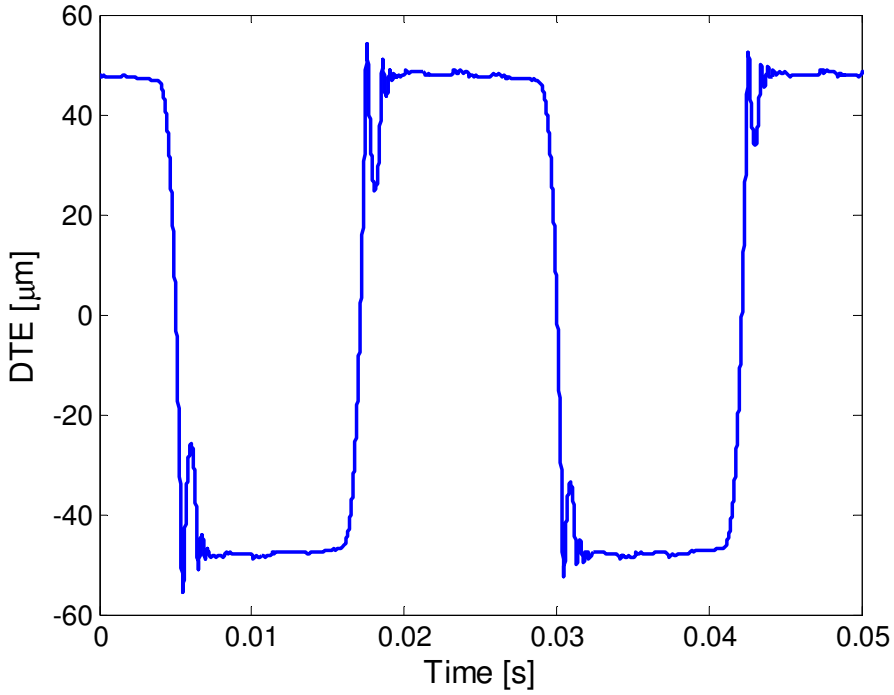

Figure 4.7 Dynamic transmission error under rattle

The gear rattle noise level indicator presented in Eqn. 4.19 is verified by varying the model parameters: wheel gear inertia, meshing stiffness, backlash, and meshing damping factor in SIMPACK simulations, one at a time. The wheel gear inertia, meshing stiffness and backlash are varied to 1/3, 2/3, 1, 4/3, and 5/3 times their reference value presented in Table 4.1. The damping factor is varied from 0.02 to 0.10 using a step size of 0.02. The obtained RMS acceleration of the wheel gear is then normalized with respect to the RMS value obtained using the reference values given in Table 4.1. The result from the analytical expression and the SIMPACK dynamic model are compared in Figure 4.9. It is seen that the proposed analytical expression predicts the increase of the backlash amount and the gear meshing stiffness increases the RMS acceleration of wheel, which matches closely with the results from SIMPACK simulation (Figure 4.9(a) and (b)). A larger backlash will result in a

larger gear speed difference at the time of impact, while a stiffer gear tooth will also increase the contact force magnitude at the impact. Therefore, both these factors increase the RMS acceleration as observed in the figure. A larger RMS acceleration in turn implies that the noise due to gear rattle will be higher. The backlash effect was verified in [12] through experiment, where the rattle noise level was measured for an idler gear first as shown in Figure 4.10. Then an elastic thrust collar was fitted onto the same idler gear surface to reduce the backlash. The measurement showed that the rattling noise level can be reduced with the reduced backlash. The analytical method also predicts that an increase in inertia of the wheel gear or the damping factor reduces the RMS acceleration of the wheel gear, which matches closely with the results obtained from the SIMPACK simulations (Figure 4.9(c) and (d)). The reduced RMS acceleration in turn indicates a lower noise level due to gear rattle. The wheel gear inertia effect was verified through the experiment in [116] where the RMS values were measured with three gears using different inertias as shown in Figure 4.11. The results showed that high inertia resulted in a low RMS acceleration value, as well as the rattle noise. Thus, it is shown that the proposed analytical method can be used to evaluate the gear parameters effect on the rattling noise level, and provide a gear rattle measure (Eqn. 4.19) to aid in the gearbox design optimization.

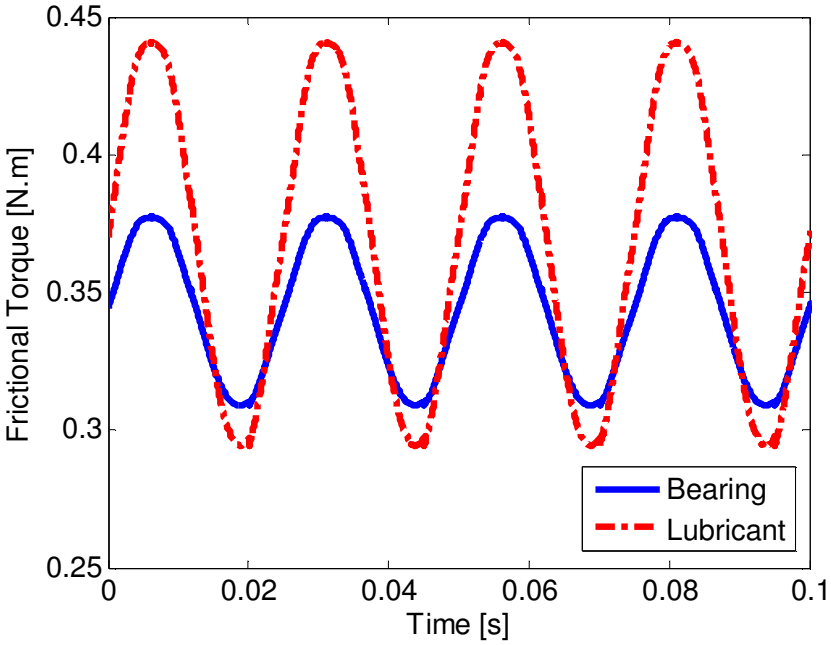

(a)

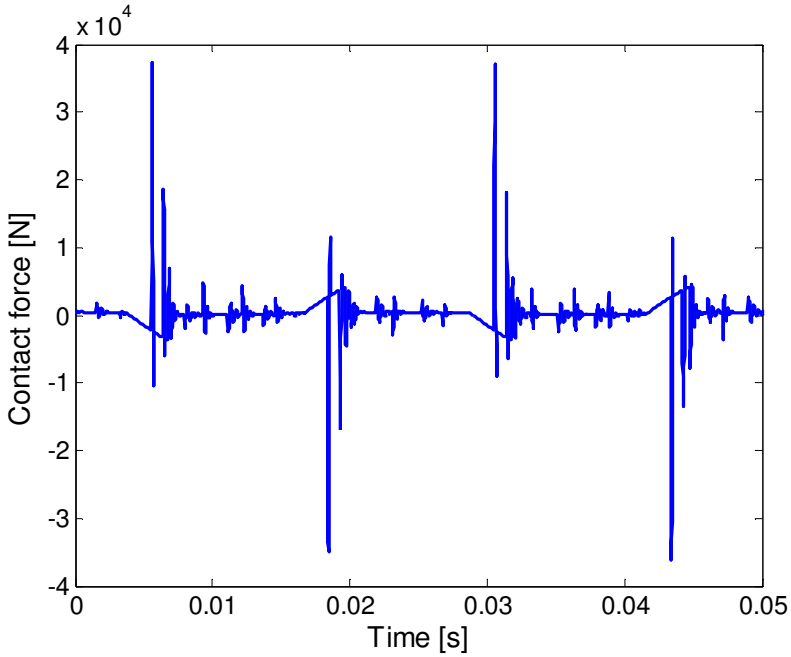

(b)

Figure 4.8 (a) Frictional torques and (b) gear teeth contact force at the wheel gear

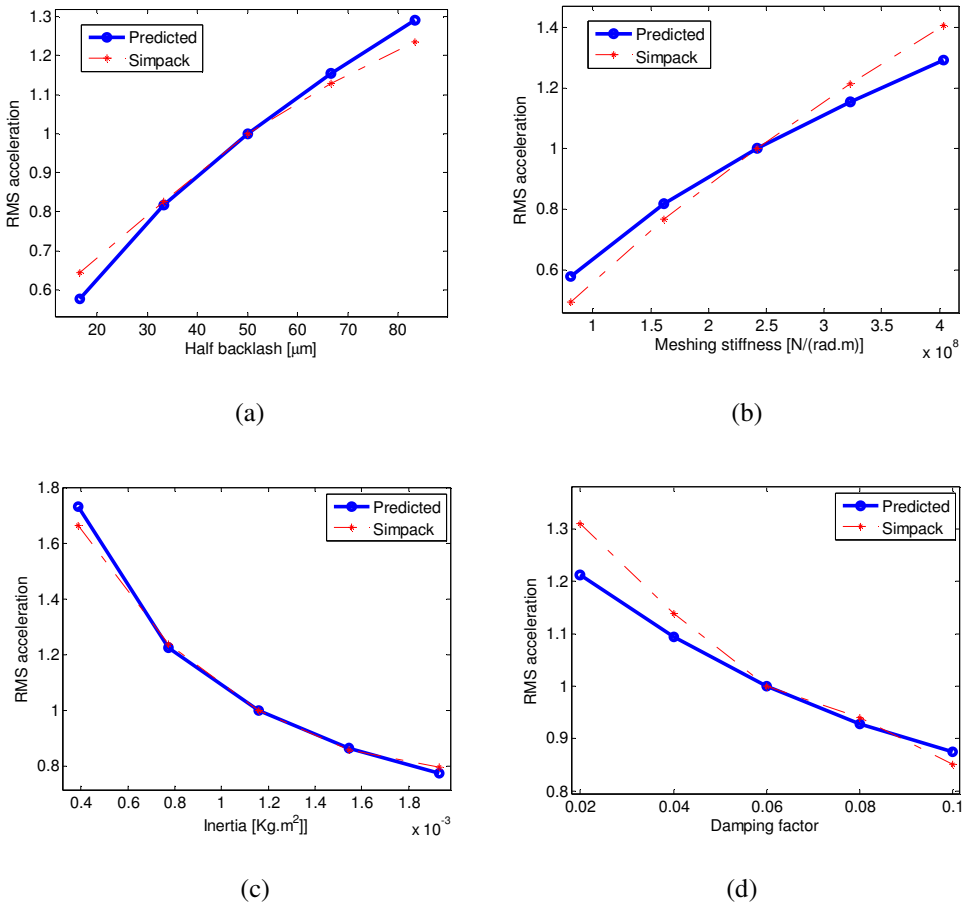

Figure 4.9 Normalized RMS of the wheel gear acceleration versus variation in gear parameters (a) backlash, (b) meshing stiffness, (c) inertia of the wheel gear, and (d) damping factor

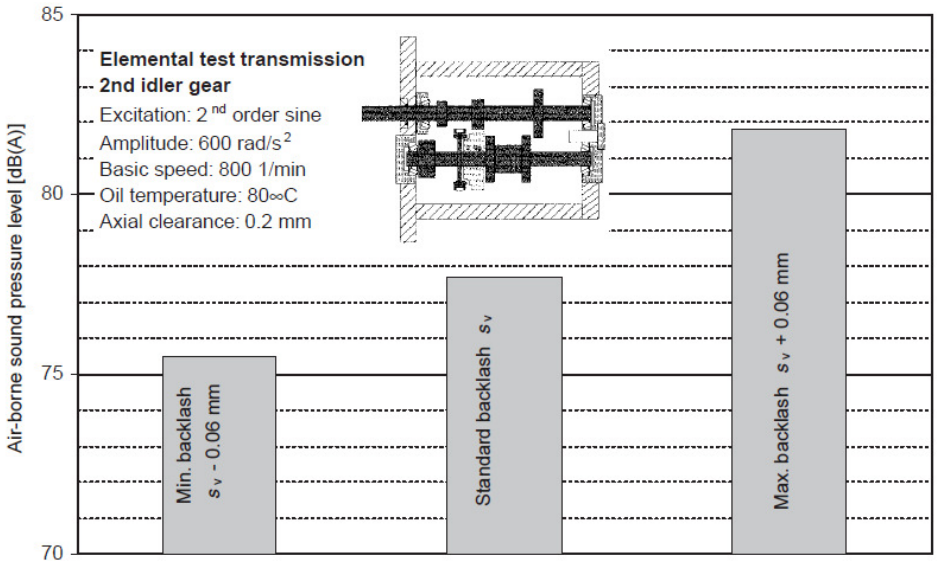

Figure 4.10 Effect of backlash on the rattling noise level at an angular acceleration amplitude of 600 rad/s^2, based on results for the second gear idler gear [12]

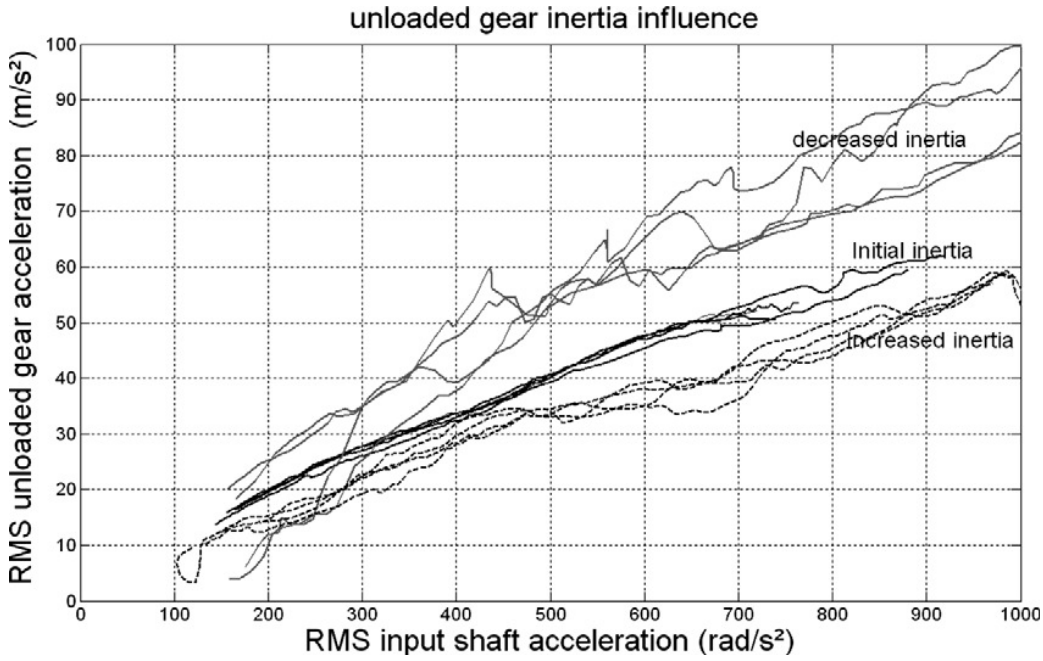

Figure 4.11 Influence of the unloaded gear inertia for an excitation at 45 Hz [116]

4.5 Conclusion

An analytical solution determining the RMS value of the rattle impact induced acceleration component for wheel gears based on a dynamic model of a typical manual transmission is presented in this chapter. Since RMS acceleration value is proportional to the rattling noise level [116, 129], the proposed analytical evaluation method is capable of investigating the gear parameters' effect on the rattle noise level. The evaluated RMS acceleration value for the wheel gear in the typical transmission gearbox is then used to investigate the effect of backlash, meshing stiffness, inertia and meshing damping factor on the rattle noise levels. To verify the proposed analytical evaluation method, an MBS dynamic model for the typical transmission is developed in SIMPACK. The comparison of analytical and dynamics simulation analysis shows that the proposed analytical expression for RMS acceleration value can effectively

predict the influence of gear parameters. Moreover the obtained analytical and simulation results also agrees with the previous experimental result in [12, 116]. Thus, the proposed evaluation method provides a simple guideline that can optimize the gearbox parameters to reduce the gear rattle noise level.

Chapter 5 Detecting Planetary Gearbox Fault by Motor Current Signature Analysis

The electro-mechanical interactions in the electro-mechanical power-trains (EMPTs) enable to investigate the torsional vibration through the electrical signature from the electric machines. As a result, vibration signature excited by the mechanical faults can be monitored by the stator current from the electric machines, referred to as Motor Current Signal Analysis (MCSA). MCSA provides an alternative nonintrusive fault detection approach. However, the harmonics resulting from the structural properties of the electric machines and the inherent system imperfections make it challenging to detect the incipient fault in the planetary gearboxes, which will be explored in this chapter. In Section 5.1, the overall configuration as well as the individual components in an EMPT testbed are introduced, which can be used to verify the built models as well as the proposed condition health monitoring (CHM) methods. In Section 5.2, a CHM method based on the resonance residual technique is proposed and its performance over the existing methods is shown through both the simulation and the experiments.

5.1 An Electro-Mechanical Power-Train Testbed

5.1.1 Overall configuration

To verify the models developed for the EMPTs and the proposed CHM method, a configurable EMPT experimental testbed has already been built in Mechatronics Lab, Nanyang Technological University. This testbed consists of

two identical PMSMs (one as a driving motor, the other as a load generator), two identical planetary gearboxes where each one has a back-to-back configuration, a control panel, a load bank, a PC, a dSPACE 1104 DAQ & control card, and a few sensors as in Figure 5.1. Both the PMSMs and the gearboxes are installed on the slide ways. Together with the torque transducer installed on a supporting beam, four different configurations can be achieved in the EMPT as in Figure 5.2. This design helps to investigate a complex EMPT step by step.

The driving motor is controlled by a variable frequency inverter, whose speed command is prescribed through dSPACE 1104 through a D/A output port. The load generator provides the load for the overall EMPT and the electricity generated is dissipated by a load bank with variable steps. The dynamics of the EMPT can be accessed by several different kinds of sensors including the LEM current and voltage sensors, torque transducer, shaft encoder, as well as the accelerometer. Finally, the experiment data is collected by dSPACE 1104 A/D input ports.

5.1.2 Control panel

A control panel not only accommodates several electrical components but also isolates the high frequency electromagnetic noise caused by the inverter from the rest of the system. And the power cable should also be well shielded to remove the electromagnetic interference on the sensor signal. Otherwise, the acquired data from the sensors may contain significant interference noise. Inside the control panel, there is a variable frequency inverter, a few circuit breakers,

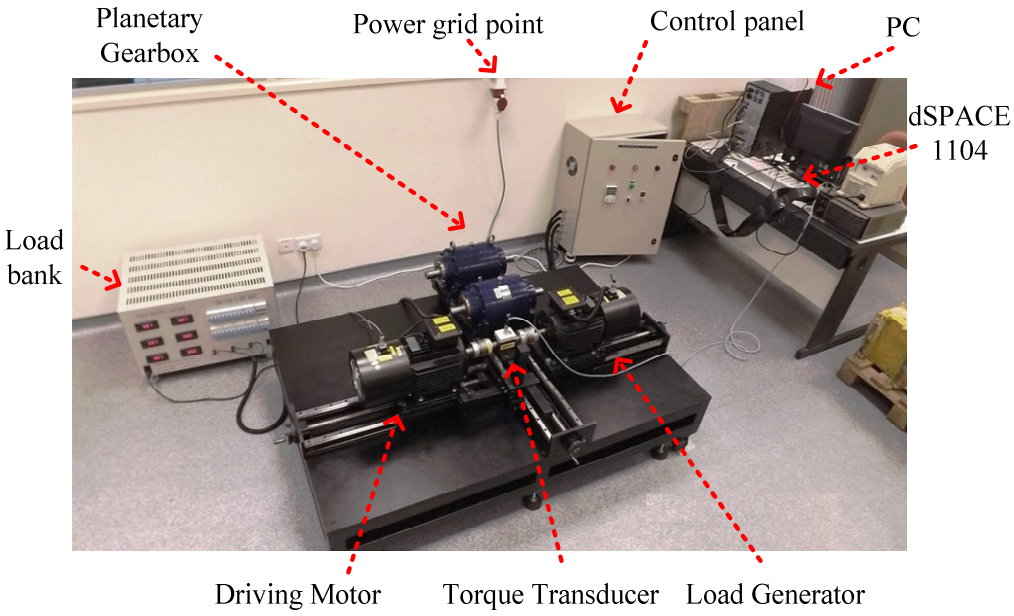

Figure 5.1 Electro-mechanical power-train testbed

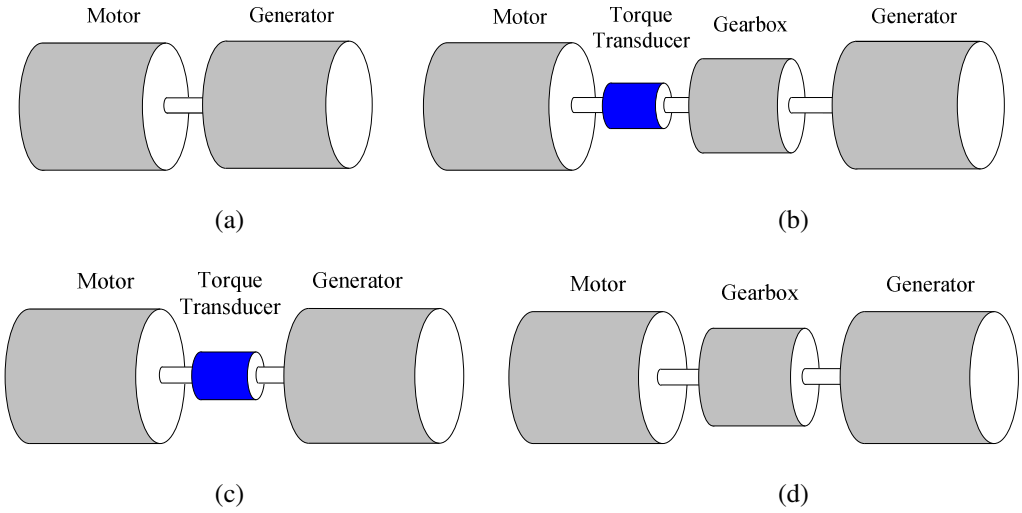

Figure 5.2 Four configurations of the power-train testbed

two PCBs integrated with the current and voltage sensors, and a DC power to supply the sensors as in Figure 5.3. The three phase terminal voltage and the line current of each PMSM can be measured by the sensors integrated on the PCBs. On the left wall of the control panel, there are four power cables

connecting different EMPT components together. On the right wall, there are a few BNC connectors to be as the signal interfaces.

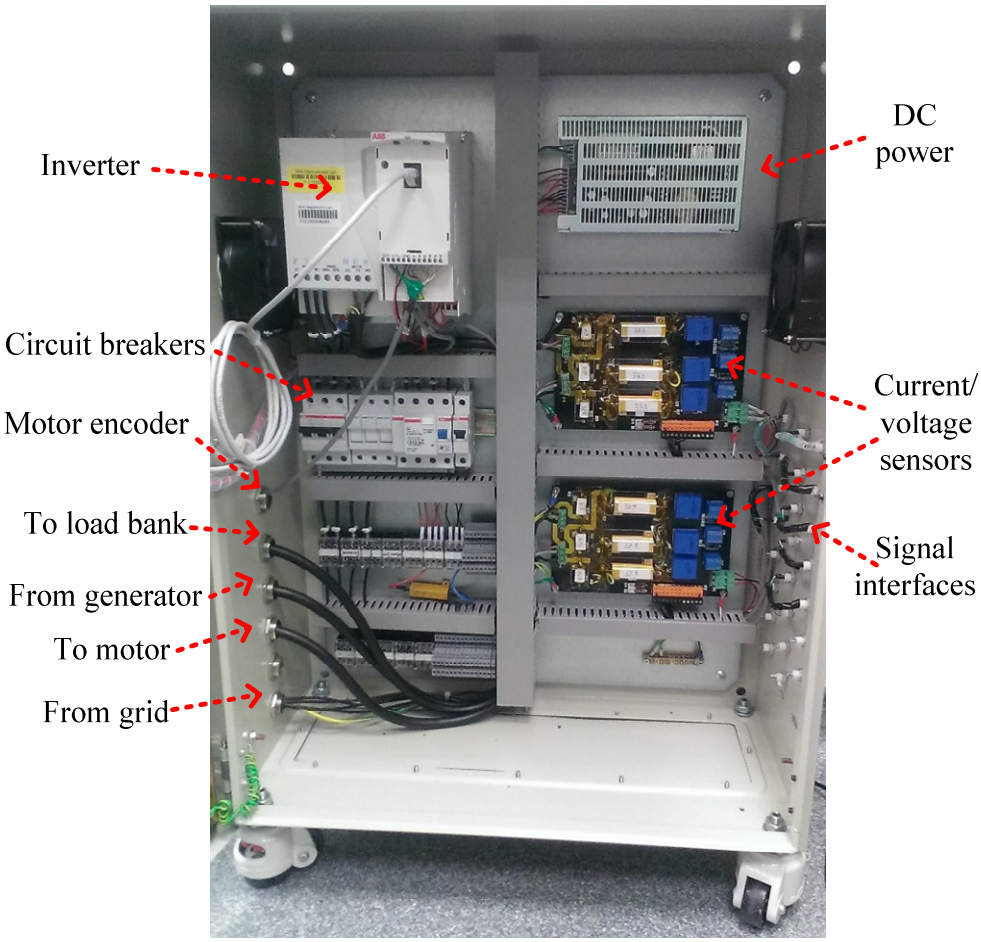

Figure 5.3 Control panel for the EMPT testbed

5.1.3 Sensor integration

In the Hall Effect current and voltage sensors, a primary coil and a secondary coil are coupled together. In the current sensor (LEM HX-10P), the line current directly flows through the primary coil. In the voltage sensor (LEM LV 25-P), the primary coil is connected between two phase terminals and a resistor R_1 is insert to allow only a small fractional current flow through the primary coil. In both sensors, a current proportional to the measured current/ voltage will be

excited in the secondary coil. A measuring resistor R_M / R_L is put into the secondary coil to convert the output current value into voltage value for easy measurement as in Figure 5.4. In order to calculate the suitable resistances R_1, R_M and R_L, the maximum value of the measured signal and the measuring range of the data acquisition system should be taken into consideration.

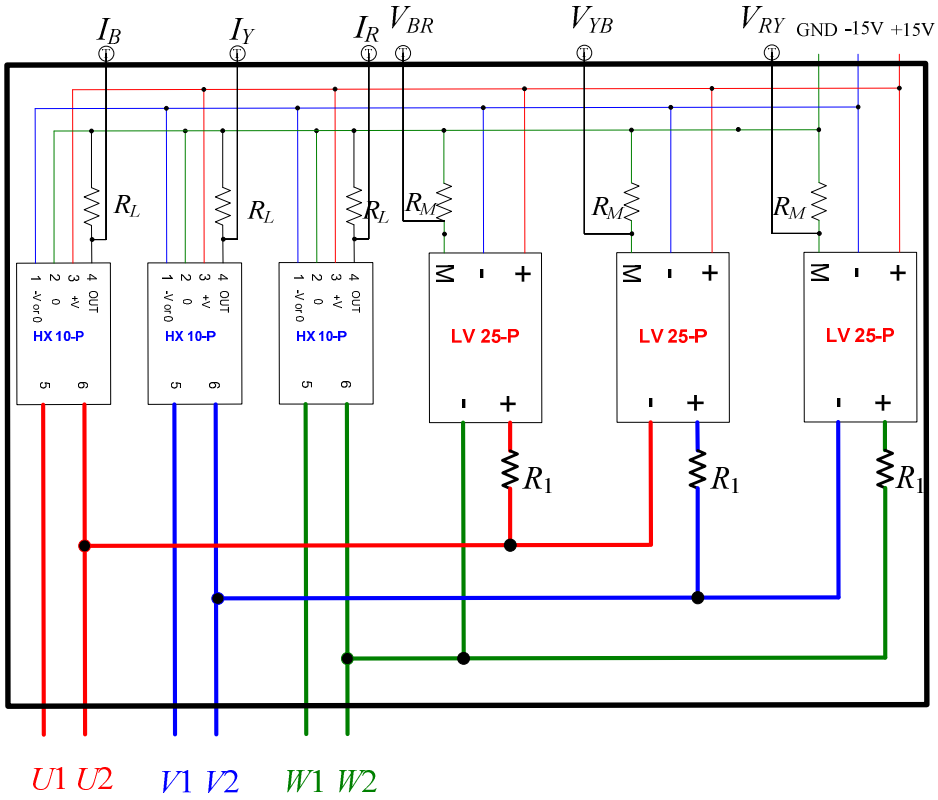

Figure 5.4 Wiring diagram of the current and voltage sensors for three phase measurement

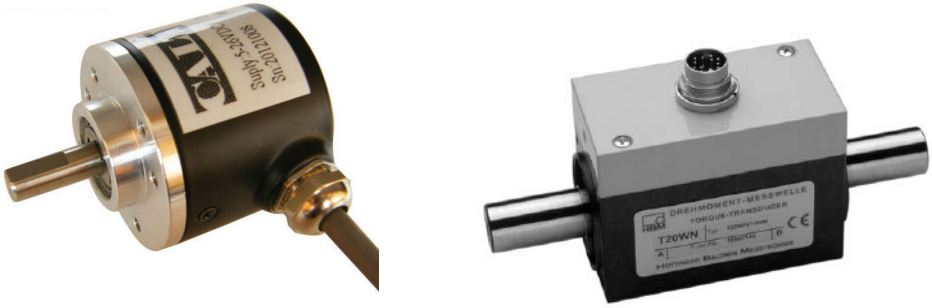

(a) Shaft encoder (b) Torque transducer

Figure 5.5 Speed and torque sensors

A solid shaft incremental encoder, with 5000 pulse per revolution (PPR) and the differential RS422 output circuit, is connected to the PMSM shaft to measure its rotational speed as in Figure 5.5. The measuring range of the shaft torque transducer is ±50N.m, where there is an additional shaft encoder with line driver output (TTL) and 360 PPR.

5.1.4 Parameters of the PMSMs

A three phase permanent magnet synchronous machine (PMSM) is used in this testbed with parameters shown in Table 5.1. It can work as either a driving motor or a load generator.

Table 5.1 Parameters of the PMSM

Parameters	*Value*
Nominal power (kW)	4
Nominal voltage (V)	380
Nominal speed (RPM)	1500
Number of poles	4
Stator winding resistance r_s (Ω)	1.28
Stator winding inductance L_q (mH)	160.4
Stator winding inductance L_d (mH)	39
Permanent magnet flux linkage λ'_f (A·H)	0.66
Inertia of rotor J_M (kg.m^2)	0.013

5.1.5 Load bank

In the testbed, an 8.6 kW three phase load bank with six different load steps is used whose wiring diagram is shown in Figure 5.6. If the applied terminal voltage per phase is 220V, the power consumed by these resistors will be 0.1, 0.2, 0.5, 1, 2, and 3kW respectively.

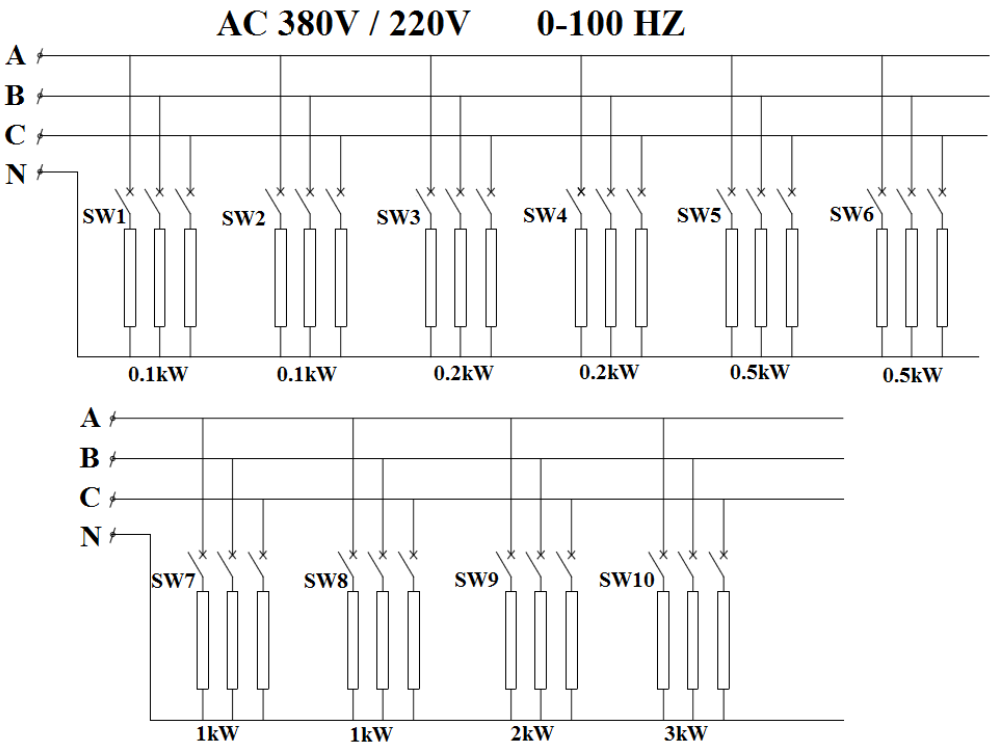

Figure 5.6 Wiring diagram of the load bank

5.1.6 Planetary gearbox and gear tooth fault creation

Each planetary gearbox in the testbed consists of two identical planetary gear sets connected in a back-to-back configuration such that the overall speed ratio is 1/4×4 =1.0, where 4 is the speed ratio for each gear set. The sun gear of one gear set is connected to the driving motor, while the sun gear of the other gear set is connected to the load generator. The carriers of the planetary gear set are connected together through a steel spline, and the annulus gears are fixed to the housing. In each planetary gear set, there are four equally spaced planets. The parameters for the gear set are shown in Table 5.2.

The frequent occurred faults in the planetary gearbox are the spalling fault and crack fault in the gear teeth. To investigate the dynamics under gear tooth fault and verify the proposed CHM methods, an artificial gear tooth crack is

introduced on one of the annulus gear tooth by removing 1/3rd of the tooth as in Figure 5.7.

Table 5.2 Parameters of the planetary gear set

Parameter	*Sun*	*Planet*	*Annulus*	*Carrier*
Number of tooth	28	28	84	-
Number of planet	-	4	-	-
Pressure angle (°)	22.5			-
Radius (mm)	51.74	51.74	155.2	56
Module (mm)	2			-
Tooth face width (mm)	30			-
Gear meshing stiffness [N/(rad.m)]	k_{min} = 1.4×10^8, and k_{max} = 2×10^8			-
Mass (kg)	0.576	0.576	-	5.4
Inertia (kg.m^2)	2.25×10^{-4}	2.25×10^{-4}	-	1.32×10^{-2}

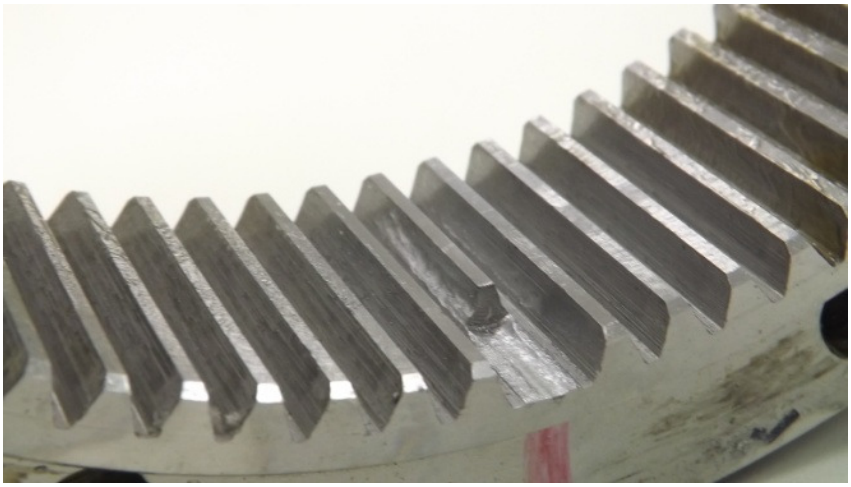

Figure 5.7 The simulated tooth crack on the annulus gear

5.2 Resonance Residual Technique

5.2.1 Motor current signature analysis

An electro-mechanical power-train consisting of electrical machines connected to a planetary gearbox can be found in several heavy-duty applications such as wind turbines, maritime vessels, helicopters and automobiles [141, 142]. They

allow a larger transmitted torque to weight ratio, easier control, higher reliability and efficiency, and reduced maintenance costs. However, a failure in the planetary gearbox can cause catastrophic accidents, extended downtimes and require expensive maintenance. Therefore, early detection of such failures can significantly reduce the associated capital losses. The conventional fault detection approaches for the gearboxes are usually based on the vibration and acoustic emission signatures [87, 89-91, 143]. However, practical implementation of such approaches can face several limitations, including (a) vibration and acoustic signals contain a significant noise resulting from external perturbations, (b) these measurements are affected by the sensor placement and the optimal sensor location is not always accessible, and (c) measurement is sensitive to the operating environment [51]. Furthermore, the vibration spectra of a planetary gearbox has complex characteristics, which are attributed to: (1) the angle-varying gear meshing stiffness from the planet-sun and planet-annulus gear meshes, and (2) the modulation effects introduced from the planet motion with respect to the fixed sensor mounted on the gearbox housing [122]. As a result of this modulation effect, the sidebands in the vibration spectra of a planetary gearbox are often non-symmetric and some of the expected frequency components may be missing.

Motor current signal analysis (MCSA), utilizing the stator current measurement from the electrical machines, provides an alternative non-intrusive approach to detect mechanical faults. The basis of MCSA is the reflection of mechanical torsional vibration on the stator current [19]. Mechanical faults such as rotor eccentricity, shaft misalignments, and bearing faults have been successfully

detected through MCSA [103-105] using the sidebands introduced in the current measurement spectra. Compared to the vibration signature analysis, utilizing MCSA for planetary gearbox fault detection can bring an additional benefit, where the analysis and interpretation of the results can be simplified by removing the modulation effect due to planet motion with respect to stationary sensor in the measured signal spectra. Faults in the fixed-axis gearboxes containing spur, helical, or worm gears have been detected using MCSA by monitoring the sidebands located at $f_e \pm m \bullet f_{GM} \pm n \bullet f_{GF}$ [51, 144-149]. The lowest fault indicating frequency components $f_e \pm n \bullet f_{GF}$ (by setting $m = 0$) were used as an indicator to detect the gear tooth fault in [144-147, 150]. The sidebands around the gear meshing frequency and its harmonics $f_e \pm m \bullet f_{GM} \pm n \bullet f_{GF}$ ($m \neq 0$) were proposed as an alternative indicator in [51, 144, 149]. However, most of the sidebands due to an incipient gear tooth fault have rather low amplitude. Therefore, they are often hidden by the harmonics resulting from the motor structure and noise. Thus, it is necessary to explore the location of the sidebands with high amplitudes that can provide rich fault information. However, such investigation for MCSA applications to detect faults in the planetary gearboxes is still lacking. The sideband amplitude at a given frequency is determined by the structural properties of the power-train. Vibration spectrum in the vicinity of the structural natural frequencies has been used to detect the spur gearbox and rolling bearing faults, where the fault induced sidebands show a higher amplitude around the structural frequencies of the power-trains [92, 151, 152]. Inspired by these approaches, this paper presents the resonance residual

technique that extracts the fault signature of a planetary gearbox using the measured stator current which often includes a high level of background noise.

The fault detection scheme presented in this section uses identified structural natural frequencies for the first time to detect gear tooth faults based on MCSA. Both simulations and experimental verification are presented to show the applicability of this proposed approach applied to an EMPT comprising of a driving motor (a Permanent Magnet Synchronous Machine, PMSM) connected to a load generator (another PMSM) through a planetary gearbox with back-to-back configuration (Figure 5.8). A multi-degree-of-freedom (DOF) lumped model for this power-train is developed and is numerically integrated using Newmark's method to investigate its dynamic response. It was shown in [149] that a gear tooth failure, such as a cracked tooth, spalled tooth or broken tooth, always results in a local reduction of the meshing stiffness when the faulty tooth passes through the gear meshing. Therefore, a seeded annulus gear tooth crack is modeled in this work through a local reduction in gear meshing stiffness function corresponding to each of the planet-annulus gear pair. The resonance residual technique is then applied onto the simulated or measured stator current. The resonance region around the evaluated structural frequencies of the power-train is utilized in this technique to extract spectral components with rich fault information of the gearbox. Furthermore, a fault indicator value is obtained to monitor the gearbox. The robustness of the proposed technique to detect gearbox faults under different operating conditions is demonstrated through experiments. Finally, the effectiveness of the proposed method over existing methods in fault detection from stator current is verified by experiments as well.

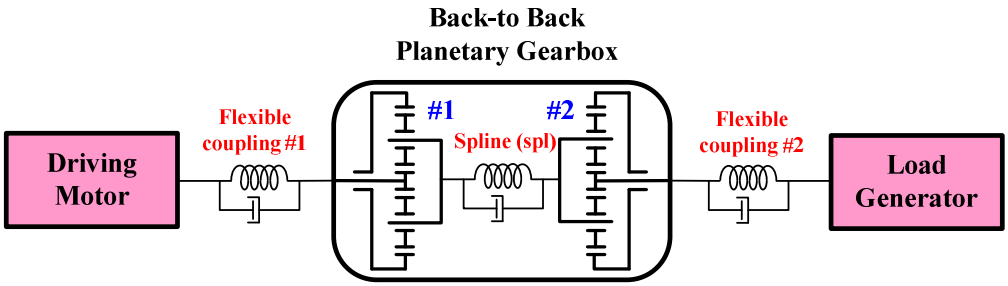

Figure 5.8 Schematic of the investigated electro-mechanical power-train

5.2.2 Dynamic model of an electro-mechanical power-train

5.2.2.1 State-Space representation of the PMSM

A three phase PMSM consists of (i) a fixed stator with three phase windings *a*, *b* and *c*, and (ii) a rotor with permanent magnet poles (Figure 2.11). When a three phase AC power supply is applied to the stator windings, a rotating magnetic field is produced which interacts with the permanent magnet poles on the rotor to push it forward. The dynamics of the PMSM can be described using Park's model as in [33, 35, 153], which can be rearranged in a state-space equation representation on the rotor reference frame (*d*-*q*) as

$$\underbrace{\begin{bmatrix}\dot{\lambda}_q\\ \dot{\lambda}_d\end{bmatrix}}_{\dot{\boldsymbol{\Lambda}}}=\underbrace{\begin{bmatrix}-R_s/L_q & -\omega_r\\ \omega_r & -R_s/L_d\end{bmatrix}}_{\mathbf{A}(\omega_r)}\underbrace{\begin{bmatrix}\lambda_q\\ \lambda_d\end{bmatrix}}_{\boldsymbol{\Lambda}}+\underbrace{\begin{bmatrix}v_q\\ v_d\end{bmatrix}+\begin{bmatrix}0\\ \lambda'_f R_s/L_d\end{bmatrix}}_{\mathbf{B}} \tag{5.1}$$

where $\boldsymbol{\Lambda}$ is the magnetic flux linkage vector. The matrix $\mathbf{A}(\omega_r)$ is a function of electrical rotor speed ω_r, $\mathbf{B}$ is the input vector comprising of the terminal voltages and a constant term from the permanent magnet flux linkage. The stator current vector $\mathbf{I}$ can be evaluated using $\boldsymbol{\Lambda}$ as

$$\underbrace{\begin{bmatrix}i_q\\ i_d\end{bmatrix}}_{\mathbf{I}}=\underbrace{\begin{bmatrix}1/L_q & 0\\ 0 & 1/L_d\end{bmatrix}}_{\mathbf{L}^{-1}}\underbrace{\begin{bmatrix}\lambda_q\\ \lambda_d\end{bmatrix}}_{\boldsymbol{\Lambda}}+\underbrace{\begin{bmatrix}0\\ -\lambda'_f/L_d\end{bmatrix}}_{\mathbf{G}} \tag{5.2}$$

where **L** is the inductance matrix, and **G** is a constant vector. Based on Eqn. 5.1 and 5.2, a model for the PMSM (load generator) can be built in SIMULINK as in Figure 5.10.

5.2.2.2 Lumped parameter model for planetary gearbox

With the multi-DOF lumped model developed for a planetary gear set in Section 3.4.2, each gear set in the planetary gearbox can be represented as

$$\mathbf{M}_j\ddot{\mathbf{Q}}_j + \mathbf{C}_j\dot{\mathbf{Q}}_j + \mathbf{K}_j\mathbf{Q}_j = \mathbf{T}_j \tag{5.3}$$

where j = 1 or 2 represents one of the two gear sets, $\mathbf{M}_j$ is the mass matrix, $\mathbf{C}_j$ is the damping matrix, $\mathbf{K}_j$ is the stiffness matrix, and $\mathbf{T}_j$ is the externally applied torque vector. The vector $\mathbf{Q}_j$ contains all the rotational DOFs of the gear set as

$$\mathbf{Q}_j = \begin{bmatrix} \theta_{sj} & \theta_{p1j} & \theta_{p2j} & \theta_{p3j} & \theta_{p4j} & \theta_{cj} \end{bmatrix}^T \tag{5.4}$$

where the subscript s represents the sun gear, the subscripts c represents the carrier and $p1$ to $p4$ represent planet 1 to 4. If the gearbox is free of any defects, the gear meshing stiffness is a function of the gear angular displacement and can be described by a square waveform [57, 66]. The gear meshing stiffness for a pair of teeth is determined by the teeth bending stiffness, fillet-foundation stiffness, and the Hertzian contact stiffness [119]. If a tooth defect is present, a partial loss of the contact occurs whenever the faulty tooth is engaged, resulting in a local reduction in the meshing stiffness function [119] due to the increased flexibility of the gear teeth. The meshing stiffness functions used in simulation for healthy and faulty gear are shown in Figure 5.9. Due to the local reduction in the meshing stiffness, amplitude and phase modulation effects are introduced into the vibration response. These modulation effects appear as sidebands in the

vibration spectrum, whose frequency locations are determined by the gear fault location [92]. Furthermore, these sidebands are also reflected on the stator current obtained from the electrical machines, which is discussed in detail in Section 5.2.3.

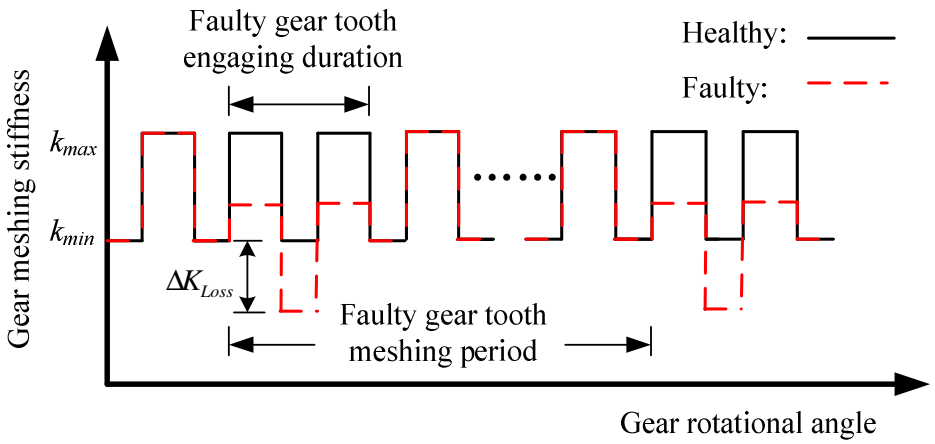

Figure 5.9 Gear meshing stiffness under healthy and faulty conditions

Within the planetary gearbox, the torsional stiffness of the spline which couples the two planetary gear sets in a back-to-back configuration can be estimated as

$$k_{spl} = \pi G\left(d_{splO}{}^4 - d_{splI}{}^4\right)/\left(32 L_{spl}\right) \tag{5.5}$$

where G is the shear modulus, d_{splO} is the outer diameter of the spline, d_{splI} is the inner diameter, and L_{spl} is the spline length.

5.2.2.3 Model of the electro-mechanical power-train

As shown in Figure 5.8, two shaft couplings with different torsional flexibilities are used to couple the two PMSMs with the planetary gearbox on each side, whose stiffness and inertia properties are given in Table 5.3. The low stiffness coupling (*cpl*1) is installed between a sun gear and the driving motor to remove high frequency noise introduced from the motor side, while the high stiffness

coupling (*cpl*2) is installed between sun gear of the other gear set and the load generator.

Table 5.3 Parameters of the shaft couplings

Parameters	Coupling 1(*cpl*1)	Coupling 2(*cpl*2)
Torsional stiffness (kN•m/rad)	1.29	54
Inertia (kg.m^2)	8.7×10^{-4}	8.8×10^{-3}

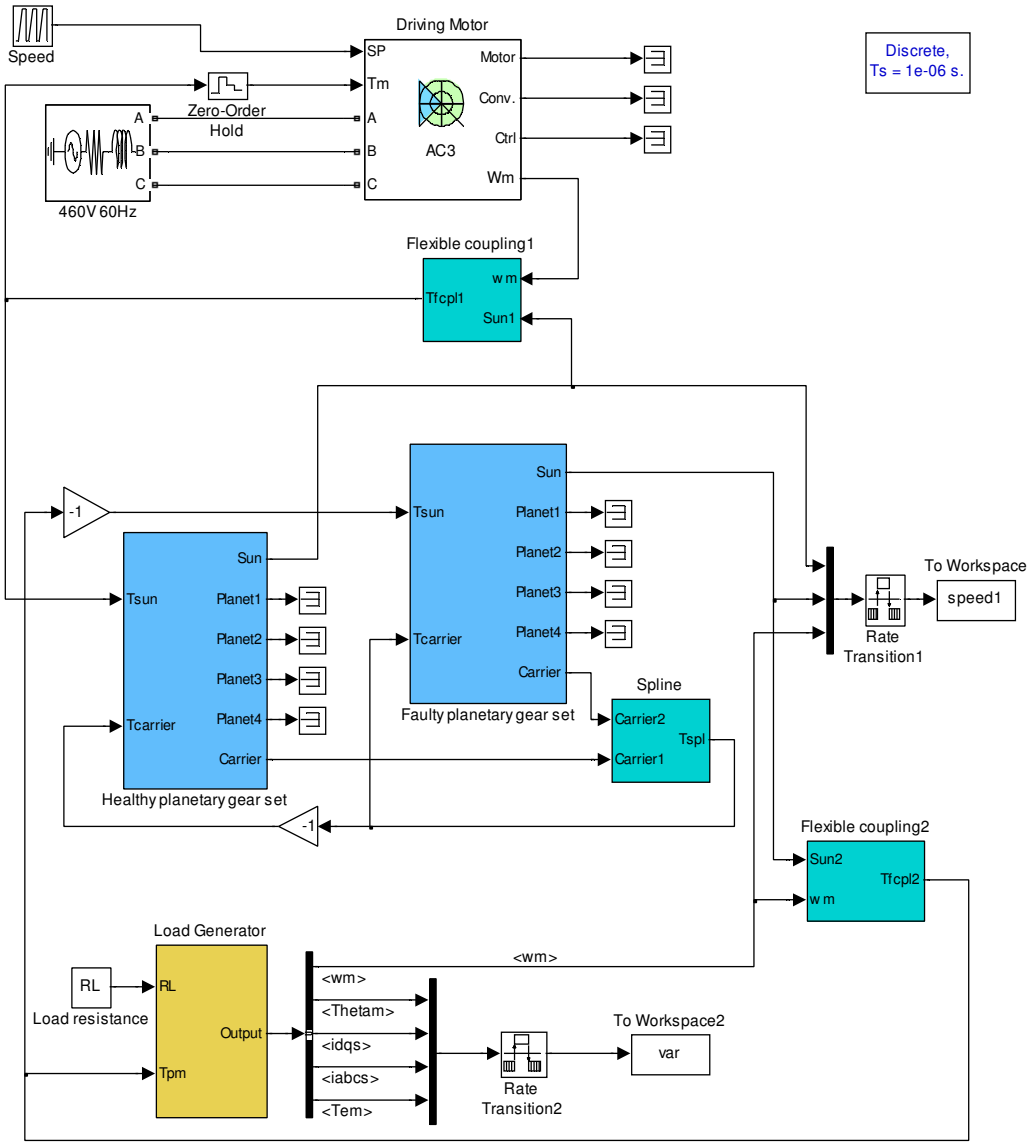

Figure 5.10 Diagram of the EMPT model in SIMULINK

With the model built for the planetary gear set in Section 3.4.2 as well as the PMSM model in Section 5.2.2, the electro-mechanical power-train is modeled in SIMULINK as Figure 5.10.

5.2.3 Resonance residual based fault detection technique

5.2.3.1 Planetary gearbox to load generator rotor transmission

The transmission of the torque fluctuation from the planetary gearbox to the rotor vibration of the load generator is determined by the rotor inertias and the shaft flexibilities. By reflecting the entire gearbox inertia on the sun gear connected with the load generator, an equivalent inertia J_{eq} of the gearbox can be obtained as ([57])

$$J_{eq} = J_{s1} + J_{s2} + 2J_p \cdot P\frac{r_{bs}^2}{4r_{bp}^2} + 2\left(J_c + P \cdot M_p \cdot r_{bc}^2\right)\frac{r_{bs}^2}{4r_{bc}^2} \tag{5.6}$$

where the planetary gearbox comprises of two planetary gear sets, both of which are taken into consideration. J_{s1}= J_s+J_{cpl1}/2 and J_{s2}= J_s+J_{cpl2}/2 are the overall inertia at each sun gear, where half inertia of the couplings are added to the corresponding sun gears. J_s, J_p, J_c, J_{cpl1}, and J_{cpl2} are the inertias of the sun gear, planet, carrier (values provided in Table 5.2), and the coupling 1 and 2 (values provided in Table 5.3) respectively. P is the number of the planet. r_{bs}, r_{bp} and r_{bc} are the base radii of the sun gear, planets and the carrier respectively. M_p is the mass of the planet. The overall power-train can be simplified as a two-mass system shown in Figure 5.11. The governing equations for the simplified two-mass system are

$$J_{eq}\ddot{\theta}_{eq} = T_{eq} - k_{cpl2}\left(\theta_{eq} - \theta_L\right) \tag{5.7a}$$

$$J_L\ddot{\theta}_L = -T_L - k_{cpl2}\left(\theta_L - \theta_{eq}\right) \tag{5.7b}$$

where $J_L = J_M + J_{cpl2}/2$ is the overall inertia of the load generator, θ_{eq} is the angular displacement of the equivalent gearbox inertia, θ_L is the angular displacement of the load generator, T_{eq} is the torque applied on the equivalent inertia, and T_L is the load torque. The damping in shaft and coupling is primarily material based, which is low and therefore can be neglected. Equation 5.7 can be simplified to describe the relationship between the gearbox torque fluctuation and the torsional vibration experienced at the load generator as

$$G_1(\delta) = \frac{\theta_L(\delta)}{T_{eq}(\delta)} = \frac{k_{cpl2}}{J_{eq}J_L\delta^4 + \left(J_{eq} + J_L\right)k_{cpl2}\delta^2} \tag{5.8}$$

where δ is the Laplace variable and the parameters corresponding to the considered testbed are shown in Table 5.1, Table 5.2 and Table 5.3. The frequency response of $G_1(\delta)$ is shown in Figure 5.12(a). It can be observed that $G_1(\delta)$ has a high amplitude gain around the natural frequency f_N of the two-mass system.

$$f_N = \frac{1}{2\pi}\sqrt{k_{cpl2}\left(\frac{1}{J_{eq}} + \frac{1}{J_L}\right)} \tag{5.9}$$

Therefore, the transmitted vibration response from the gearbox side to the load generator has energy concentration around the resonance frequency.

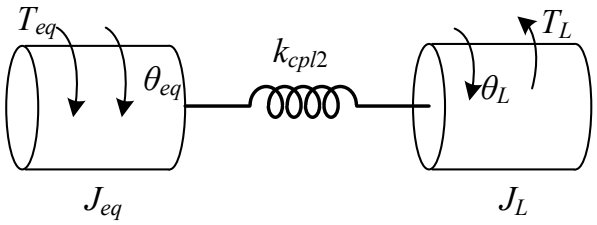

Figure 5.11 Two-mass system representation for load generator with equivalent inertia

5.2.3.2 Effect of generator vibration on stator current

MCSA relies on the reflection of the torsional vibration on the stator current. However, the frequency response function of the stator current to the torsional vibration has not yet been sufficiently investigated in the existing literatures. For a balanced three phase PMSM, the voltage equation of phase *a* is

$$v_{as} = R_s i_{as} + L_{asas}\frac{di_{as}}{dt} + L_{asbs}\frac{di_{bs}}{dt} + L_{ascs}\frac{di_{cs}}{dt} + \frac{d}{dt}\left(\lambda_f' \sin\theta_r\right) \tag{5.10}$$

where L_{asas} is the self-inductance of stator winding *as*, L_{asbs} is the mutual-inductance between the windings *as* and *bs*, L_{ascs} is the mutual-inductance between the windings *as* and *cs*, and θ_r is the electrical angular displacement of the PMSM. The induced stator current is related to the electrical angular displacement as

$$i_{as} = \sqrt{2} I_s \cos\left(\theta_r - \xi - \frac{\pi}{2}\right) \tag{5.11a}$$

$$i_{bs} = \sqrt{2} I_s \cos\left(\theta_r - \xi - \frac{7\pi}{6}\right) \tag{5.11b}$$

$$i_{cs} = \sqrt{2} I_s \cos\left(\theta_r - \xi + \frac{\pi}{6}\right) \tag{5.11c}$$

where I_s is the root mean square of the stator current, and ξ is the lead angle of the rotor magnetic field with respect to the stator magnetic field (generator mode). The inductance of the stator winding

$$L_{asas} = L_{ls} + L_A - L_B \cos 2\theta_r \tag{5.12a}$$

$$L_{asbs} = -\frac{L_A}{2} - L_B \cos 2\left(\theta_r - \frac{\pi}{3}\right) \tag{5.12b}$$

$$L_{ascs} = -\frac{L_A}{2} - L_B \cos 2\left(\theta_r + \frac{\pi}{3}\right) \tag{5.12c}$$

where L_{ls} is the leakage stator inductance, and L_A and L_B are defined as

$$L_A = \frac{1}{3}\left(L_d + L_q - 2L_{ls}\right) \tag{5.13a}$$

$$L_B = \frac{1}{3}\left(L_d - L_q\right) \tag{5.13b}$$

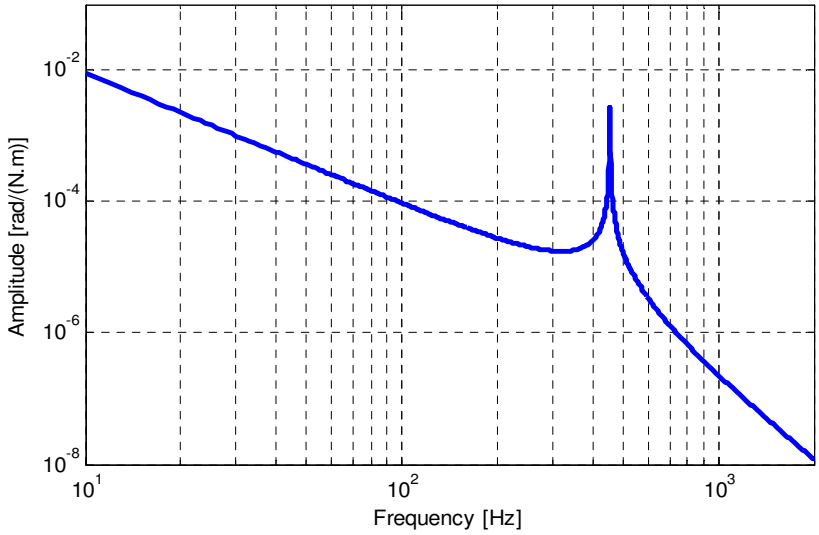

(a)

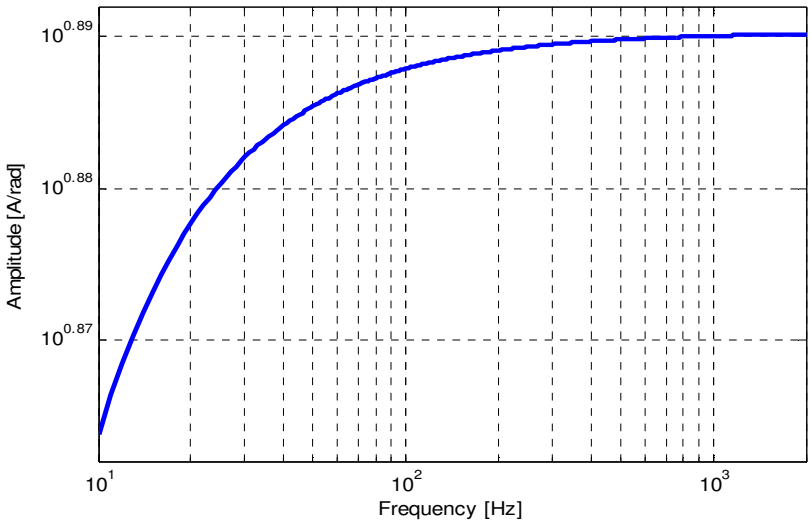

(b)

Figure 5.12 Frequency response functions (a) gearbox torque fluctuation to electrical machine rotor vibration $G_1(\delta)$, and (b) electrical machine rotor vibration to stator current signal $G_2(\delta)$.

Using Eqn. 5.10-5.13, the relationship between the applied stator voltage v_{as}, electrical angular displacement θ_r, and stator current i_{as} for phase a is

$$v_{as} = R_s i_{as} + \left[L_{ls} + \frac{3}{2} L_A - \frac{3}{2} L_B e^{2j(\xi+\pi/2)} \right] \frac{di_{as}}{dt} + \frac{d}{dt}\left(\lambda'_f \sin\theta_r\right) \tag{5.14}$$

θ_r can be partitioned into terms corresponding to nominal speed and a fluctuating component due to torsional vibrations

$$\theta_r = \theta_m \cdot w/2 = \omega_{m0} t \cdot w/2 + \Delta\theta_m \cdot w/2 \tag{5.15}$$

where w is the number of poles of the PMSM. The nominal speed ω_{m0} is a constant and does not affect frequency response. Therefore, it can be neglected. The amplitude of $\Delta\theta_m$ is usually low, resulting in $\sin(\Delta\theta_m) \approx \Delta\theta_m$. Thus, Eqn.5.14 can be rewritten as

$$v_{as} = R_s i_{as} + \left[L_{ls} + \frac{3}{2} L_A - \frac{3}{2} L_B e^{2j(\xi+\pi/2)} \right] \frac{di_{as}}{dt} + \lambda'_f \frac{w}{2} \frac{d}{dt} \Delta\theta_m \tag{5.16}$$

Furthermore, the transmission of the torsional vibration to the stator current signal can be derived as

$$G_2(\delta) = \frac{i_{as}(\delta)}{\Delta\theta_m(\delta)} = \frac{-\lambda'_f \frac{w}{2}\delta}{R_s + \left[L_{ls} + \frac{3}{2} L_A - \frac{3}{2} L_B e^{2j(\xi+\pi/2)} \right]\delta} \tag{5.17}$$

Equation 5.17 shows that the rotor speed oscillation $\Delta\theta_m$ can be reflected onto the stator current i_{as}, where the PMSM parameters are described in Table 5.1. The lead angle ξ is assumed to be $2\pi/3$, which is typical in PMSMs. Figure 5.12(b) shows the frequency response of $G_2(\delta)$. It can be observed that in the lower frequency range, the amplitude response from $\Delta\theta_m$ to i_{as} increases with the frequency, and approaches a constant in the higher frequency range. The corner frequency which lies between these two regions is determined by the

parameters of the PMSM. Thus, Eqn. 5.8 shows that the vibration signature can be transmitted from the gearbox to the connected rotor of the PMSM wherein a peak amplitude in transmission function is observed around the natural frequency of the power-train, and Eqn. 5.17 shows that the mechanical vibration reflected onto the stator current has a constant amplitude of the frequency response function after the corner point. This implies that detecting gear fault using sidebands in measured current signals around the power-train's natural frequency should be feasible. The remainder of this section presents a fault detection algorithm based on MCSA that utilizes the peak in the transmission function response around the natural frequency of the power-train.

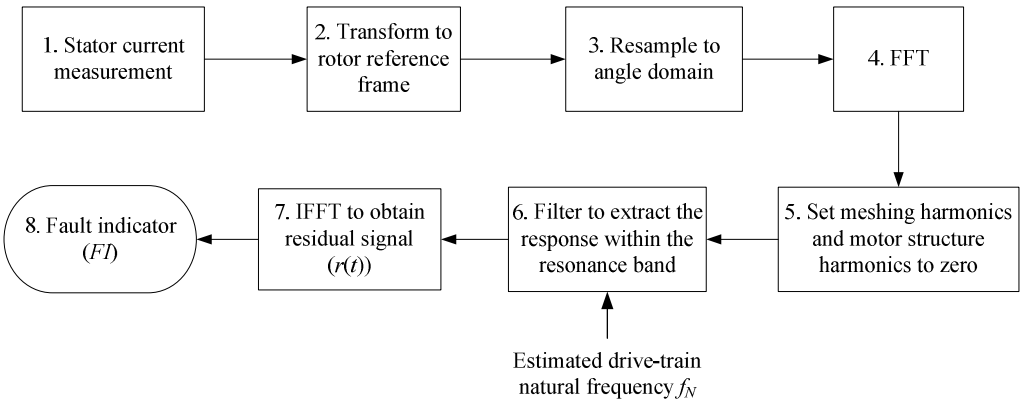

Figure 5.13 Fault detection algorithm based on resonance residual approach

5.2.3.3 Fault detection algorithm

As discussed earlier, a gear tooth fault results in amplitude and phase modulation of the nominal vibration signal, which can be detected by monitoring the sideband patterns in the vibration spectra. Also, these gear vibration signals can be transmitted to the rotor of the load generator, where the dominant sidebands are expected to be around the structural frequency of the

power-train. Therefore, the reflection of the sidebands on the stator current enables detection of the gear fault by MCSA. Figure 5.13 shows a proposed fault detection algorithm for a gearbox connected to a PMSM through the measured stator current using the resonance residual technique. First, the stator current is transformed from stationary reference frame (*abc*) to rotor reference frame (*d-q*) to remove the fundamental line frequency f_e which otherwise may mask the sidebands arising from the fault. Then, the signal is resampled from the time domain to the angle domain/shaft order domain to remove the influence of small speed / load fluctuations that often blur the obtained current spectra. This step improves the signal to noise characteristics of the measurements [65]. To obtain the spectrum of the current signal with respect to the shaft orders, Fast Fourier Transform (FFT) is adopted. However, for presentation of results, stator current spectrum is shown in the frequency domain where frequency = shaft order × nominal operating speed × number of pole pair. Presenting the results using the frequency domain instead of shaft order domain allows the readers to easily locate the resonance region in presented spectra. In the obtained current spectrum, the gear meshing frequency and its harmonics, as well as the identified harmonics due to the electric machine structure are set to zero. For this step, measuring the stator current spectrum of generator without connecting it to the gearbox can predetermine the harmonics resulting from the electrical machine structure. The signal is then band-pass filtered to remove the stator current response and noise outside the resonance band. The center frequency of the filter is set as the natural frequency f_N of the power-train corresponding to the gearbox-generator coupling estimated using Eqn. 5.9.

Inverse Fast Fourier Transform (IFFT) is utilized to obtain the residual signal $r(t)$. Finally, a fault indicator *FI*, similar to that proposed in [93], is evaluated to indicate the health condition of the gearbox as

$$FI = PP\left(r(t)\right) \Big/ \sum A_{GM,i} \tag{5.18}$$

where $PP(r(t))$ is the peak to peak value of the residual signal $r(t)$ to measure the amplitude fluctuation, and $\sum A_{GM,i}$ is the summation of the amplitude of the meshing frequency and its harmonics determined by the operating conditions.

5.2.4 Simulation results

5.2.4.1 Results from SIMULINK

Table 5.1, Table 5.2 and Table 5.3 provide the parameters for the shaft couplings, three-phase PMSM, and the planetary gear set. The stiffness of the two flexible couplings are k_{cpl1} = 1.29kN•m/rad and k_{cpl2} = 54kN•m/rad, while the rotational gear meshing stiffness is significantly higher than the above two. The natural frequencies of the power-train assembly can be evaluated as the solutions of the equation $det(-\mathbf{M}\omega^2+\mathbf{K})=0$ [32]. Because of the free boundary conditions at the rotor inertias of electric machines, the first solution is zero, which corresponds to the rigid body mode. This mode can be neglected in the vibration response analysis of the system. Further, it can be seen from Figure 5.12(a) that the response transmission of vibration signal from gearbox to generator side attenuates quickly as the frequency increases. Therefore, only the next three frequencies determined as 90, 449, and 2530Hz are considered. A lower stiffness results in a lower structural frequency. Therefore, the first

natural frequency is found to be associated to coupling 1 (between the driving motor and gearbox) which has the lowest corresponding stiffness. The second natural frequency is found to be associated to coupling 2 between the load generator and the gearbox, and the third natural frequency is associated to the meshing among the gears which is significantly stiffer.

In the simulation, the operating condition for the power-train is set as: operating speed = 600rpm, load power = 0.76kW, and load torque = 12.1N.m (which is the same as the operating condition I used in experimental study as shown in Table 5.4). A healthy gearbox is simulated first, followed by a gearbox with cracked annulus gear tooth. At this operating speed, the gear meshing frequency equals to 210Hz and the fault in the annulus gear will excite sidebands with spacing equal to be 10Hz. Fluctuations in stator current are observed even for the healthy planetary gearbox, which is a result of the variation in the gear meshing stiffness with respect to the rotational angle. Such oscillations evaluated from a healthy planetary gearbox are illustrated in Figure 5.14(a). Finite element analysis using ANSYS estimated that losing one third of a teeth in the annulus gear results in a local drop of around 0.2×10^8 N/(rad.m) in gear meshing stiffness function as in Section 3.4.2. This local reduction excites a periodic impulse in the torsional vibration which is reflected on the stator current signal as shown in Figure 5.14(b).

Under healthy condition, the gear meshing frequency and its harmonics are the dominant frequency components in the spectrum of the stator current (Figure 5.15(a)). A few sidebands with low amplitude can be observed around 449 Hz

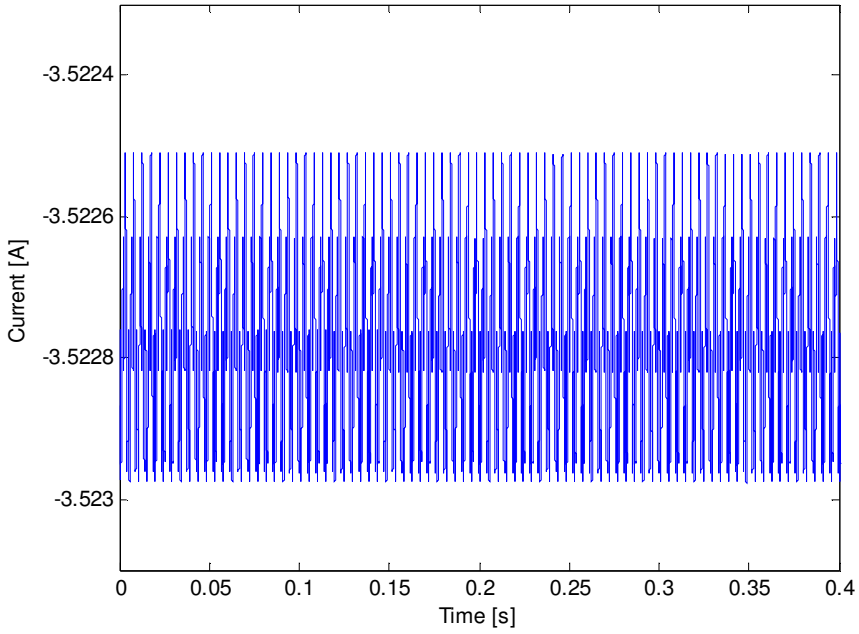

(a)

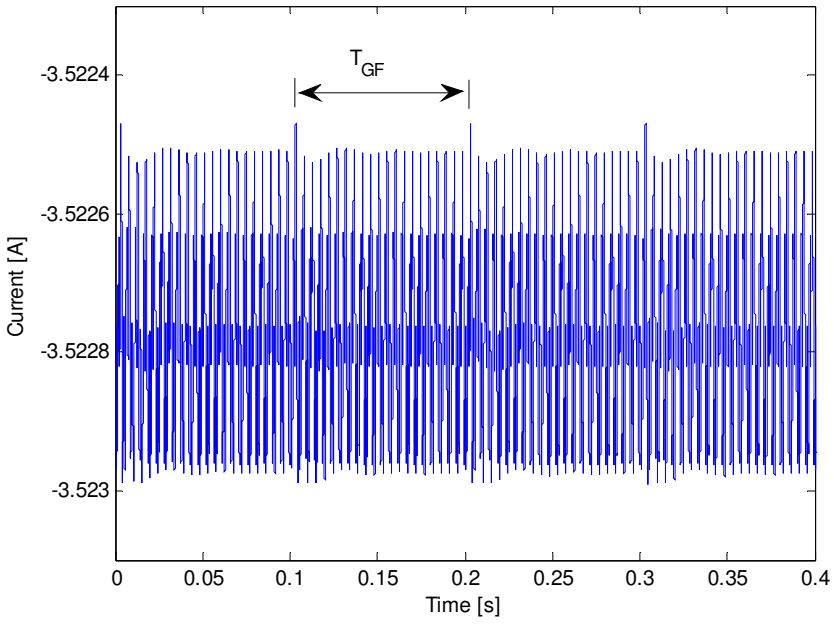

(b)

Figure 5.14 Time waveform of the stator current i_d (a) healthy condition, and (b) gear tooth crack

which is the natural frequency of the power-train (corresponding to the gearbox generator coupling). The appearance of those sidebands can be attributed to the

interaction between gear meshing frequency and the natural frequencies. However, in presence of fault, several more sidebands having significantly higher amplitude can be observed in Figure 5.15(b). Further, it is noteworthy to observe that the amplitude of the sidebands at the low frequencies and those around the 449Hz resonance frequency are comparable. However, there are more sidebands in the latter location.

Using the proposed resonance residual technique shown in Figure 5.13, the residual signals for both the healthy and faulty simulated cases are obtained in Figure 5.16. The parameters used in the algorithm are as follows. In Step 5, the gear meshing frequency 210Hz and its harmonics are set to be zero in the stator current spectra. In Step 6, a band pass filter with a low cutoff frequency of 400 Hz and a high cutoff frequency of 500 Hz is used to extract the sidebands around the evaluated natural frequency. In Step 7, IFFT command in MATLAB is applied on the band passed signal to obtain the residual signal $r(t)$. Finally, the fault indicator value in Eqn. 5.18 is evaluated to monitor the health condition of the gearbox. Periodic high peaks having time period corresponding to the annulus gear fault can be observed in the residual signal obtained from the faulty gearbox case in Figure 5.16, indicating a fault at the annulus gear teeth of the planetary gearbox. The corresponding fault indicators for the faulty and healthy gearbox are 8.9×10^{-3} and 2.8×10^{-3} respectively. Thus, it can be seen that a gearbox fault produces a higher fault indicator value than the healthy case demonstrating the capability of proposed algorithm to detect planetary gearbox faults through MCSA. In the next section, the capability of the proposed

algorithm to detect planetary gearbox faults is further verified through experiments.

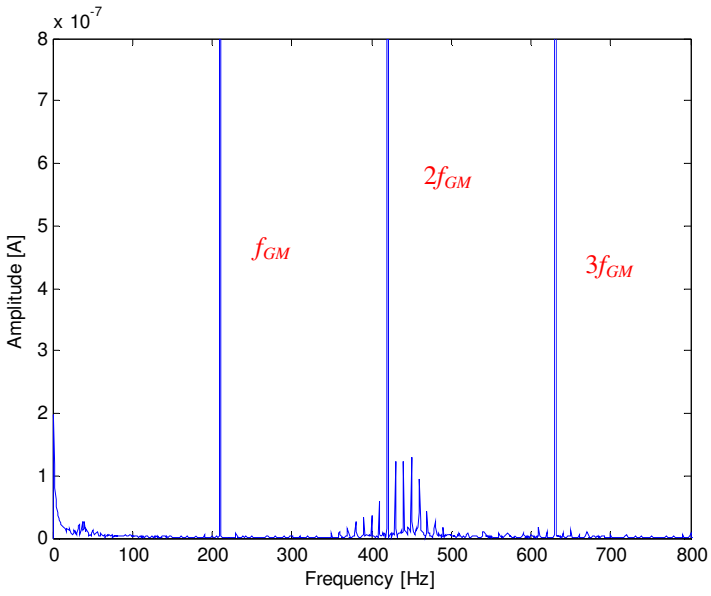

(a)

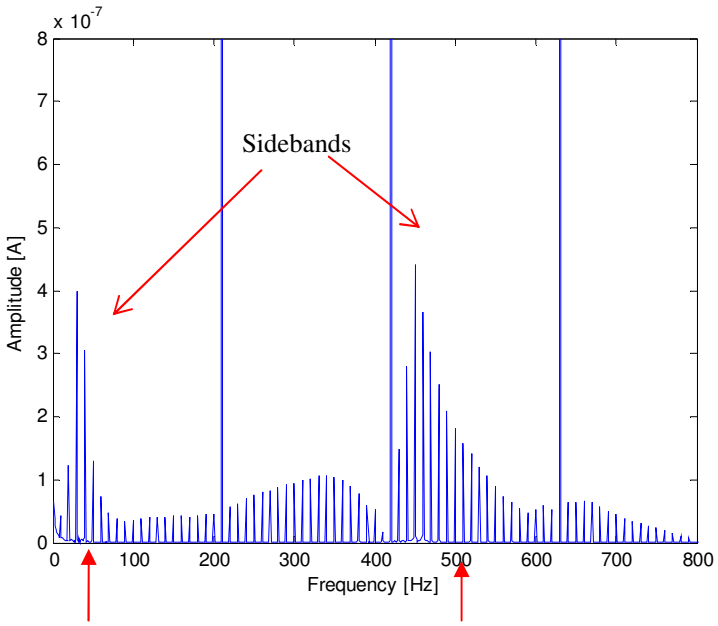

(b)

Figure 5.15 Sidebands excited in the spectra of the stator current (a) healthy condition, and (b) gear tooth crack.

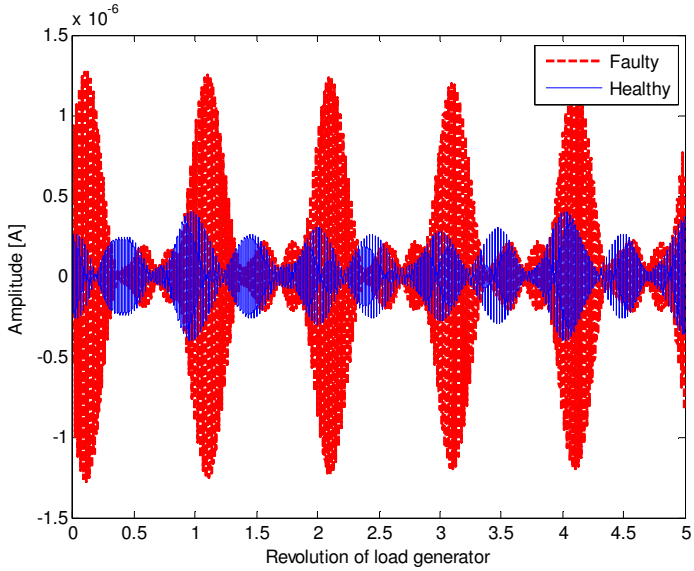

Figure 5.16 Evaluated residual signals obtained from the stator current.

Table 5.4 Parameters for experimental operating conditions

Case	Speed (rpm)	Power (kW)	Load torque (N.m)	Gear meshing frequency f_{GM} (Hz)	Gear fault frequency f_{GF} (Hz)
I	600	0.76	12.1	210	10
II	600	0.26	4.2	210	10
III	1500	2.0	12.7	525	25

5.2.4.2 Results from a nonlinear model built in ANSOFT

To explore the dynamics response of stator current to vibration signature induced by the gear tooth fault in the practical electric machines, a nonlinear analytical model built in ANSOFT for the PMSM in Section 3.3.2 is utilized, where the speed of the load generator acquired from Section 5.2.3 is used as the speed input of the PMSM. The spectra of the stator current with gear tooth fault are shown in Figure 5.17, where it can be seen that lots of sidebands are excited

in the resonance region while there are few sidebands in the lower frequency range.

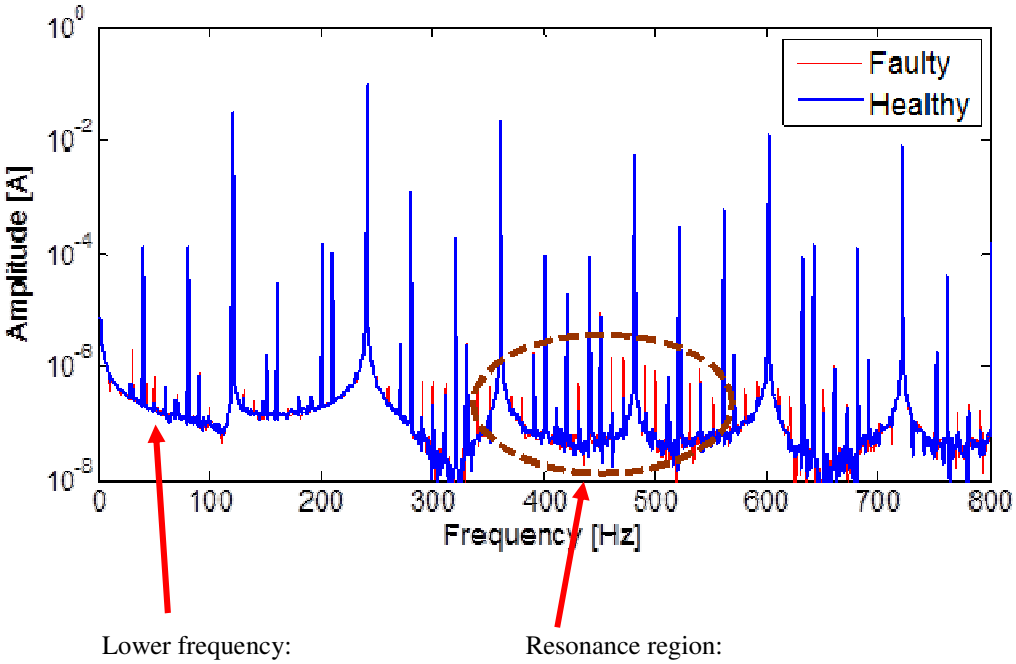

Figure 5.17 Stator current spectra under faulty gear tooth based on model in ANSOFT

5.2.5 Experimental validation

The proposed fault detection method is experimentally verified using an EMPT testbed whose configuration was shown earlier in Figure 5.8. An annulus gear tooth crack is created on the second gear set by removing 1/3rd of a tooth (Figure 5.7). The speed command of the driving motor is output through an analog signal from dSPACE 1104. The electricity generated by the load generator is dissipated at a resistive load bank at different power steps. The current of the load generator are measured by three Hall Effect sensors. The rotor speed of generator is measured by an incremental encoder having 5000 pulses per revolution. The power-train was operated under three different operating conditions (Table 5.4) to show both the effectiveness of the proposed

method over the existing ones and its robustness to detect faults under different operating conditions.

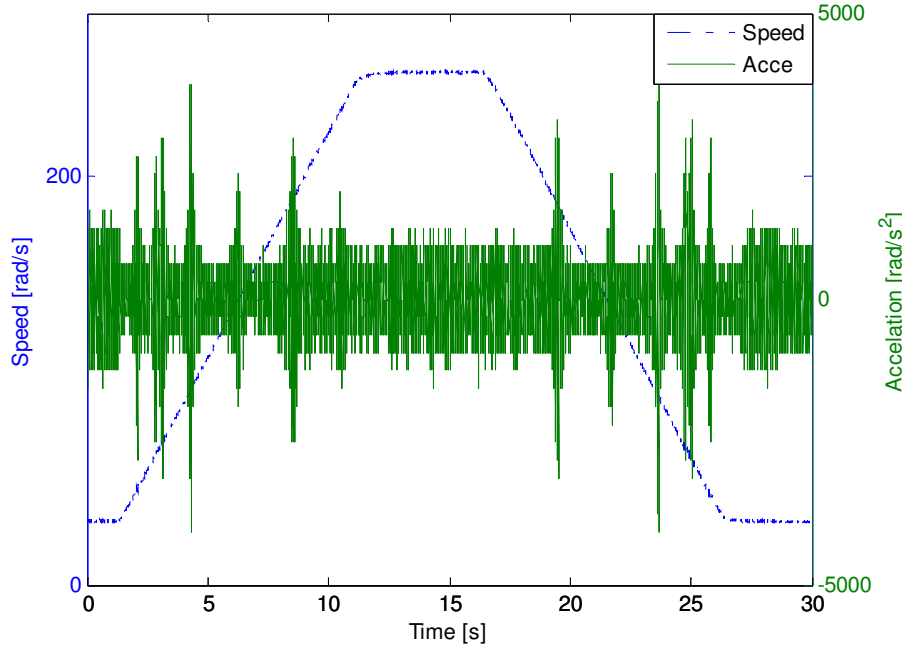

(a)

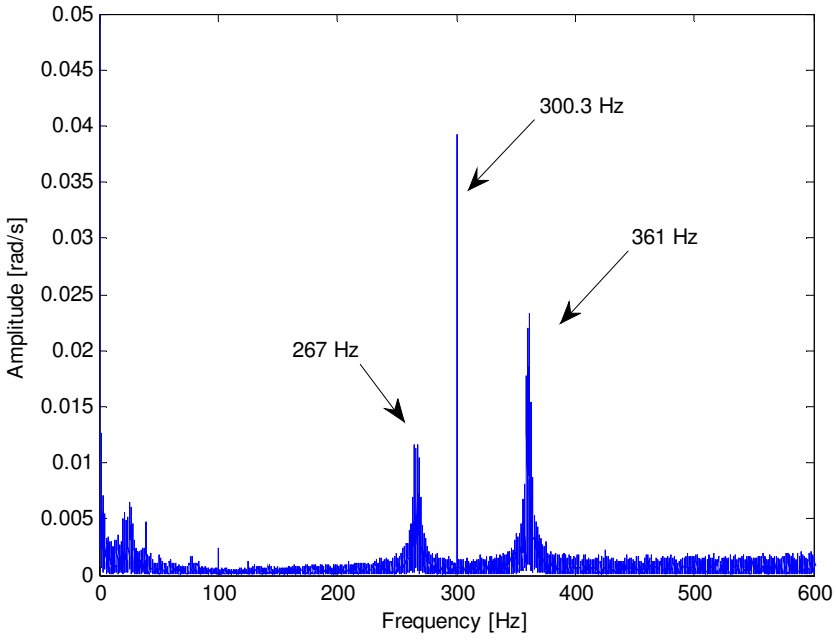

(b)

Figure 5.18 Identification of PMSM's dominant structural frequencies (a) speed and acceleration plots for load generator, and (b) spectrum of measured speed.

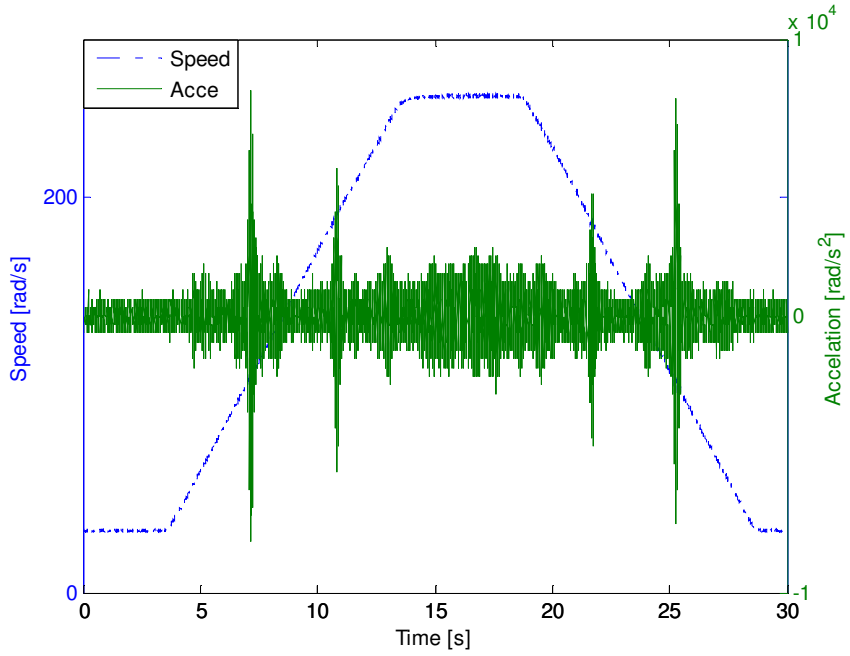

(a)

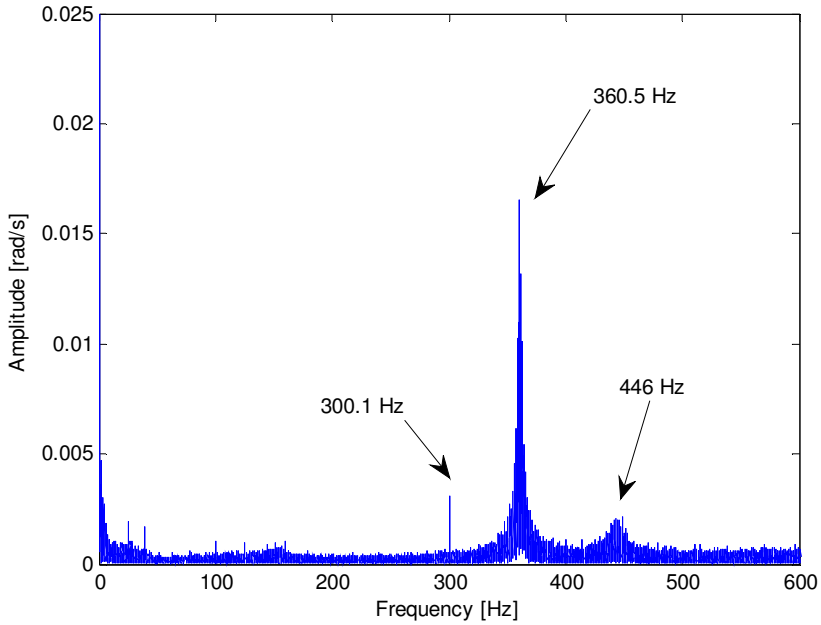

(b)

Figure 5.19 Identification of the overall power-train structural frequencies (a) speed and acceleration plots of load generator, and (b) spectrum of measured speed.

5.2.5.1 Identification of the power-train's natural frequencies

The PMSM injects several dominant frequencies due to its own structure in the measured current spectra. These dominant frequencies from the motor structure can affect the fault detection process and therefore must be identified beforehand. For this, the driving motor is directly connected to the load generator through coupling 1. Its low stiffness isolates the vibration of the PMSMs from each other. Afterwards, the motor is given a ramp speed command from 300 to 2400rpm followed by deceleration as shown in Figure 5.18(a). Whenever the operating speed of the motor matches one of the structural/ resonance frequencies, large speed oscillations can be observed in the measured encoder signal. The acceleration curve of the load generator, obtained by differentiating the speed measured from the encoder, shows several such resonances (Figure 5.18(a)). Three dominant structural frequencies were excited at the load generator speed: 267, 300, and 361Hz (Figure 5.18(b)). Afterwards, the planetary gearbox is installed to investigate the natural frequencies of the power-train with the same speed profile, where a new dominant component (around 446Hz) can be found in the spectrum of the load generator speed (Figure 5.19). Compared with the previous theoretical results, it can be determined that the 446 Hz component is the natural frequency of the power-train arising from the flexibility of the generator gearbox connection.

5.2.5.2 Detection of gear tooth crack using stator current

The stator current spectrum of a healthy planetary gearbox under operation condition I are shown as an example in Figure 5.20 to demonstrate its

complexity due to dominant frequency components from different sources. Even under the presumed healthy condition, several dominant frequency components can be observed, which arises from the gear meshing frequency f_{GM} (given in Table 5.4) and its harmonics, as well as the manufacturing and installation errors of the power-train. Furthermore, harmonics resulting from the PMSM structure [36, 37] are also reflected in the stator current. These harmonics were not reflected in the simulation study presented earlier using Park's model, as this model assumed that, (1) the number of the stator winding coils is distributed sinusoidally around the stator, (2) magnetic saturation does not occur, (3) the influence of the slot on the magnetic permeance is negligible, (4) the higher order harmonics due to distribution of permanent magnet materials can be ignored, and (5) the three-phase winding is ideally balanced. For the described experimental test rig, it was identified that the PMSM introduced significant contributions at the 1^{st}, 2^{nd}, 3^{rd}, 4^{th}, 6^{th}, 12^{th}, 14^{th}, 16^{th}, 18^{th}, 21^{st}, and 24^{th} harmonics of the fundamental frequency as in Figure 5.20(a).

The application of the proposed algorithm for experimental investigation is similar to that for simulation study. First, the measured stator current is transformed to the rotor reference frame to remove the fundamental line frequency, followed by resampling to angle domain to remove the speed fluctuation in the power-train. Afterwards, the spectra of the measured stator current are obtained using FFT. In Step 5, the gear meshing frequency f_{GM} (Table 5.4) and its harmonics, as well as the before mentioned PMSM structure induced harmonics are set to be zero in the spectra. In Step 6, a band pass filter

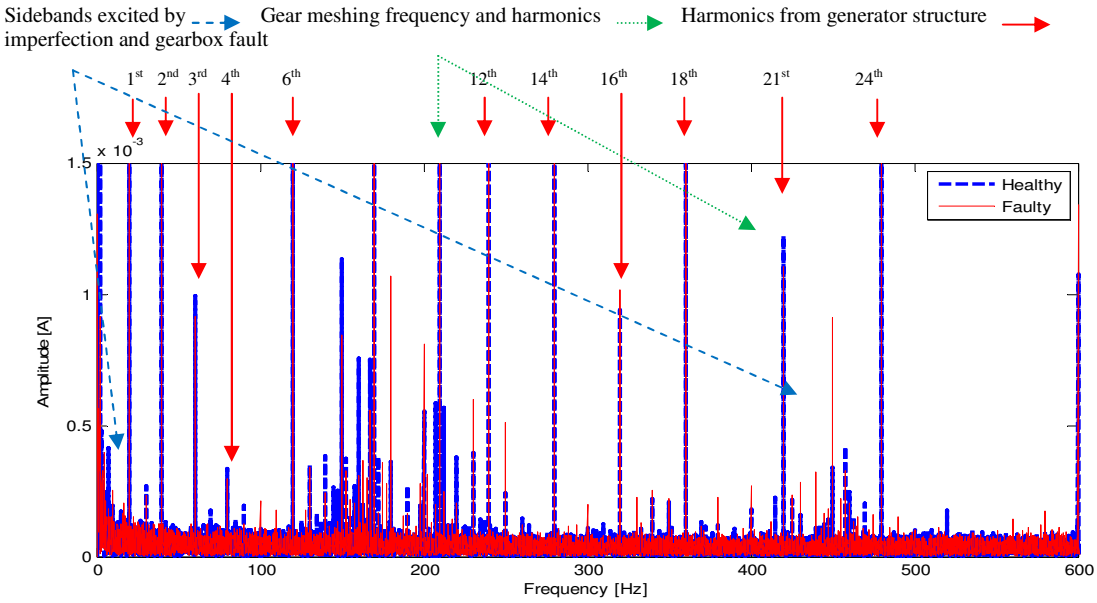

(a)

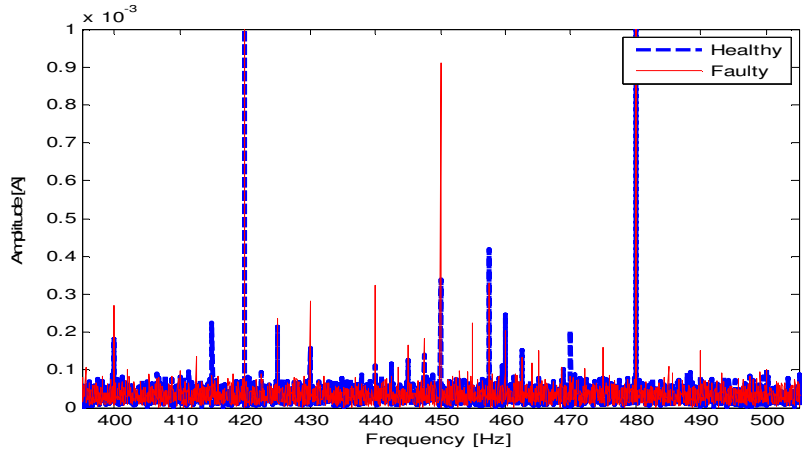

(b)

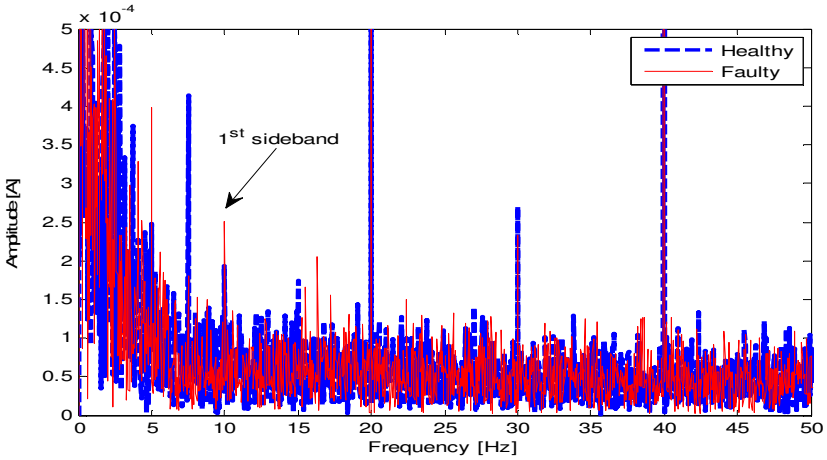

(c)

Figure 5.20 The stator current spectra of load generator (a) overall frequency band, (b) around structural frequency, and (c) in low frequency range.

with low cutoff frequency 400 and high cutoff frequency 500 Hz is used to extract the rich gear fault information around the resonance frequency 446Hz as in Figure 5.20. In Step 7, IFFT of the band passed signal produces the residual signal $r(t)$ as in Figure 5.21. Finally, the health condition can be identified by the fault indicator in Eqn. 5.18. The robustness of the proposed method was investigated through three different operating conditions I, II and III (Table 5.4), where the corresponding fault indicator values for both the faulty and healthy gearboxes as well as their ratios are shown in Table 5.5. From Table 5.5, it can be seen that the evaluated fault indicator value depends on the operating conditions of the experiments. Therefore, the fault indicator value evaluated at one particular operating condition cannot be used as a reference to monitor the gearbox health running under another operating condition. Further, it can be seen that the fault indicator ratio is sensitive to the load torque, where a high load torque results in a larger ratio between the faulty and healthy conditions. Therefore, to implement the proposed method, the fault indicator for the healthy gearbox should be pre-determined in its range of operating speed and load. The thresholds for indicating gearbox faults can be set based on the fault indicator ratio between the faulty and healthy gearboxes at a given operating condition. During its operation, the fault indicator can be monitored continuously, where an increase beyond the threshold limit indicates a fault in the gearbox.

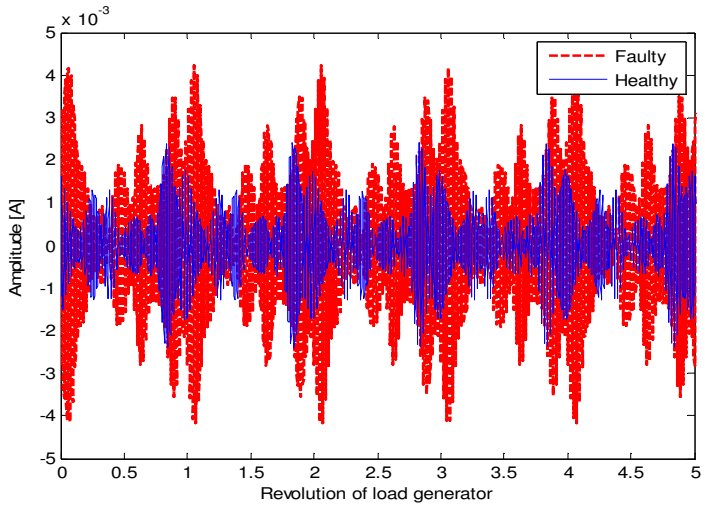

(a)

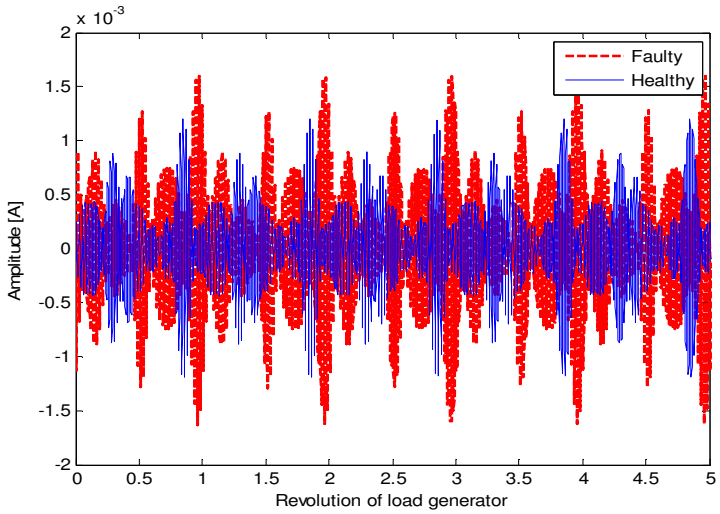

(b)

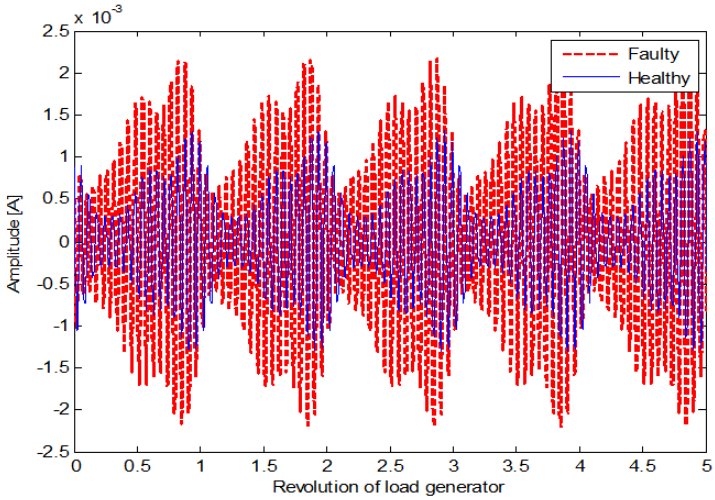

(c)

Figure 5.21 Residual signal of the stator current (a) operating condition I, (b) operating condition II, and (c) operating condition III

Existing fault detection methods based on MCSA utilize the amplitude of the sidebands in the lower frequency range of the stator current spectra as an indicator to monitor a gearbox's health condition [145-148]. For the conducted experiments, only the 1st sideband corresponding to the annulus gear tooth crack in the lower frequency range of current spectra shows apparent increase (Figure 5.20(c)). Therefore, this particular sideband was used as a fault indicator of the gearbox health condition as well, where the fault indicator is rescaled by the $\sum A_{GM,i}$ as in Eqn. 5.18. With the existing methods, the fault indicators for the faulty and healthy gearboxes and their ratios are also given in Table 5.5. Comparison of the fault indicators obtained from the existing method and the proposed method shows that the former produces a lower fault indicator ratio. Thus, the proposed method is more effective in detecting the gearbox fault through MCSA.

Table 5.5 Fault indicators from existing and proposed methods

Case	FI from existing method			FI from proposed method		
	Healthy	Faulty	Ratio	Healthy	Faulty	Ratio
I	0.41	0.53	1.29	1.02	1.74	1.71
II	0.91	1.12	1.23	1.77	2.33	1.35
III	1.14	1.35	1.18	0.21	0.35	1.67

5.2.6 Conclusion

In this section, a novel fault detection scheme that extracts rich fault information from the frequency region in vicinity of power-train resonance in measured stator current spectrum is developed and implemented. This approach

is applied through both simulations and experiments to an electro-mechanical power-train consisting of a driving motor connected to a load generator through a back-to-back planetary gearbox. The frequency response functions of the transmitted vibration from gearbox to electrical machine rotor, and from rotor vibration to stator current response are presented to show that the sidebands in the vicinity of power-train natural frequency of current spectrum contain rich fault information. The first frequency response function has a high amplitude relationship around the power-train natural frequency, while the second one has higher amplitude at the higher range of frequencies. Both simulations and experiments show a significant presence of sidebands in the current spectrum in vicinity of power-train natural frequency. The proposed algorithm is applied to experiments conducted at different operating conditions. It is shown that the fault indicator determined by proposed approach is more sensitive to presence of gearbox faults as compared to existing MCSA based approaches.

Chapter 6 Concluding and Remarks

The electro-mechanical power-trains (EMPTs) are now utilized in many applications. Compared with the conventional power-trains, the EMPTs provide higher fuel efficiency, better dynamic performance, and lower maintenance costs because, (1) the electrical components can decouple the power generation stage from the load part, which enables the engine to operate always with high efficiency, and (2) the electrical drives have a faster and smoother response than the internal combustion engines.

However, the following factors challenge the reliability and applicability of EMPTs:

(1) Modeling of the EMPTs is challenging due to the immense variation in required model selection and approach with respect to the EMPTs' configuration and the research applications. Furthermore, there is a lack of the efficient model development techniques that offer a good overall electro-mechanical modeling capability.

(2) The resulting challenge in being able to model the nonlinear dynamics of the power-trains has let to insufficient investigation and lack of the design optimization knowledge, for example, appropriate gearbox selection to reduce the vibration and noise in the power-trains.

(3) The electro-mechanical interactions have not been fully revealed, especially the reflection of the vibration signature onto the stator current of electric

machines. As a result, the stator current has not been effectively utilized to analyze the dynamics and carry out condition monitoring of the EMPTs.

6.1 Contributions of this Thesis

To deal with the above mentioned research concerns on EMPTs, the following three key contributions have been demonstrated in this presented thesis:

(1) A systematic co-simulation strategy, which utilizes the extensive model libraries from block diagram (as available in MATLAB/SIMULINK), multi-body system (such as SIMPACK), bond graph (such as 20-SIM), and finite element analysis (such as ANSYS and ANSOFT), was presented to model the EMPTs of various configurations for different research applications. The proposed co-simulation strategy is applicable to different EMPT configurations and can leverage on the model libraries to model healthy and faulty power-train components accurately.

(2) A new analytical formulation to estimate the noise level due to the nonlinear dynamic response exhibited by gear rattle in a typical automotive power-train was developed. This formulation evaluated the effect of important gear design parameters on the gear rattle vibration and noise level and thus can provide a guideline in gearbox design to reduce the rattle noise concern. The formulation was verified using co-simulation of automotive power-train model in SIMPACK along with model library approach in MATLAB/ SIMULINK. The results were also verified using existing experimental data available in literatures.

(3) The electro-mechanical interactions were investigated through evaluation of transfer function between the gearbox vibration and the stator current of the electric machines. Based on this investigation, a novel condition health monitoring (CHM) method based on the resonance residual technique is proposed for the EMPTs through the measured stator current. Compared with the existing CHM methods, this new method is more sensitive to incipient faults in the EMPTs.

6.2 Future Work

Although the proposed CHM method for EMPTs is shown to be more sensitive to the incipient faults than the existing methods, there is still some work to be done in the future, including

(1) The performance of the proposed CHM method has only been explored under steady speed. Thus, the CHM under unsteady speed condition will be investigated in the future.

(2) The proposed CHM method was carried out on a load generator connected to a pure resistive load in order to remove the nonlinearity and interference introduced by the power electronics inverter and controller. To study the influence of power electronics and control algorithms, the CHM will be implemented at the driving motor side driven by the inverter in the future.

Bibliography

[1] I. Moir and A. G. Seabridge, *Aircraft systems : mechanical, electrical, and avionics subsystems integration*, 3rd ed. Chichester, West Sussex, England ; Hoboken, NJ: Wiley, 2008.

[2] H. Zhang, C. Saudemont, B. Robyns, and M. Petit, "Comparison of technical features between a More Electric Aircraft and a Hybrid Electric Vehicle," in *Vehicle Power and Propulsion Conference, 2008. VPPC '08. IEEE*, 2008, pp. 1-6.

[3] J. A. Rosero, J. A. Ortega, E. Aldabas, and L. Romeral, "Moving towards a more electric aircraft," *Aerospace and Electronic Systems Magazine, IEEE,* vol. 22, pp. 3-9, 2007.

[4] Z. He, F. Mollet, C. Saudemont, and B. Robyns, "Experimental validation of energy storage system management strategies for a local DC distribution system of More Electric Aircraft," *IEEE Transactions on Industrial Electronics,* vol. 57, pp. 3905-3916, 2010.

[5] U. Kiencke and L. Nielsen, *Automotive control systems : for engine, driveline, and vehicle*, 2nd ed. Berlin: Springer, 2005.

[6] T. Katrasnik, "Hybridization of powertrain and downsizing of IC engine - A way to reduce fuel consumption and pollutant emissions - Part 1," *Energy Conversion and Management,* vol. 48, pp. 1411-23, 2007.

[7] I. Husain, *Electric and hybrid vehicles : design fundamentals*, 2nd ed. Boca Raton: CRC Press, 2011.

[8] Wikipedia, "Internal combustion engine," ed, 2013.

[9] P.-A. Michael, *Decreasing fuel consumption and exhaust gas emissions in transportation*. New York: Springer, 2012.

[10] R. Izadi-Zamanabadi and M. Blanke, "A ship propulsion system as a benchmark for fault-tolerant control," *Control Engineering Practice,* vol. 7, pp. 227-39, 1999.

[11] T. I. Fossen, *Guidance and control of ocean vehicles*. Chichester ; New York: Wiley, 1994.

[12] S. N. Dogan, "Loose part vibration in vehicle transmissions - gear rattle," *Turkish Journal of Engineering and Environmental Sciences/Turk Muhendislik ve Cevre Bilimleri Dergisi,* vol. 23, pp. 439-454, 1999.

[13] M. L. Adams, *Rotating machinery vibration : from analysis to troubleshooting*. New York: Marcel Dekker, 2001.

[14] E. F. Merrill, "Torsional dynamics of AC electrical machines and systems," in *Conference Record of 1994 Annual Pulp and Paper Industry Technical Conference*, 1994, pp. 52-59.

[15] H. H. Lin, R. L. Huston, and J. J. Coy, "On dynamic loads in parallel shaft transmissions: part I-modelling and analysis," *Journal of mechanisms, transmissions, and automation in design,* vol. 110, pp. 221-225, 1988.

[16] A. Farshidianfar, M. Ebrahimi, and H. Bartlett, "Hybrid modelling and simulation of the torsional vibration of vehicle driveline systems," *Proceedings of the Institution of Mechanical Engineers, Part D: Journal of Automobile Engineering,* vol. 215, pp. 217-228, 2001.

[17] D. Jelaska, *Gears and gear drives*. Chichester, West Sussex ; Hoboken: John Wiley & Sons, 2012.

[18] D. J. Inman, *Engineering vibration*, 2nd ed. Upper Saddle River, N.J.: Prentice Hall, 2001.

[19] S. H. Kia, H. Henao, and G. A. Capolino, "Torsional vibration effects on induction machine current and torque signatures in gearbox-based electromechanical system," *IEEE Transcations on Industrial Electronics,* vol. 56, pp. 4689-99, 2009.

[20] C. J. Li and H. Lee, "Gear fatigue crack prognosis using embedded model, gear dynamic model and fracture mechanics," *Mechanical Systems and Signal Processing,* vol. 19, pp. 836-46, 2005.

[21] W. A. Tuplin, "Gear-tooth stresses at high speed," *Institution of Mechanical Engineers -- Proceedings,* vol. 163, pp. 162-167, 1950.

[22] H. N. Özgüven, "A non-linear mathematical model for dynamic analysis of spur gears including shaft and bearing dynamics," *Journal of Sound and Vibration,* vol. 145, pp. 239-260, 1991.

[23] L. Walha, T. Fakhfakh, and M. Haddar, "Nonlinear dynamics of a two-stage gear system with mesh stiffness fluctuation, bearing flexibility and backlash," *Mechanism and Machine Theory,* vol. 44, pp. 1058-1069, 2009.

[24] C. Siyu, T. Jinyuan, L. Caiwang, and W. Qibo, "Nonlinear dynamic characteristics of geared rotor bearing systems with dynamic backlash and friction," *Mechanism and Machine Theory,* vol. 46, pp. 466-478, 2011.

[25] M. A. Sargeant, S. J. Drew, and B. J. Stone, "Coupled torsional and transverse vibration of a back-to-back gearbox rig," *Proceedings of the Institution of Mechanical Engineers, Part K (Journal of Multi-Body Dynamics),* vol. 219, pp. 259-73, 2005.

[26] S. Sassi, B. Badri, and M. Thomas, "A numerical model to predict damaged bearing vibrations," *Journal of Vibration and Control,* vol. 13, pp. 1603-1628, 2007.

[27] T. Doguer, J. Strackeljan, and P. Tkachuk, "Using a dynamic roller bearing model under varying fault parameters," presented at the The sixth International Conference on Condition Monitoring and Machinery Failure Prevention-CM2009, Dublin, 2009.

[28] C. Mi, A. Masrur, and D. W. Gao, *Hybrid electric vehicles : principles and applications with practical perspectives*. Chichester, West Sussex, U.K. ; Hoboken, N.J.: Wiley, 2011.

[29] K. Govindswamy, T. Wellmann, and G. Eisele, "Aspects of NVH integration in hybrid vehicles," in *SAE 2009 Noise and Vibration Conference and Exhibition, NVC 2009, May 19, 2009 - May 19, 2009*, St. Charles, IL, United states, 2009.

[30] C. La, M. Poggi, P. Murphy, and O. Zitko, "NVH considerations for zero emissions vehicle driveline design," in *SAE 2011 Noise and Vibration Conference and Exhibition, NVC 2011, May 16, 2011 - May 19, 2011*, Rapids, MI, United states, 2011.

[31] Rolls-Royce, "The HSG concept," P. E. S. Bergen, Ed., ed, 2010.

[32] Rolls-Royce, "Hybrid shaft generator propulsion system upgrade," P. E. S. Bergen, Ed., ed, 2010.

[33] P. C. Krause, O. Wasynczuk, and S. D. Sudhoff, *Analysis of electric machinery and drive systems*, 2nd ed. New York: IEEE Press, 2002.

[34] R. Krishnan, *Electric motor drives : modeling, analysis, and control*. Upper Saddle River, N.J.: Prentice Hall, 2001.

[35] C.-M. Ong, *Dynamic simulation of electric machinery : using MATLAB/SIMULINK*. Upper Saddle River, N.J.: Prentice Hall PTR, 1998.

[36] Z. Q. Zhu and D. Howe, "Instantaneous magnetic field distribution in brushless permanent magnet dc motors. Part II: Armature-reaction field," *IEEE Transactions on Magnetics,* vol. 29, pp. 136-142, 1993.

[37] Z. Q. Zhu and D. Howe, "Instantaneous magnetic field distribution in permanent magnet brushless dc motors. Part IV: Magnetic field on load," *IEEE Transactions on Magnetics,* vol. 29, pp. 152-158, 1993.

[38] Z. Q. Zhu and D. Howe, "Instantaneous magnetic field distribution in brushless permanent magnet dc motors. Part III: Effect of stator slotting," *IEEE Transactions on Magnetics,* vol. 29, pp. 143-151, 1993.

[39] Z. Q. Zhu, D. Howe, E. Bolte, and B. Ackermann, "Instantaneous magnetic field distribution in brushless permanent magnet dc motors. Part I: Open-circuit field," *IEEE Transactions on Magnetics,* vol. 29, pp. 124-135, 1993.

[40] R. Islam and I. Husain, "Analytical model for predicting noise and vibration in permanent-magnet synchronous motors," *IEEE Transactions on Industry Applications,* vol. 46, pp. 2346-2354, 2010.

[41] W. Lei, D. Xianming, L. Jia, W. Kang, and W. Ruixian, "Design and finite element analysis of permanent magnet synchronous motor with novel rotor type," in *2010 Asia-Pacific Power and Energy Engineering Conference (APPEEC)*, 2010, pp. 1-4.

[42] M. Cosovic, S. Smaka, I. Salihbegovic, and S. Masic, "Design optimization of 8/14 switched reluctance machine for electric vehicle," in *2012 International Conference on Electrical Machines (ICEM)*, 2012, pp. 2654-2659.

[43] B. Vaseghi, N. Takorabet, and F. Meibody-Tabar, "Fault analysis and parameter identification of permanent-magnet motors by the finite-element method," *IEEE Transactions on Magnetics,* vol. 45, pp. 3290 - 3295, 2009.

[44] V. M. Zivotic-Kukolj, W. L. Soong, and N. Ertugrul, "Investigation of iron losses in a high flux interior PM automotive alternator," in *Australasian Universities Power Engineering Conference 2004*, Brisbane, Australia, 2004.

[45] B. M. Ebrahimi and J. Faiz, "Feature extraction for short-circuit fault detection in permanent-magnet synchronous motors using stator-current monitoring," *IEEE Transcations on Industrial Electronics,* vol. 25, pp. 2673 - 2682, 2010.

[46] N. Mohan, T. M. Undeland, and W. P. Robbins, *Power electronics : converters, applications, and design*, 3rd ed. Hoboken, NJ: John Wiley & Sons, 2003.

[47] P. Vas, *Sensorless vector and direct torque control*. Oxford ; New York: Oxford University Press, 1998.

[48] J. F. Gieras, *Permanent magnet motor technology : design and applications*, 3rd ed. Boca Raton: CRC Press, 2010.

[49] P. g. W.-. 1050, "Vector control of pmsg for grid-connected wind turbine applications," Master Theses and Dissertations, Institute of Energy Technology, Aalborg University, Spring 2009.

[50] M. Durr, A. Cruden, S. Gair, and J. R. McDonald, "Dynamic model of a lead acid battery for use in a domestic fuel cell system," *Journal of Power Sources,* vol. 161, pp. 1400-1411, 2006.

[51] N. Feki, G. Clerc, and P. Velex, "An integrated electro-mechanical model of motor-gear units-Applications to tooth fault detection by electric measurements," *Mechanical Systems and Signal Processing,* vol. 29, pp. 377-390, May 2011.

[52] A. Abass and A. T. Shenton, "Automotive driveline modelling, inverse-simulation and compensation," in *UKSim/AMSS 1st International Conference on Intelligent Systems, Modelling and Simulation, ISMS 2010, January 27, 2010 - January 29, 2010*, Liverpool, United kingdom, 2010, pp. 244-249.

[53] M. Cipek, J. Deur, and J. Petric, "Bond graph analysis of power flow in series-parallel hybrid electric vehicle transmissions," in *UKACC International Conference on CONTROL 2010, September 7, 2010 - September 10, 2010*, Coventry, United kingdom, 2010, pp. 217-223.

[54] B. K. Powell, K. E. Bailey, and S. R. Cikanek, "Dynamic modeling and control of hybrid electric vehicle powertrain systems," *IEEE Control Systems Magazine,* vol. 18, pp. 17-33, 1998.

[55] A. R. Crowther and N. Zhang, "Torsional finite elements and nonlinear numerical modelling in vehicle powertrain dynamics," *Journal of Sound and Vibration,* vol. 284, pp. 825-49, 2005.

[56] M. Todorov, I. Dobrev, and F. Massouh, "Analysis of torsional oscillation of the drive train in horizontal-axis wind turbine," in *2009 8th International Symposium on Advanced Electromechanical Motion Systems & Electric Drives Joint Symposium (ELECTROMOTION 2009), 1-3 July 2009*, Piscataway, NJ, USA, 2009, p. 7 pp.

[57] Z. Daneshi-Far, H. Henao, and G. A. Capolino, "Planetary gearbox effects on induction machine in wind turbine: Modeling and analysis," in *Proceedings - 2012 20th International Conference on Electrical Machines, ICEM 2012*, 2012, pp. 1790-1796.

[58] J. Wojnarowski, J. Kopec, and S. Zawislak, "Gears and graphs [gear modelling]," *Journal of Theoretical and Applied Mechanics,* vol. 44, pp. 139-62, 2006.

[59] P. Velex and M. Maatar, "Mathematical model for analyzing the influence of shape deviations and mounting errors on gear dynamic behaviour," *Journal of Sound and Vibration,* vol. 191, pp. 629-660, 1996.

[60] T. Eritenel and R. G. Parker, "Three-dimensional nonlinear vibration of gear pairs," *Journal of Sound and Vibration,* vol. 331, pp. 3628-3648, 2012.

[61] R. Singh, H. Xie, and R. J. Comparin, "Analysis of automotive neutral gear rattle," *Journal of Sound and Vibration,* vol. 131, pp. 177-96, 1989.

[62] M. Y. Wang, R. Manoj, and W. Zhao, "Gear rattle modelling and analysis for automotive manual transmissions," *Proceedings of the Institution of Mechanical Engineers, Part D: Journal of Automobile Engineering,* vol. 215, pp. 241-258, 2001.

[63] B. E. J., "Simulations of gear-based systems including backlash," Ph.D. theses and dissertations, Lehigh University, 2006.

[64] S. V. Neriya, R. B. Bhat, and T. S. Sankar, "On the dynamic response of a helical geared system subjected to a static transmission error in the form of deterministic and filtered white noise inputs," in *Rotating Machinery Dynamics. Presented at the 1987 ASME Design Technology Conferences - 11th Biennial Conference on Mechanical Vibration and Noise.*, Boston, MA, USA, 1987, pp. 287-296.

[65] L. Hong and J. S. Dhupia, "A time domain approach to diagnose gearbox fault based on measured vibration signals," *Journal of Sound and Vibration,* vol. 333, pp. 2164-2180, 2014.

[66] M. Inalpolat and A. Kahraman, "A dynamic model to predict modulation sidebands of a planetary gear set having manufacturing errors," *Journal of Sound and Vibration,* vol. 329, pp. 371-393, 2010.

[67] P. Fisette, O. Bruls, and J. Swevers, "Multiphysics modeling of mechatronic multibody systems," in *International Conference on Noise and Vibration Engineering 2006, ISMA 2006, September 18, 2006 - September 20, 2006*, Heverlee, Belgium, 2006, pp. 41-67.

[68] MathWorks Inc., *Simulink® : simulation and model-based design : using Simulink*, 6. ed. Natick, MA: MathWorks, 2005.

[69] S. Hauptmann, S. Mulski, M. Kuhn, and L. Mauer, "Advanced drive train modeling in a virtual wind turbine using the multibody simulation code simpack," in *European Wind Energy Conference and Exhibition 2007, EWEC 2007, May 7, 2007 - May 10, 2007*, Milan, Italy, 2007, pp. 1074-1079.

[70] A. Yuejun, W. Hongliang, M. Zhaojun, Z. Wenqiang, and L. Guoming, "Performance analysis of novel magnet arrayed permanent magnet synchronous motor based on ANSOFT," Piscataway, NJ, USA, 2010, pp. 715-18.

[71] D. Liu, H. Chen, R. Jiang, and W. Liu, "Study of driving performance of semi-active suspension based on hybrid control strategy," in *2010 2nd WRI Global Congress on Intelligent Systems, GCIS 2010, December 16, 2010 - December 17, 2010*, Wuhan, China, 2010, pp. 43-46.

[72] Y. Yasa, Y. Sozer, and E. Mese, "Unbalanced fault analysis of doubly fed induction generator drive system for wind turbine applications," in *Applied Power Electronics Conference and Exposition (APEC), 2013 Twenty-Eighth Annual IEEE*, 2013, pp. 2953-2960.

[73] O. Haedrich and U. Knorr, "Electric circuit and control system simulation by linking simplorer and Matlab/Simulink - analysis of interactions of subsystems of modern electric drives," in *7th Workshop on Computers in Power Electronics, July 16, 2000 - July 18, 2000*, Blacksburg, VA, USA, 2000, pp. 192-196.

[74] H. M. Paynter, *Analysis and design of engineering systems*. Cambridge, Mass.,: M. I. T. Press, 1961.

[75] D. Karnopp and R. C. Rosenberg, *Analysis and simulation of multiport systems; the bond graph approach to physical system dynamics*. Cambridge, Mass.,: M.I.T. Press, 1968.

[76] D. Karnopp and R. C. Rosenberg, *System dynamics : a unified approach*. New York: Wiley, 1975.

[77] D. Karnopp, D. L. Margolis, and R. C. Rosenberg, *System dynamics : a unified approach*, 2nd ed. New York: Wiley, 1990.

[78] J. U. Thoma, *Introduction to bond graphs and their applications*, 1st ed. Oxford ; New York: 1975., 1975.

[79] T. Bakka and H. R. Karimi, "Wind turbine modeling using the bond graph," in *Computer-Aided Control System Design (CACSD), 2011 IEEE International Symposium on*, 2011, pp. 1208-1213.

[80] M. Ronkowski, "Modelling of electrical machines using the Modelica Bond-Graph Library," in *Power Electronics and Motion Control Conference, 2008. EPE-PEMC 2008. 13th*, 2008, pp. 880-886.

[81] L. I. Silva, P. M. de la Barrera, C. H. De Angelo, G. R. Bossio, and G. O. Garcia, "Multi-domain modeling of electric traction drives using Bond Graphs: Application to fault diagnosis," in *Industrial Electronics,*

2009. IECON '09. 35th Annual Conference of IEEE, 2009, pp. 3455-3460.

[82] B. Umesh Rai and L. Umanand, "Bond graph toolbox for handling complex variable," *Control Theory & Applications, IET,* vol. 3, pp. 551-560, 2009.

[83] S. He, R. Gunda, and R. Singh, "Effect of sliding friction on the dynamics of spur gear pair with realistic time-varying stiffness," *Journal of Sound and Vibration,* vol. 301, pp. 927-949, 2007.

[84] H.-H. Lin, R. L. Huston, and J. J. Coy, "On Dynamic Loads in Parallel Shaft Transmissions: I - Modeling and Analysis," 1987.

[85] M. T. Khabou, N. Bouchaala, F. Chaari, T. Fakhfakh, and M. Haddar, "Study of a spur gear dynamic behavior in transient regime," *Mechanical Systems and Signal Processing,* vol. 25, pp. 3089-101, 2011.

[86] P. J. Tavner, *Condition monitoring of rotating electrical machines*. London, U.K.: Institution of Engineering and Technology, 2008.

[87] P. D. Samuel and D. J. Pines, "A review of vibration-based techniques for helicopter transmission diagnostics," *Journal of Sound and Vibration,* vol. 282, pp. 475-508, 2005.

[88] R. B. Randall, "New method of modeling gear faults," *American Society of Mechanical Engineers,* 1981.

[89] M. J. Zuo and F. Xianfeng, "Gearbox fault detection using Hilbert and wavelet packet transform," *Mechanical Systems and Signal Processing,* vol. 20, pp. 966-82, 2006.

[90] D. He, L. Ruoyu, and E. Bechhoefer, "Split torque type gearbox fault detection using acoustic emission and vibration sensors," in *2010 International Conference on Networking, Sensing and Control (ICNSC 2010), 10-12 April 2010*, Piscataway, NJ, USA, 2010, pp. 62-6.

[91] P. T. Monsen, E. S. Manolakos, and M. Dzwonczyk, "Helicopter gearbox fault detection and diagnosis using analog neural networks," in *Proceedings of 27th Asilomar Conference on Signals, Systems and Computers, 1-3 Nov. 1993*, Los Alamitos, CA, USA, 1993, pp. 381-5.

[92] W. Wang, "Early detection of gear tooth cracking using the resonance demodulation technique," *Mechanical Systems and Signal Processing,* vol. 15, pp. 887-903, 2001.

[93] F. K. Choy, S. Huang, J. J. Zakrajsek, R. F. Handschuh, and D. P. Townsend, "Vibration signature analysis of a faulted gear transmission system," *Journal of Propulsion and Power,* vol. 12, pp. 289-295, 1996.

[94] J. R. Stack, R. G. Harley, and T. G. Habetler, "An amplitude Modulation detector for fault diagnosis in rolling element bearings," *IEEE Transcations on Industrial Electronics,* vol. 51, pp. 1097-1102, 2004.

[95] J. R. Stack, T. G. Habetler, and R. G. Harley, "Fault-signature modeling and detection of inner-race bearing faults," *IEEE Transactions on Industry Applications,* vol. 42, pp. 61-68, 2006.

[96] B. M. Ebrahimi, J. Faiz, and M. J. Roshtkhari, "Static-, dynamic-, and mixed-eccentricity fault diagnoses in permanent-magnet synchronous motors," *IEEE Transcations on Industrial Electronics,* pp. 4727 - 4739, 2009.

[97] A. Djerdir, J.-A. Farooq, A. Rezig, and A. Miraoui, "Faults in permanent magnet traction motors: state of the art and modelling approaches," presented at the 2010 IEEE Power & Energy Society General Meeting, 2010.

[98] J. J. Sinou and A. W. Lees, "The influence of cracks in rotating shafts," *Journal of Sound and Vibration,* vol. 285, pp. 1015-37, 2005.

[99] B. Wagner, "Rotating Equipment Defect Detection Using the Algorithm of Mode Isolation," Ph.D. , School of Mechanical Engineering, Georgia Institute of Technology, 2007.

[100] M. S. Yilmaz and E. Ayaz, "Adaptive neuro-fuzzy inference system for bearing fault detection in induction motors using temperature, current, vibration data," in *IEEE EUROCON 2009, 18-23 May 2009*, Piscataway, NJ, USA, 2009, pp. 1140-5.

[101] A. D. Nembhard, J. K. Sinha, A. J. Pinkerton, and K. Elbhbah, "Fault diagnosis of rotating machines using vibration and bearing temperature measurements," *Diagnostyka,* vol. 14, pp. 45-51, 2013.

[102] J. C. Banks, M. Lebold, and K. Reichard, "Fault localization for gear tooth failure in coupled mechanical systems," in *2003 IEEE Aerospace Conference, March 8, 2003 - March 15, 2003*, Big Sky, MT, United states, 2003, pp. 3295-3304.

[103] B. M. Ebrahimi, J. Faiz, and M. J. Roshtkhari, "Static-, dynamic-, and mixed-eccentricity fault diagnoses in permanent-magnet synchronous motors," *IEEE TRANSACTIONS ON INDUSTRIAL ELECTRONICS,* pp. 4727 - 4739, 2009.

[104] B. Yazici, G. B. Kliman, W. J. Premerlani, R. A. Koegl, G. B. Robinson, and A. Abdel-Malek, "Adaptive, on-line, statistical method for bearing fault detection using stator current," in *Proceedings of the 1997 IEEE Industry Applications Conference 32nd IAS Annual Meeting. Part 3 (of 3), October 5, 1997 - October 9, 1997*, New Orleans, LA, USA, 1997, pp. 213-220.

[105] H. Liu and J. S. Dhupia, "A time-domain fault detection method based on an electrical machine stator current measurement for planetary gear-sets," in *2013 IEEE/ASME International Conference on Advanced Intelligent Mechatronics (AIM), 9-12 July 2013*, Piscataway, NJ, USA, 2013, pp. 1631-6.

[106] T. G. Habetler, "Current-Based Motor Condition Monitoring: Complete Protection of Induction and PM Machines," presented at the IEEE, 2007.

[107] J. Rosero, A. G. Espinosa, J. Cusido, J. A. Ortega, and L. Romeral, "Simulation and fault detection of short circuit winding in a Permanent Magnet Synchronous Machine (PMSM) by means of fourier and wavelet transform," presented at the IEEE International Instrumentation and Measurement Technology Conference, Victoria, Vancouver Island, Canada, 2008.

[108] L. Romeral, J. A. Rosero, A. G. Espinosa, J. Cusido, and J. A. Ortega, "Electrical Monitoring for Fault Detection in an EMA," *IEEE Aerospace and Electronic Systems Magazine,* pp. 4 - 9, MARCH 2010.

[109] C. Dae-Woong, S. Seung-Ki, and L. Dong-Choon, "Analysis and compensation of current measurement error in vector controlled AC motor drives," in *Industry Applications Conference, 1996. Thirty-First IAS Annual Meeting, IAS '96., Conference Record of the 1996 IEEE*, 1996, pp. 388-393 vol.1.

[110] S. Diao, Z. Makni, J. F. Bisson, D. Diallo, and C. Marchand, "Sensor fault diagnosis for improving the availability of electrical drives," in *IECON 2013 - 39th Annual Conference of the IEEE Industrial Electronics Society (IECON 2013), 10-13 Nov. 2013*, Piscataway, NJ, USA, 2013, pp. 3108-13.

[111] T. G. Habetler, "Current-based condition monitoring of electrical machines in safety critical applications," presented at the 13th International Power Electronics and Motion Control Conference, 2008.

[112] W. le Roux, R. G. Harley, and T. G. Habetler, "Detecting rotor faults in low power permanent magnet synchronous machines," *IEEE Transcations on Industrial Electronics,* vol. 22, pp. 322-8, 2007.

[113] J. A. Farooq, A. Djerdir, and A. Miraoui, "Identification of demagnetization faults in a permanent magnet synchronous machine by

permeance network," *COMPEL - The International Journal for Computation and Mathematics in Electrical and Electronic Engineering,* vol. 28, pp. 1619-1631, 2009.

[114] B. Yu and A. H. C. Van Paassen, "Simulink and bond graph modeling of an air-conditioned room," *Simulation Modelling Practice and Theory,* vol. 12, pp. 61-76, 2004.

[115] E. M. Alawadhi, *Finite element simulations using ANSYS*. Boca Raton: CRC Press, 2010.

[116] M. Barthod, B. Hayne, J. L. Tebec, and J. C. Pin, "Experimental study of dynamic and noise produced by a gearing excited by a multi-harmonic excitation," *Applied Acoustics,* vol. 68, pp. 982-1002, 2007.

[117] A. J. Mitcham and J. J. A. Cullen, "Permanent magnet generator options for the More Electric Aircraft," in *Power Electronics, Machines and Drives, 2002. International Conference on (Conf. Publ. No. 487)*, 2002, pp. 241-245.

[118] M. Comanescu, A. Keyhani, and D. Min, "Design and analysis of 42-V permanent-magnet generator for automotive applications," *Energy Conversion, IEEE Transactions on,* vol. 18, pp. 107-112, 2003.

[119] F. Chaari, W. Baccar, M. S. Abbes, and M. Haddar, "Effect of spalling or tooth breakage on gearmesh stiffness and dynamic response of a one-stage spur gear transmission," *European Journal of Mechanics / A Solids,* vol. 27, pp. 691-705, 2008.

[120] J. Zhang, J. S. Dhupia, and C. J. Gajanayake, "Gear Rattle under Influence of Bearings, Lubricant Churning and Gear Tooth Sliding Friction within a Geared Mechanism," in *in 2014 International Symposium on Flexible Automation (ISFA2014)*, Awaji-Island, Hyogo, Japan, 2014.

[121] E. Rocca and R. Russo, "Theoretical and experimental investigation into the influence of the periodic backlash fluctuations on the gear rattle," *Journal of Sound and Vibration,* vol. 330, pp. 4738-4752, 2011.

[122] L. Hong, J. S. Dhupia, and S. Sheng, "An explanation of frequency features enabling detection of faults in equally-spaced planetary gearbox," *Mechanism and Machine Theory,* vol. 73, pp. 169-183, 2014.

[123] M. Esmaeli and A. Subramaniam, "Engine Timing Geartrain Concepts and Proposals for Gear Rattle Noise Reduction in Commercial Vehicles," Master of Science, Department of Product and Production Development, Division of Product Development, Chalmers University of Technology, Göteborg, Sweden, 2011.

[124] J. R. Ottewill, S. A. Neild, and R. E. Wilson, "An investigation into the effect of tooth profile errors on gear rattle," *Journal of Sound and Vibration,* vol. 329, pp. 3495-3506, 2010.

[125] S. Ohnuma, S. Yahata, M. Inagawa, and T. Fujimoto, "Research on idling rattle of manual transmission," in *Surface Vehicle Noise and Vibration Conference, May 15, 1985 - May 17, 1985*, Traverse City, MI, United states, 1985.

[126] H. Moradi and H. Salarieh, "Analysis of nonlinear oscillations in spur gear pairs with approximated modelling of backlash nonlinearity," *Mechanism and Machine Theory,* vol. 51, pp. 14-31, 2012.

[127] G. Bonori and F. Pellicano, "Non-smooth dynamics of spur gears with manufacturing errors," *Journal of Sound and Vibration,* vol. 306, pp. 271-83, 2007.

[128] M. Barthod, B. Hayne, and J. L. Tebec, "Auditory perception of noise known as "rattle" in gearboxes," *Acta Acustica United With Acustica,* vol. 91, pp. 180-91, 2005.

[129] R. Singh, "Gear noise: Anatomy, prediction and solutions," in *38th International Congress and Exposition on Noise Control Engineering 2009, INTER-NOISE 2009, August 23, 2009 - August 26, 2009*, Ottawa, ON, Canada, 2009, pp. 3691-3720.

[130] Y. Kadmiri, E. Rigaud, J. Perret-Liaudet, and L. Vary, "Experimental and numerical analysis of automotive gearbox rattle noise," *Journal of Sound and Vibration,* vol. 331, pp. 3144-3157, 2012.

[131] J. L. Dion, S. Le Moyne, G. Chevallier, and H. Sebbah, "Gear impacts and idle gear noise: experimental study and non-linear dynamic model," *Mechanical Systems and Signal Processing,* vol. 23, pp. 2608-28, 2009.

[132] "Calculation of load capacity of spur and helical gears," Standard ISO 6336-1, 2007.

[133] I. P. Girsang, J. S. Dhupia, E. Muljadi, M. Singh, and L. Y. Pao, "Gearbox and drivetrain models to study dynamic effects of modern wind turbines," in *2013 IEEE Energy Conversion Congress and Exposition (ECCE), 15-19 Sept. 2013*, Piscataway, NJ, USA, 2013, pp. 874-81.

[134] P. Eschmann, L. Hasbargen, Weigand, J. Brändlein, and FAG Kugelfischer Georg Schäfer KGaA., *Ball and roller bearings : theory, design, and application*, 2nd ed. München; Chichester; New York: R. Oldenbourg; Wiley, 1985.

[135] G. SKF, "SKF general catalogue," ed, 2003.

[136] S. Iqbal, F. Al-Bender, J. Croes, B. Pluymers, and W. Desmet, "Frictional power loss in solid-grease-lubricated needle roller bearing," *Lubrication Science,* vol. 25, pp. 351-367, 2013.

[137] C. Changenet and P. Velex, "A model for the prediction of churning losses in geared Transmissions-preliminary results," *Transactions of the ASME. Journal of Mechanical Design,* vol. 129, pp. 128-33, 2007.

[138] C. Changenet, X. Oviedo-Marlot, and P. Velex, "Power loss predictions in geared transmissions using thermal networks-applications to a six-speed manual gearbox," *Transactions of the ASME. Journal of Mechanical Design,* vol. 128, pp. 618-25, 2006.

[139] R. L. Seaman, C. E. Johnson, and R. F. Hamilton, "Component inertial effects on transmission design," in *Truck and Bus Meeting and Exposition, December 3, 1984 - December 6, 1984*, Dearborn, MI, United states, 1984.

[140] P. Velex, "On the modelling of spur and helical gear dynamic behaviour," *Mechanical Engineering,* pp. 75-106, 2012.

[141] I. P. Girsang, J. S. Dhupia, E. Muljadi, M. Singh, and J. Jonkman, "Modeling and control to mitigate resonant load in variable-speed wind turbine drivetrain," *IEEE Journal of Emerging and Selected Topics in Power Electronics,* vol. 1, pp. 277-286, 2013.

[142] I. P. Girsang, J. S. Dhupia, E. Muljadi, M. Singh, and L. Y. Pao, "Gearbox and drivetrain models to study dynamic effects of modern wind turbines," in *Energy Conversion Congress and Exposition (ECCE), 2013 IEEE*, 2013, pp. 874-881.

[143] R. B. Randall, "A New Method of Modeling Gear Faults," *Journal of Mechanical Design,* vol. 104, pp. 259-267, 1982.

[144] M. Rgeai, F. Gu, A. Ball, M. Elhaj, and M. Ghretli, "Gearbox fault detection using spectrum analysis of the drive motor current signal," in *Proceedings of the 4th World Congress on Engineering Asset Management*, Athen, Greece, 2009, pp. 758-769.

[145] M. Haram, T. Wang, F. Gu, and A. D. Ball, "Electrical motor current signal analysis using a modulation signal bispectrum for the fault diagnosis of a gearbox downstream," *Journal of Physics: Conference Series,* vol. 364, 2012.

[146] I. X. Bogiatzidis, A. N. Safacas, and E. D. Mitronikas, "Detection of backlash phenomena appearing in a single cement kiln drive using the current and the electromagnetic torque signature," *IEEE Transcations on Industrial Electronics,* vol. 60, pp. 3441-3453, 2013.

[147] S. Rajagopalan, T. G. Habetler, R. G. Harley, T. Sebastian, and B. Lequesne, "Current/voltage-based detection of faults in gears coupled to electric motors," *IEEE Transcations on Industrial Applications,* vol. 42, pp. 1412-20, 2006.

[148] C. Kar and A. R. Mohanty, "Monitoring gear vibrations through motor current signature analysis and wavelet transform," *Mechanical Systems and Signal Processing,* vol. 20, pp. 158-187, 2006.

[149] J. Zhang, L. Hong, and J. S. Dhupia, "Gear fault detection in planetary gearbox using stator current measurement of ac motors," *ASME 2012 5th Annual Dynamic Systems and Control Conference Joint with the JSME 2012 11th Motion and Vibration Conference, DSCC 2012-MOVIC 2012,* vol. 1, pp. 673-680, 2012.

[150] Z. Jidong, J. S. Dhupia, and C. J. Gajanayake, "Model based current analysis of electrical machines to detect faults in planetary gearboxes," in *2014 IEEE/ASME International Conference on Advanced Intelligent Mechatronics (AIM), 8-11 July 2014*, Piscataway, NJ, USA, 2014, pp. 1616-21.

[151] Q. Hao, L. Gao, X. Wang, and H. Ye, "Application study on resonance demodulation technique in fault diagnosis of gear box," in *International Conference on Engineering Design and Optimization, ICEDO 2010, October 28, 2010 - October 30, 2010*, Ningbo, China, 2010, pp. 198-202.

[152] A. Ghasemlooniaa and S. E. Z. Khadem, "Gear tooth failure detection by the resonance demodulation technique and the instantaneous power spectrum method: A comparative study," *Shock and Vibration,* vol. 18, pp. 503-23, 2011.

[153] D. W. Novotny and T. A. Lipo, *Vector control and dynamics of AC drives*. Oxford, New York: Clarendon Press; Oxford University Press, 1996.

List of Publications

1. J. Zhang, J. S. Dhupia, and C. J. Gajanayake, "Model Based Current Analysis of Electrical Machines to Detect Faults in Planetary Gearboxes," Proceedings of AIM 2014, IEEE/ASME International Conference on Advanced Intelligent Mechatronics, 2014.

2. J. Zhang, J. S. Dhupia, and C. J. Gajanayake, "Gear Rattle under Influence of Bearings, Lubricant Churning and Gear Tooth Sliding Friction within a Geared Mechanism," Proceedings of ISCIE/ASME 2014 International Symposium on Flexible Automation, 2014.

3. J. Zhang, J. S. Dhupia, and C. J. Gajanayake, "Stator Current Analysis from Electrical Machines Using Resonance Demodulation Technique to Detect Faults in Planetary Gearboxes ", IEEE Transactions on Industrial Electronics, accepted, 2015.

4. J. Zhang, J. S. Dhupia, L. Hong, and C. J. Gajanayake, "Evaluating the Effects of Gearbox Parameters on the Gear Rattle Noise," International Journal of Automotive Technology, to be submitted soon, 2015.

5. J. Zhang, L. Hong, and J. S. Dhupia, "Gear fault detection in planetary gearbox using stator current measurement of ac motors," ASME 2012 5th Annual Dynamic Systems and Control Conference Joint with the JSME 2012 11th Motion and Vibration Conference, vol. 1, pp. 673-680, 2012.